Performance of the SmartPET Positron Emission Tomography System for Small Animal Imaging

Thesis submitted in accordance with the requirements of the
University of Liverpool for the degree of
Doctor in Philosophy

by

Reynold James Cooper

Oliver Lodge Laboratory

October 2007

Abstract

Performance of the SmartPET Positron Emission Tomography System for Small Animal Imaging

Reynold James Cooper

The experimental results presented in this study demonstrate the performance of a prototype Positron Emission Tomography system utilising planar HPGe detector technology. The experimental measurements undertaken provide evidence of the feasibility of such a system for small animal imaging. It has been shown how the use of digital Pulse Shape Analysis techniques may be employed in order to improve the achievable image quality.

By performing high precision scans of one the SmartPET HPGe detectors with finely collimated gamma-ray beams at a range of energies the performance and response of the detector as a function of gamma-ray interaction position has been quantified. This analysis has facilitated the development of parametric Pulse Shape Analysis techniques and algorithms for the correction of imperfections in detector response. These algorithms have then been applied to data from PET imaging measurements using both SmartPET detectors in conjunction with the specially designed rotating gantry.

A number of point sources have been imaged and it has been shown how, when using simple PSA approaches, the nature of an event has direct implications for the quality of the resulting image. Over 60% of coincident events from 511keV gamma rays have been processed in imaging these point sources, increasing the imaging sensitivity by a factor of three in comparison to previous work. The absolute detection sensitivity of the SmartPET system has been found to be 0.99%.

The SmartPET system has been used to image distributed sources for the first time. A ^{22}Na line source was imaged in a number of different orientations and reconstructed with a spatial resolution approaching the fundamental limitations imposed by gamma-ray non-colinearity and positron range blurring. Increasingly complex source distributions have

been imaged, demonstrating the ability of the system to resolve multiple features with fine spatial resolution. These measurements then allowed the current limitations of the system to be identified.

Contents

List of Figures

List of Tables

Chapter 1

Introduction

The use of germanium detectors for gamma-ray spectroscopy has revolutionised the field of nuclear structure physics research since their introduction in the early 1960s, their unrivaled energy resolution allowing the structure of the nucleus to be probed in ever finer detail.

The continued development of germanium detector technology coupled with advances in digital electronics and data processing techniques has effectively heralded the dawn of a new era in the use of semiconductor gamma-ray detectors. Indeed, large scale collaborations in both Europe and the USA are working to develop the ultimate gamma-ray spectrometer for nuclear structure physics research.

While these advances have traditionally been fuelled by the pursuit of academic progress, the need for state of the art radiation detection systems in a range of applied fields is becoming an increasingly important driver. The well established crossover between physics and medicine is one obvious target for the application of this detector technology.

1.1 Nuclear Medical Imaging

Diagnostic nuclear medical imaging utilises the properties of nuclear radiation to aid patient diagnosis through imaging. Two common imaging modalities which fall into this branch of medicine are Positron Emission Tomography (PET) [Val03] and Single Photon Emission Computed Tomography (SPECT) [Che03]. These techniques may be used to probe the physiological function of the human body and as such are commonly used in the diagnosis of cancer and the assessment of organ performance.

Both PET and SPECT require that a patient be administered a radiopharmaceutical known as a radiotracer. This substance is a radioactive element delivered in the form of a chemical known to exhibit specific behaviour in the body. The detection of gamma rays emitted by this decaying tracer allows an image of the source distribution to be created. As the patients body naturally metabolises the radiotracer, regions of non-uniform activity within an organ are often indicative of disease. A common example in PET imaging is the use of the radiotracer ^{18}F-FDG (fluorodeoxyglucose) [Val03], used in the field of oncology to identify the size and location of tumours.

1.2 The SmartPET Project

The SmartPET (Small Animal Reconstruction Tomograph for Positron Emission Tomography) project is the development of a small animal PET demonstrator system based on the use of germanium detectors and state of the art digital electronics. Through the use of Pulse Shape Analysis techniques (PSA) [Lie01] this system aims to improve the spatial resolution achievable in medical images while the intrinsic properties of germanium as a gamma-ray detector hold the potential to increase patient throughput and/or reduce patient dose through increases in sensitivity.

The primary aim of the SmartPET system is to provide proof of principle for the use of High Purity germanium (HPGe) detectors in medical imaging, developing an integrated small animal PET system capable of performing online event processing. As such it is designed to operate as a dual head PET camera. It is however versatile enough to be used in SPECT configuration in the form of a Compton camera [Ger05], [Vet04], where the use of cone beam reconstruction techniques [Tom03] provides electronic collimation. This makes the mechanical collimation required in commercial SPECT systems redundant, hugely increasing the efficiency of the system, while the excellent energy resolution of germanium detectors provides the opportunity for multi-tracer SPECT studies. Finally, Monte Carlo simulations have demonstrated the feasibility of operating the system in ‘Compton PET’ mode. By operating the system in this mode Gillam *et al.* [Gil07] have shown how reconstructing the kinematics of Compton scattered events may improve the signal to noise ratio of PET images by allowing poor quality events, those arising from random coincidence for example, to be vetoed.

1.3 Research Overview

The work presented in this thesis discusses the first tests of the SmartPET system as a fully functional dual head PET camera comprising two planar HPGe detectors, automated rotating gantry and fast digital electronics. Pulse Shape Analysis techniques based on parameterisation of the detector preamplifier response have been developed in order to improve the localisation of the gamma-ray interaction position on an event-by-event basis. These techniques have then been integrated into a data processing routine which corrects for imperfections in detector performance and facilitates imaging. The data processing procedure has been developed to be computationally inexpensive (reducing an event to be described in terms of parameter lists as soon as is practicable) such that in future stages of the project the analysis techniques may be performed online.

The SmartPET system has then been used to image three ^{22}Na point sources where the fraction of events used for imaging has been increased by a factor of three compared to previous work. In analysis of these data an investigation into the impact of different event types on image quality has been performed.

A range of increasingly complex distributed sources have then been imaged with the system and the image quality quantified. Finally, the current performance of the SmartPET system has been reviewed both in its own right and in relation to several commercially available small animal PET systems.

Chapter 2

Positron Emission Tomography

Positron Emission Tomography (PET) is a diagnostic imaging modality which allows organ function to be assessed via the quantitative study of tracer uptake in a subject. This tracer takes the form of a positron emitting nuclide with a chemical composition similar to a biological substance such as glucose. When this radiotracer decays via the emission of a positron, the resulting colinear annihilation gamma-rays are detected in coincidence allowing a Line of Response (LoR) [Val03] to be defined between the two points of detection. As the point of β^+ annihilation must lie somewhere along this line, defining multiple LoRs over a full range of angles allows line integrals describing the source distribution to be produced. Processing these projections[1] with image reconstruction algorithms allows an accurate image of the source distribution to be generated and used to aid diagnosis. Common clinical applications include the assessment of cardiac performance, the monitoring of brain function and tumour identification. This chapter discusses some of the physical principles of Positron Emission Tomography, the use of PET in small animal studies and common image reconstruction techniques.

2.1 Positron Emission

An unstable proton rich nucleus may decay via the emission of a positron (β^+ decay). A positron is the anti-particle of the electron and as such has the exact physical properties but opposite charge to the electron. The mechanism of positron decay allows the nucleus in

---

[1] The term projections is used to refer to a set of LoRs measured at a given angle.

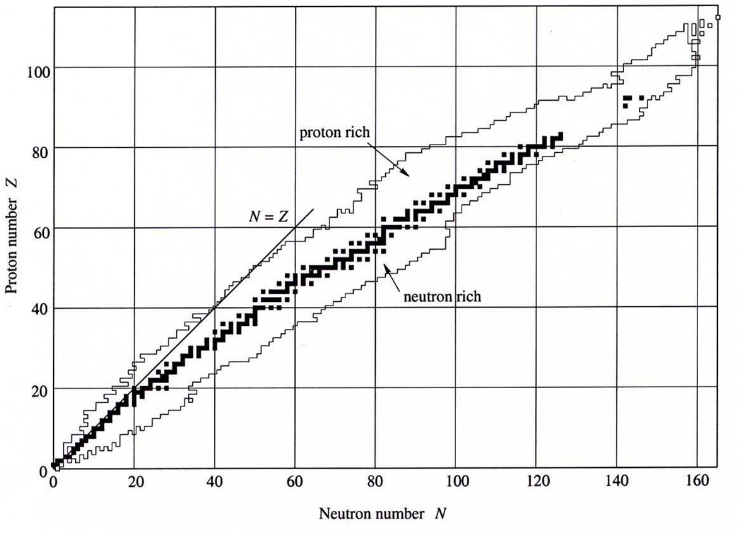

Figure 2.1: The Segre chart of nuclides plotted according to proton number Z and neutron number N. The proton-neutron (Z=N) symmetry line is displayed along with the valley of stability (denoted by black squares). Reproduced from [Lil02].

question to decay into a more stable isobar[2] closer to the line of stability with the nuclear charge decreasing by one unit. Figure 2.1 shows the Segre chart of the nuclides in terms of proton number (Z) and neutron number (N) where the line of stability is represented by solid black squares. The members of an isobar may be plotted in terms of their excess energy and neutron number to reveal a parabolic shape. This may be considered to be a diagonal cross-section through the valley of stability where the most stable nuclei lie at the bottom of the parabola. Figure 2.2 shows an example of this for the A=61 isobar. This figure shows how β^+ emission acts to reduce proton number toward stability at Z=28.

Although not fully understood, the process of β^+ decay can be thought to correspond to the conversion of a proton into a neutron and a positron inside the nucleus via the weak nuclear force [Lil02]. In this process a neutrino is also created and the reaction can be represented as

$$p \rightarrow n + \beta^+ + \nu. \tag{2.1}$$

As the neutron mass is greater than that of the proton, energy is required in order for

---

[2] An isobar is a sequence of nuclei with the same atomic mass (A), where the atomic mass may be defined in terms of the proton number, (Z) and neutron number, (N) as A=Z+N.

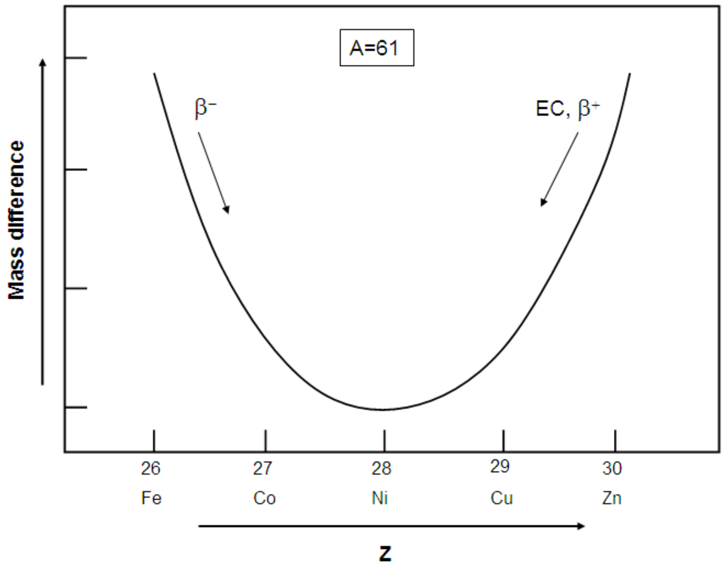

Figure 2.2: Diagonal cross-section through the valley of stability showing the A=61 isobar in terms of mass difference (excess energy) and proton number, Z. β^+ decay and electron capture act from the right to reduce Z towards stability while β^- decay acts in the other direction to increase Z.

the process of β^+ emission to take place. β^+ decay can therefore only occur inside a nucleus when the absolute value of the binding energy of the daughter nucleus is higher than that of the parent. In the example of the β^+ decay of ^{22}Na, the equation of the process is given by

$$^{22}_{11}Na \rightarrow^{22}_{10} Ne + \beta^+ + \nu. \tag{2.2}$$

The available excess binding energy, known as the Q-value, is shared between the recoiling daughter nucleus, the positron and the neutrino. The emitted β^+ particle therefore carries off some of the available energy ranging from almost zero up to a specific maximum value which is dependent on the parent nucleus involved in the decay. This end-point energy can be defined as

$$E_{\beta^+max} = Q - 2m_0c^2 - E_i \tag{2.3}$$

where E_i is the energy level to which the decay occurs and m_0 is the rest mass of the electron. As a result, β^+ decay can only occur if

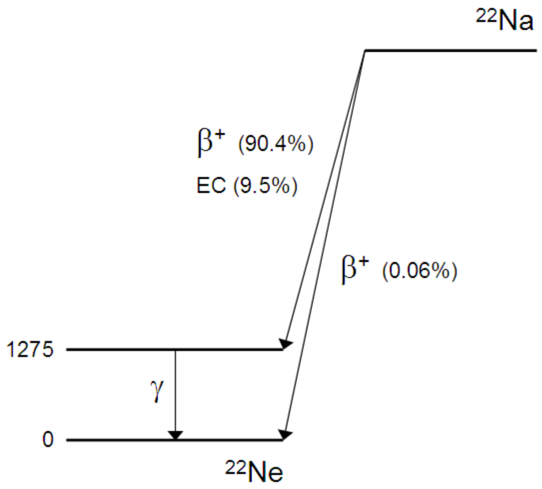

Figure 2.3: Decay scheme for the positron emitting radioactive nucleus ^{22}Na. The intensities of the β^{+} and electron capture (EC) branches are indicated as percentages. The Q value for this decay is 2.84MeV [Fir96].

$$Q - E_i > 2m_0c^2. \tag{2.4}$$

Throughout this work the positron emitting radionuclide ^{22}Na is used. The energy level diagram for ^{22}Na ($t_{\frac{1}{2}}$=2.6 years) is shown in Figure 2.3. The main β^{+} decay branch is to an excited state of the daughter nucleus ^{22}Ne which subsequently decays by emission of a 1275keV γ-ray. In this case, for transitions through the main positron decay branch, the end point energy is 545keV [Nic01].

The competing process of electron capture (EC), which results in energy production, is the conversion, via the weak nuclear force, of an electron and a proton into a neutron resulting in a loss of positive nuclear charge. The electron in question is captured by the nucleus, usually from the innermost orbit (the process is often termed ‘K-capture’) and the following reaction ensues:

$$e^{-} + p \rightarrow n + \nu. \tag{2.5}$$

2.1.1 Positron-Electron Annihilation

Upon emission from a decaying nucleus, a positron will travel through a medium losing kinetic energy via ionisation or elastic scattering, a process known as thermalisation. Within a short range the positron will encounter an atomic electron where an annihilation reaction takes place resulting in the production of (usually) two colinear gamma-rays, each with 511keV of energy.

Prior to the gamma-ray decay, the electron and positron form an intermediate bound state known as positronium. According to [Har04] this state can be thought of as a hydrogen atom with the proton replaced by a positron. Positronium is highly unstable as quantum field interactions between the electron and positron ensure that the particles spiral closer and closer together in discrete quantised steps, until after around 10^{-7} seconds the annihilation takes place. Due to conservation of energy the annihilation gamma-rays carry away 511keV each (twice the rest mass of the electron) with the photons being emitted at roughly 180° to each other in order to conserve momentum.

While Positron Emission Tomography relies on the emission of two colinear 511keV gamma-rays, this is not the only route through which positronium can decay and, in reality, deviations from this model place fundamental restrictions on the performance of PET systems.

Three Photon Decay

In general, we can consider the positron-electron annihilation reaction to produce two gamma-ray photons. However, in a small fraction of cases three photon decay occurs. Essentially, if the particle wavefunctions are symmetric when the positronium forms then decay via two photon emission is forbidden. Three photon decay however is not forbidden, as the atom may exist in either a singlet or longer lived triplet state known as Para-Positronium and Ortho-Positronium respectively [Cha00] where radiative transition from one state to another is forbidden. Calculations have shown that the ratio of three-photon emission to two-photon emission is around 1:370 [Web00]. It has even been suggested that the three-photon decay could be used in PET to provide a more accurate description of source location [Kac04], [Kac05]. This is more likely to be of academic than clinical interest

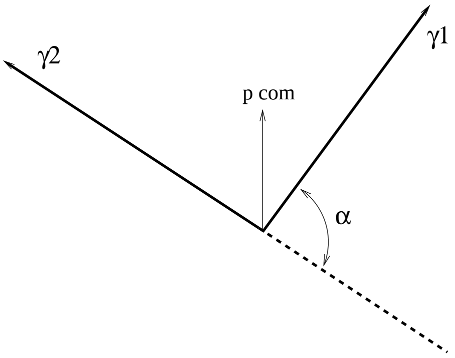

Figure 2.4: Coordinate system defining the angle of non-colinearity between annihilation photons.

however due to the small percentage of events where the decay mode occurs.

Non-Colinearity of Gamma-Rays

It has been stated previously that for two-photon positronium decay, conservation of momentum ensures that the gamma-rays are emitted at 180° to each other. This assumes that the positron and electron are at rest when the annihilation occurs - a scenario which is unlikely to be true. As a result an angle of non-colinearity can be defined which depends upon the momentum of the centre of mass at the time of annihilation.

From momentum conservation the angle of non-colinearity, α, defined in Figure 2.4 is found to be

$$\alpha = 2 \arcsin \left(\frac{E_{\beta+}}{\sqrt{2E_{\beta+}}} \right) \tag{2.6}$$

where $E_{\beta+}$ is the energy of the positron. The value of α is typically quoted as $\pm 0.25°$ [Che04] for typical clinical positron emitters.

This non-colinearity acts to degrade the spatial resolution of a PET image by increasing the uncertainty in identifying the position of annihilation. The contribution to position uncertainty is independent of isotope, instead varying with the system geometry, at the centre of the detectors according to

$$X = \frac{\alpha D}{2} \tag{2.7}$$

where X is the uncertainty in position and D is the diameter of the ring of detectors (assuming a standard PET camera configuration). The blurring effect induced by this uncertainty can be modelled as Gaussian broadening [Lev99] of the form

$$N\left(x\right) = A\exp(\frac{-x^2}{2\sigma^2}) \tag{2.8}$$

where the Full Width at Half Maximum (FWHM) of this Gaussian is given by

$$FWHM = 2.35\sigma = 0.0022D. \tag{2.9}$$

This limits the spatial resolution achievable in typical human and small animal PET systems to ∼2mm and ∼0.5mm based on typical diameters of 80cm and 17cm respectively[3].

Positron Range Blurring

In the discussion of positron-electron annihilation it has been stated that the positron travels a certain range through a given medium before positronium is formed. This produces a blurring effect on the localisation of a point source as there is an intrinsic discrepancy between the position of positron emission and that of positronium decay. In contrast to non-colinearity effects, the contribution to position uncertainty which positron range blurring introduces is independent of system geometry and depends only on the energy spectrum of the emitted positrons and therefore the isotope in question. The positron range clearly varies from isotope to isotope and typically limits the spatial resolution to between 0.5mm and 1mm for common low energy positron emitters such as ^{18}F [Lev99]. It is the quadrature sum of the blurring effects associated with these two artefacts of positron physics which place the fundamental limit on the spatial resolution achievable in any PET image [Mos93].

2.1.2 Coincident Event Categories

In addition to the considerations of three photon decay, gamma-ray non-colinearity and positron range blurring, the performance of a PET system is influenced by its ability to

---

[3] The ECAT EXACR HR+ and Biograph 2 clinical PET scanner have internal diameters of 82.4cm and 82.5cm respectively [Kar06] while the microPET system for small animal PET has an internal diameter of 17.2cm [Che97].

correctly identify and use coincident events. Generally, this will depend on the systems intrinsic timing and energy resolution. If one assumes that two photons must be detected within a given time window with each passing an energy gate in order for them to be considered to have occurred in coincidence, for a typical PET system these events may be categorised in the following way:

i. True Coincidence

A true coincident event is said to occur when two photons resulting from the same positron-electron annihilation are detected within the coincidence time window and both pass the energy requirement. This type of event is ideal for imaging as the LoR will be defined as accurately as is possible. Poor energy resolution may give rise to a scenario in which scattered photons still pass the energy requirement despite their reduced energy. This is discussed in more detail below.

ii. Random Coincidence

When two photons passing the energy criteria are detected within the defined time window, but these photons do not originate from the same annihilation reaction, a random coincidence is said to have occurred. The random coincidence count rate varies as a function of source activity and the coincidence time window. The random coincidence count rate between two detector elements (R_{ab}) may be estimated from Equation 2.10 where N_a and N_b are the singles count rates from each element and 2τ is the width of the coincidence window [Tar03]. It can be seen from this equation how, in a system providing good timing resolution, the coincidence window may be reduced, thus reducing the random coincident count rate. A further reduction may also result from the ability of a system to reject contributions from background gamma rays based on energy discrimination.

$$R_{ab} = 2\tau N a N_b. \tag{2.10}$$

iii. Scatter Coincidence

As Compton scattering is the dominant interaction process at 511keV (the energy of interest for PET) a significant fraction of events are likely to undergo scattering in the patient or subject (depending upon patient/subject size) prior to impinging on the detectors. The Compton scattering process results in a photon changing direction and losing energy. If either of the annihilation photons scatters in the subject before detection, this change of direction will result in incorrect LoR definition. The fraction of these event included in a data set for image reconstruction may be reduced by vetoing events on the basis of energy (as the Compton scattered photons will have an energy <511keV). However, as the energy resolution of conventional PET systems is extremely poor it is likely that this type of event constitutes a significant percentage of those used for imaging. Clearly, the scatter coincidence count rate is dependent on the amount of scatter material surrounding the source and therefore has much greater implications for human PET than small animal imaging.

iv. Multiple Coincidence

A multiple coincidence occurs when more than two photons are detected within the time window. These events are generally rejected. Detector systems providing increased granularity (or position sensitivity) and improved energy resolution have the potential to discriminate between interactions, identifying the true annihilation photons and thereby increasing statistics in the reconstruction data set.

Generally speaking, in any PET scan the data set is made up almost exclusively from true, random and scatter coincidence. For a typical whole-body clinical PET scan operating in 3D mode[4] , the relative fractions of these events is displayed in Figure 2.5 as described by [Mos03]. It can be seen how true coincidences make up only 25% of the data set with twice as many random events occuring. In a small animal PET system these numbers are likely to be very different with the scatter event rate being quoted as 11% of the total true event rate for a standard mouse phantom by Huber and Moses in [Hub99]. In the majority of work presented here true coincident events are expected to contribute almost 100% of the total counts. In most cases the activity of the sources is sufficiently low as to ensure

---

[4] For a typical FDG brain scan, a total activity of around 250MBq is delivered [Val03] while a coincidence window of 6ns is typical for an Lutetium Oxyorthosilicate (LSO) based commercial PET system [Tar03].

the random rate is negligible and the presence of little or no scatter material ensures the scatter fraction remains small.

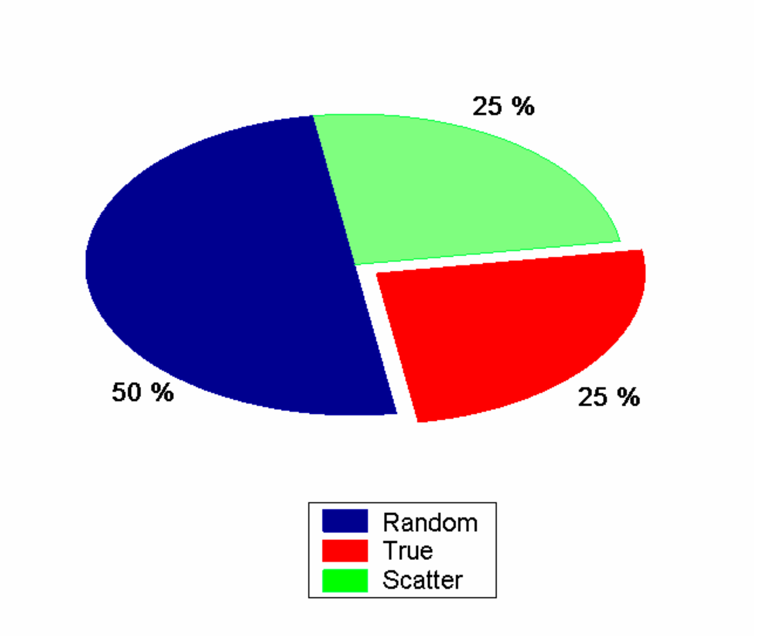

Figure 2.5: Pie chart showing the relative contribution to a clinical, whole-body, 3D PET data set made by true, random and scatter coincidences.

As the inclusion of random and scattered coincident events will ultimately degrade the quality of a reconstructed image, PET systems attempt to reduce the relative fractions of these events. This is generally achieved through the optimisation of timing resolution to reduce the number of random coincidences. The rejection of scattered coincidences may be achieved through improved energy resolution. From [Mat06] energy resolution considerations result in typical scintillator PET systems being unable to identify scatters through angles below ∼60°. The same calculation for a Ge based system yields a value of 5°.

2.2 Small Animal PET

Positron Emission Tomography has been used as a clinical imaging tool in one form or another for over 35 years. More recently (∼10 years), improved detector and software technology has given rise to an increased use of PET in small animal imaging studies. Small animal imaging is commonly used in medical research and pharmaceutical development in order to understand disease process and evaluate potential therapies. The advent of the first dedicated small animal PET system in 1992 allowed non-invasive studies to be carried out and paved the way for academic research into such systems. In human PET a spatial resolution of ∼5-8mm is typically required for brain imaging while ∼8-15mm is sufficient for the rest of the body. Due to the size of the subjects, small animal PET systems must provide much finer spatial resolution while maintaining good detection efficiency. With conventional detector technology such as scintillators, this improvement in position sensitivity can only be achieved by producing ever smaller detector elements which has the unwanted side effect of decreasing the output signal to noise ratio and limiting the efficiency of each individual detector element. Despite this, like their clinical counterparts the majority of commercially available small animal PET systems still rely on scintillation detectors though the QuadHIDAC [Mis04] utilises High Density Avalanche Chambers and applies specially developed reconstruction algorithms [Wal01] in order to achieve very fine spatial resolution. Improvements in semiconductor fabrication techniques and the availability of fast digital electronics have recently made the development of prototype semiconductor based systems a reality [Phi02]. In terms of detection efficiency, semiconductor tomographs currently under development appear to follow one of two common schools of thought, either opting for detectors with a high or low photofraction [Sen07]. This has resulted in a diversity of designs ranging from many layers of very thin silicon detectors to more standard geometries employing higher density Cadmium Zinc Telluride (CZT) detectors. The use of planar germanium detectors lies somewhere in between these two extremes providing reasonable stopping power and the potential for excellent position sensitivity. According to [Che01], the future of small animal PET looks promising with the quest for optimum spatial resolution still an important research objective.

2.3 Image Reconstruction

Image reconstruction is the process through which information from the Lines of Response (LoR) are used to produce a clinically useful diagnostic image. The lack of a single, ideal reconstruction method has resulted in the development of a range of techniques, each with their relative merits. In general, these methods may be said to fall into one of two distinct categories; Analytic or Statistical methods. This section describes the principles and applications of image reconstruction by considering the most common technique from each class, Filtered Backprojection (FBP) [Cor63] and Maximum Likelihood Expectation Maximisation (MLEM) [She82].

2.3.1 The Sinogram and Radon Transform

The fundamental LoR data acquired from a PET scan may be represented in the form of a Sinogram which forms the basic input to the reconstruction algorithm.

If we consider a LoR, $L_{d_a d_b}$, defined between two detector elements d_a and d_b, the number of counts along this LoR (the number of coincidences between elements d_a and d_b) is a Poisson variable with a mean value $\langle P_{d_a d_b} \rangle$ given by:

$$< P_{d_a d_b} >= \tau \int dr f(r) \psi_{d_a d_b}(r) \tag{2.11}$$

Where $f(r)$ is the time-independent tracer distribution and τ is the acquisition time. $\psi_{d_a d_b}(r)$ is a sensitivity function included to take account of the removal of scattered coincidence and random coincidence events which results in the data set including only true coincident events occurring along the LoR $L_{d_a d_b}$. This sensitivity function has a value of zero everywhere except along the LoR. The equation then simplifies to:

$$< P_{d_a d_b} >= \tau \int dr f(r) \tag{2.12}$$

which is the line integral of the positron decay distribution along the LoR in question.

During PET data acquisition, the detector system is rotated around the subject. If we consider this rotation to be performed in discrete, equally spaced angular increments, the angle of rotation from a defined x-axis at any moment is given by ϑ. The combination of each of the parallel beam LoRs thus forms a one dimensional projection of the source $p_\vartheta(t)$ for every angular position where t is the position along the projection axis. This is illustrated in Figure 2.6 where two independent one dimensional projections of a two dimensional source distribution are made.

By combining these one-dimensional projections for $180° \geq \vartheta \geq 0°$, a two dimensional representation of the source distribution, $p(t,\vartheta)$ is produced. This is known as a sinogram

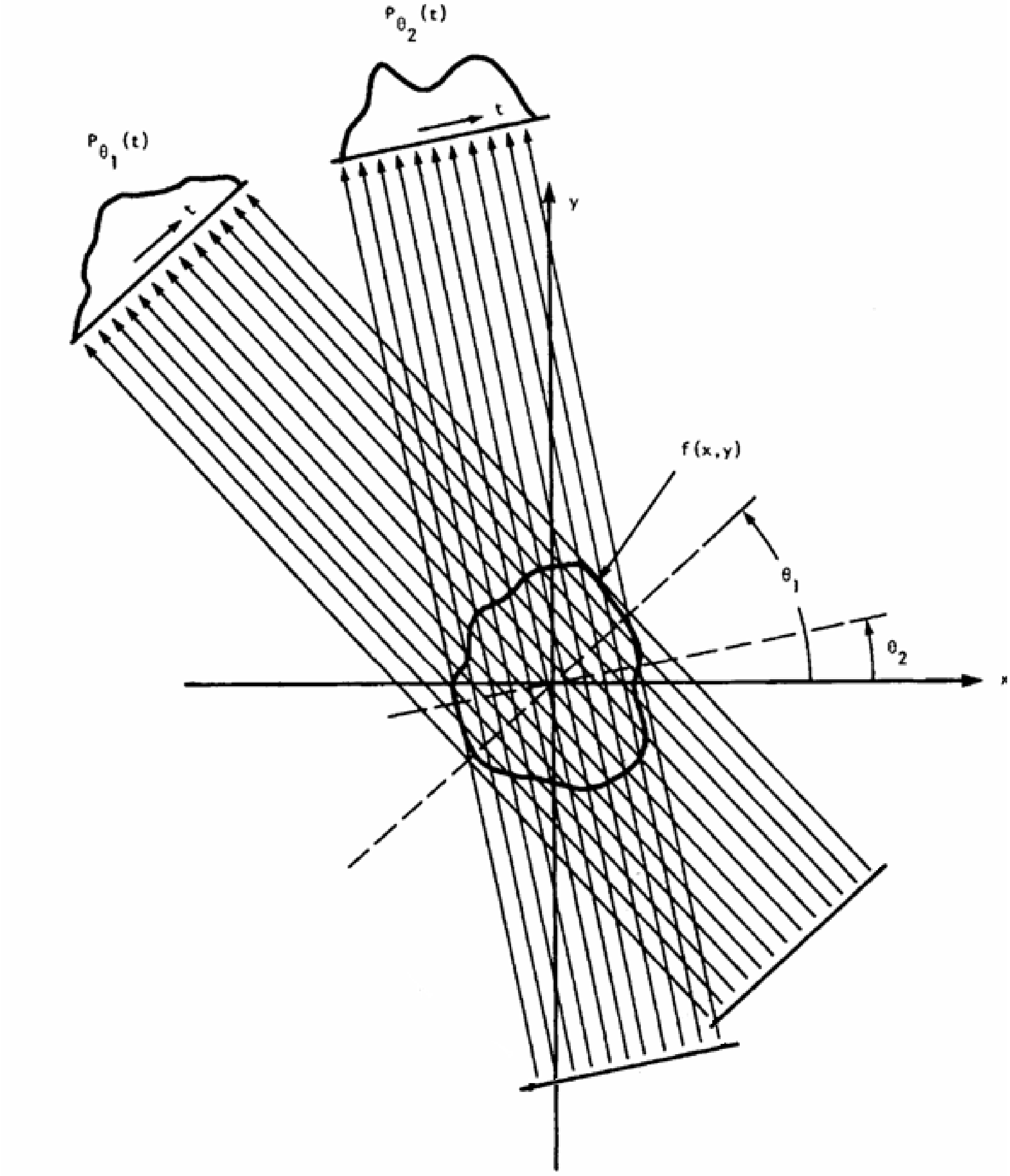

Figure 2.6: A uniform source distribution $f(x, y)$ is sampled at two angles θ_1 and θ_2 resulting in two one dimensional projections, $p_{\theta_1}(t)$ and $p_{\theta_2}(t)$ where t is the coordinate along the projection axis. To fully sample the source distribution projections covering the range $0^o \leq \theta < 180^o$ are required. Figure reproduced from [Kak89].

and tomographic image reconstruction may be understood to be the process of calculating the 2D source distribution *f(x,y)* from knowledge of the sinogram *p(t,ϑ)*.

In the example provided by Figure 2.6 the one dimensional projections are composed of equally spaced (parallel beam) LoRs. In the case of the SmartPET system these would correspond to LoRs defined only between directly opposite pixels. In most practical applications interpolation methods are employed in order to recover a Cartesian grid after the inclusion of non-parallel beam LoRs. The current algorithm implementation for SmartPET allows only the inclusion of parallel beam LoRs [Mat06].

Johann Radon [Rad17] solved the mathematical problem of two dimensional reconstruction from an infinite number of one dimensional projections in 1917, many years before it found application in the fields of Computed Tomography (CT) and PET.

[Rad17] defines the Radon Transform of a distribution $f(x, y)$ along a line l as

$$p(t, \vartheta) = \int f(x, y) dl. \tag{2.13}$$

Geometric transforms imply that all points on this line must satisfy the equation t=xcos(ϑ) + ysin(ϑ), therefore the Radon Transform may be redefined as:

$$p(t, \vartheta) = \int \int f(x, y) \delta(x \cos(\vartheta) + y \sin(\vartheta) - t) dx dy \tag{2.14}$$

Consequently, solving the inverse Radon Transform from knowledge of the sinogram provides a solution for recovering the source distribution *f(x,y)*.

2.3.2 Filtered Backprojection (FBP)

The most basic reconstruction technique which may be applied is that of simply projecting the measured LoR values back into image space. For a continuous data distribution (an infinite number of LoRs) in the range 0°≤ ϑ≤180° backprojection is defined mathematically by:

$$f_{BP} = \int p(x \cos \vartheta + y \sin \vartheta, \vartheta) d\vartheta. \tag{2.15}$$

This approach is referred to as Simple Backprojection (SBP). While this technique provides a straightforward methodology for reconstruction, the resulting images exhibit considerable blurring as the sinogram is effectively convolved with a 1/r distribution. In order to overcome this, SBP may be adapted to include filtering which aims to remove this blurring effect. This is achieved by convolving the projection data in frequency space with a filter which may be optimised to promote or suppress specific spatial frequencies. This technique is known as Filtered Backprojection and is the most widely employed analytic image reconstruction technique.

Fine detail in a reconstructed image is represented as high spatial frequency components, implying that any filter should aim to preserve high frequencies at the expense of the lower frequency elements. However, statistical noise also exists in the high spatial frequency domain and thus any sharpening of an image achieved through high pass filtering may result in degradation of the signal to noise ratio. The ensuing trade off has resulted in the development of a range of filters, the relative merits of which are discussed in more detail in [Mat06].

Due to its speed and simplicity FBP remained the standard reconstruction technique for many years. For the development of a detection system it also remains an important performance indicator as it provides a linear response to improved data and/or the physical characteristics of the detection system. It does however suffer from serious limitations in its performance in low statistics scenarios or where the number of LoRs generated is small.

2.3.3 Maximum Likelihood Expectation Maximisation (MLEM)

The poor performance of analytic reconstruction techniques such as FBP under certain conditions fuelled the need for algorithms which produced accurate, high quality images from data which may be of varying quality. As a result, statistical reconstruction techniques take a different approach than their analytic counterparts. These algorithms make an initial estimate of the image (often a uniform distribution where each pixel is equal to unity). Next, a forward projection technique is used to calculate the expected values and the estimate is updated through the backprojection, into image space, of a correction factor. This process is repeated, the estimate of the image improving every time, until some convergence criterion is met. It is this repetitive nature which gives rise to the term ‘iterative’ image reconstruction and makes such algorithms computationally intensive. Maximum Likelihood Expectation Maximisation is the most widely implemented statistical reconstruction algorithm, and like the majority of iterative techniques, relies on the generation of a so called ‘system matrix’ or ‘system model’ [Rea02]. The system matrix is effectively a probability matrix which describes the likelihood that a decay in a given pixel will be measured by a given LoR. This matrix must contain calculations for all possible pixel-LoR combinations. While a simple system matrix may calculate probabilities based only on geometrical considerations, it is possible to include the physics of a given source distribution or detector geometry to account for, for example, Compton scattering and gamma-ray attenuation. The quality of an image reconstructed using MLEM essentially hinges on the ability of the system matrix to accurately model the physical system and as such the development of suitable approaches is a research field in its own right [Par04].

The MLEM approach to tomographic reconstruction is an extension of the concept that the number of counts in a LoR varies according to Poisson statistics. The number of counts m_i measured along a LoR i is distributed, according to Poisson statistics as:

$$Pr(m_i|q_i) = \frac{q_i^{m_i} exp[-q_i]}{m_i!} \tag{2.16}$$

where q_i is the mean of the distribution and $Pr(m_i|q_i)$ is the probability of measuring m_i given a mean q_i. The MLEM algorithm then converges on the most likely image vector $\left\{n_j^k\right\}$ to have yielded the data set $\{m_i\}$.

The value of a pixel in a given iteration is related to the value in the next iteration through the application of a correction factor, updating the image according to the MLEM equation:

$$n_j^{k+1} = \frac{n_j^k}{\Sigma a_{ij}} \sum a_{ij} \frac{m_i}{q_i^k} \tag{2.17}$$

where

$$q_i^k = \sum a_{ij} n_b^k \tag{2.18}$$

As the MLEM approach to image reconstruction enables images of relatively high quality to be produced from data which may suffer from low statistics or high noise content it is not employed through the majority of this work. A more linear relationship between data quality and image quality exists for FBP algorithms and as such the images presented here will, for the most part, be reconstructed using this technique.

Chapter 3

Principles of Radiation Detection

3.1 The Interaction of Gamma-Rays with Matter

The principle of operation of a spectroscopic radiation detector is the generation of a response which is in some way proportional to the energy of the incident radiation. This takes the form of an electrical current, induced by the liberation of charge carriers within the detection medium, by the interacting radiation. It is therefore essential to have a good appreciation of the major interaction mechanisms and detection principles if one is to fully understand the response of the detector. This section will discuss the major gamma-ray interaction processes and how this facilitates the generation of both primary and secondary charge carriers.

Photons interact with matter by transferring some percentage of their energy to the atomic electrons of the material through which they are travelling. While there are several interaction processes which may take place (Rayleigh Scattering, Thompson scattering etc.) there are three major mechanisms which dominate in the energy range from $\approx 10keV$ to a few MeV. These mechanisms are; photoelectric absorption, Compton scattering and pair production. The respective energy ranges over which these processes are most dominant are illustrated in Figure 3.1. The plot shows how the relative importance of each interaction process varies as a function of atomic number and energy. It can be seen how for a material such as germanium with Z=32, the photoelectric effect is dominant at gamma-ray energies less than around 200keV. For energies between 200keV and 2MeV Compton scattering is the most important mechanism while above 6MeV pair production begins to dominate.

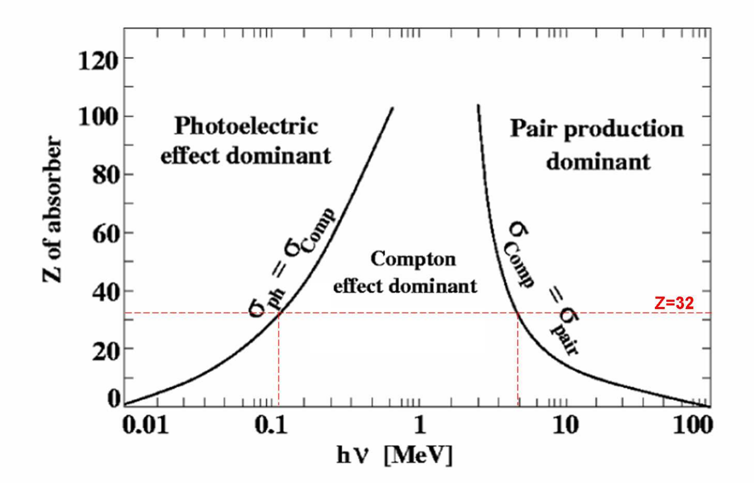

Figure 3.1: The dominant gamma-ray interaction mechanisms as a function of energy ($h\nu$) and atomic number (Z). The solid black lines show the values of Z and $h\nu$ for which the two neighbouring effects are equal. The broken line denotes the atomic number of germanium, Z=32, and shows the energies at which each interaction mechanism becomes dominant for this material. Reproduced from [Kno99].

3.1.1 Photoelectric Absorption

In germanium, photoelectric absorption is the dominant interaction mechanism for gamma-rays with energy up to 200keV. This process occurs when an incident photon interacts with a bound atomic electron (usually a K-shell electron) transferring all its energy to the electron. This electron (the photoelectron) is then ejected from the target atom with energy, E_e, given by

$$E_e = E_\gamma - E_b \tag{3.1}$$

where E_b (E_b=12keV for germanium) is the binding energy of the electron and E_γ is the energy of the gamma-ray photon.

As a result of this process, a vacancy will be left in one of the electron shells. This hole will subsequently be filled by an electron from a higher lying shell resulting in the emission of an x-ray in a process known as x-ray fluorescence.

It is not possible to define a single function which describes the cross section for photelectric absorption taking place over all ranges of energy and atomic number (Z), but in

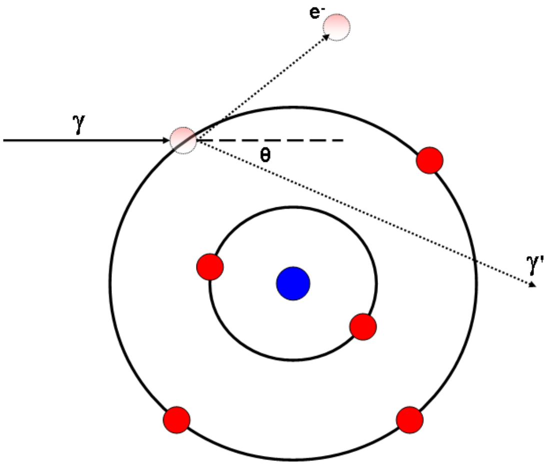

Figure 3.2: Depiction of a gamma-ray undergoing Compton scattering.

general, it can be shown to vary as:

$$prob_{pa} \propto \frac{Z^n}{E^{3.5}} \tag{3.2}$$

where n is between 4 and 5.

3.1.2 Compton Scattering

Compton scattering, the dominant interaction process for photons in the energy range of ≈200keV to 5-6MeV, involves the transfer of a fraction of the gamma-ray energy to a weakly bound atomic electron. This results in the ejection of this recoil electron and the scattering of the photon through an angle ranging from 0° to 180°. This angle is derived from the conservation of energy and momentum laws according to

$$E_\gamma^{'} = \frac{E_\gamma}{1 + \frac{E_\gamma}{m_0 c^2}(1 - \cos\vartheta)} \tag{3.3}$$

Where ϑ is the scattering angle and m_0c^2 is the rest-mass of the electron (511keV). The scattering process results in the gamma-ray photon having reduced energy ($E_\gamma^{'}$) where this energy is dependent on the angle through which it scatters. The maximum energy transfer occurs at a scattering angle at 180° with the minimum at 0°. This type of gamma-ray interaction is illustrated schematically in Figure 3.2.

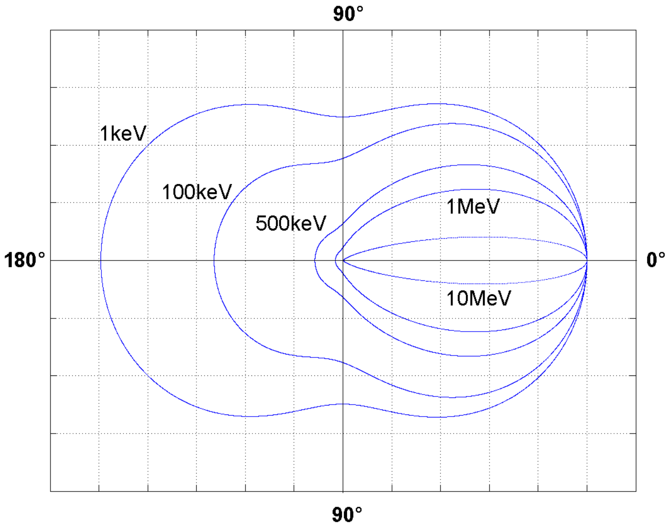

Figure 3.3: Polar plot showing the Compton scattering cross-section against deflection angle for a range of initial gamma-ray energies. At 500keV forward focussed scattering is highly probable.

The probability of a gamma-ray undergoing Compton scattering increases linearly as a function of Z as the increasing atomic number serves to maximise the number of scattering targets. The angular distribution of scattered gamma rays incident on a single electron is described as a function of energy by the differential Compton scattering cross-section or Klein-Nishina formula [Kle29]. Here, the differential scattering cross section with respect to the solid angle is given by

$$\frac{d\sigma}{d\Omega} = Zr_0^2 \left(\frac{1}{1+\alpha\left(1-cos\theta\right)}\right)^2 \left(\frac{1+cos^2\theta}{2}\right) \left(1+\frac{\alpha^2\left(1-cos\theta\right)^2}{\left(1+cos^2\theta\right)\left[1+\alpha\left(1-cos\theta\right)\right]}\right) \quad (3.4)$$

where $\alpha \equiv h\nu/m_0$c^2 and r$_0$ is the classical electron radius.

The distribution of the Klein-Nishina equation is displayed graphically in Figure 3.3.

3.1.3 Pair Production

The final interaction mechanism in this energy range is that of pair production. A gamma-ray undergoing pair production disappears completely in the Coulomb field of a target atom resulting in the production of an electron-positron pair. It is therefore energetically possible when the energy of the incident gamma-ray (E$_\gamma$) is greater than twice the electron rest mass

(E_γ >1.02MeV) however the probability remains small below 2.0MeV. For a pair production event the remaining gamma-ray energy above the 1.02MeV threshold is shared between the electron and positron in the form of kinetic energy according to

$$E_{e^-} - E_{\beta+} = E_\gamma - 2m_0c^2 \tag{3.5}$$

where $2m_0c^2 = 1.02$MeV

3.2 Semiconductor Gamma-Ray Detectors

In order to maximise detection efficiency the use of a solid state material for the formation of gamma-ray detectors is usually favourable. Equivalent gas based detectors may be up to three orders of magnitude less dense resulting in much decreased stopping power.

For many years inorganic scintillation detectors such as Sodium Iodide (NaI) and Bismuth Germinate (BGO) have found widespread application as gamma-ray detectors in fields including nuclear physics and medical imaging. Scintillation counters, while exhibiting high stopping power, provide limited energy resolution due to the many inefficient steps involved in converting the incident gamma-ray energy to a proportional electrical signal. In the early 1960s the development of semiconductor technology and the evolution of fabrication techniques led to increased availability of practical semiconductor detectors which provide much improved energy resolution. As a result, Silicon and Germanium detectors have long been the detectors of choice for the majority of nuclear physics and particle physics applications.

3.2.1 Semiconductor Materials

In any crystalline material, the periodic lattice defines a particular band structure which establishes the allowed electron energies. This band structure gives rise to the electrical properties of the material and in general allows solid state substances to be classified as either insulators, conductors or semiconductors.

In a conducting material the conduction band is either partially filled or the valence band and conduction band overlap. The lack of a band gap (region of non-allowed electron energies) allows electrons from the valence band to move up into the conduction band with only a small gain in kinetic energy. In a conducting material this kinetic energy is typically provided by an applied electric field and facilitates current flow. In contrast, an insulating material exhibits a large band gap which is larger than the thermal energy of an electron. As a result, even in the presence of an applied electric field, valence electrons may not be promoted into the conduction band and current will not flow. Semiconductor materials may be considered to be the intermediate case where the band gap is extremely small (typically around 1eV) and thermal excitation of valence electrons can result in promotion to the conduction band. At low temperatures semiconductor materials act as insulators, but at room temperature and above the thermal energy is an appreciable fraction of the band gap energy resulting in a significant number of electrons being promoted to the conduction band. Hence, application of a small applied potential results in current flow.

The electrical properties of a semiconductor material can be explained in terms of its band structure, described by the relationship between energy E and effective momentum k. Figure 3.4 shows the band structure of germanium. The shaded region corresponds to the band gap while the E-k contours of the conduction band and valence band are shown above and below the band gap respectively. In investigating the electrical properties of this semiconductor, the characteristics of the E-k relationship near the top of the valence band and the bottom of the conduction band are of interest. In the case of germanium, the bottom of the conduction band occurs where the value of effective momentum is non-zero, classifying the material as an indirect semiconductor. In all indirect semiconductors, when an electron makes the transition from the maximum point in the valence band to the minimum point in the conduction band, it requires not only a change in energy but also some momentum change.

3.2.2 Charge Carrier Concentration

An intrinsic semiconductor can be defined as having an equivalent number of electrons in the conduction band as holes (vacancies) in the valence band. The charge carrier concentration can therefore be described by

$$n = p \tag{3.6}$$

where n is the concentration of electrons in the conduction band and p the concentration of holes in the valence band. In reality, fabrication of this type of semiconductor is

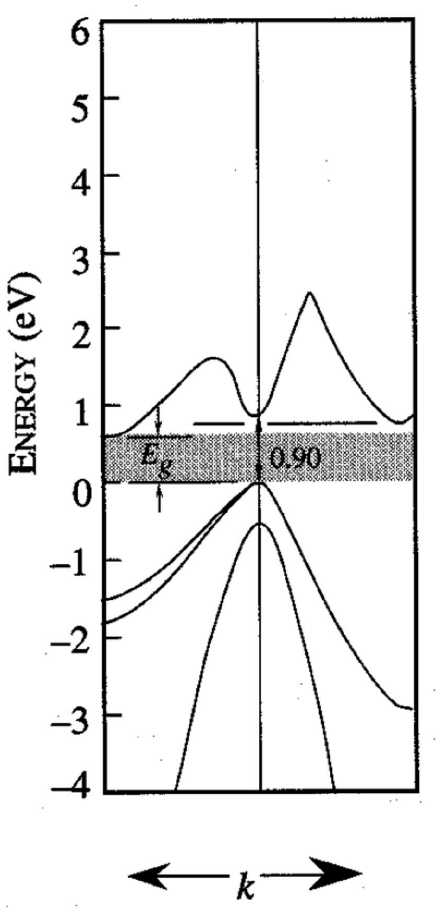

Figure 3.4: The band structure of the semiconductor material germanium in terms of the relationship between electron energy and effective momentum, k. The shaded region corresponds to the region of forbidden energies or band gap. The conduction and valence bands are therefore represented by the regions above and below the bandgap respectively.

virtually impossible [Sze02] therefore the electrical properties of real semiconductor materials tend to be influenced by the presence of chemical impurities. In many applications additional impurities may be introduced in order to specifically modify the electrical properties. Such materials, where the number of impurities is large compared with thermally generated electrons and holes, are known as extrinsic semiconductors and have a charge carrier concentration defined by

$$n \neq p. \tag{3.7}$$

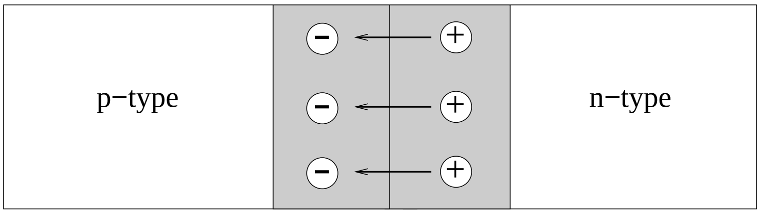

Figure 3.5: Schematic representation of a p-n junction showing charge migration resulting in the build up of regions of space charge.

In doping a semiconductor two dopant types may be introduced. These are donor atoms (n-type impurities) which donate an electron to the conduction band and acceptors (p-type impurities) which accept an electron from the valence band thus creating a hole. A donor atom must have one extra electron in its outer shell, relative to the atom it replaces. In a semiconductor material such as germanium, a Group V element such as lithium is a typical example of an n-type dopant. Conversely, a Group III element such as boron may form the p-type dopant for germanium.

The introduction of dopants acts to modify the band gap of a semiconductor thus altering its electrical properties. In the case of n-type (donor) doping, the additional electrons occupy an energy level close to the conduction band resulting in a smaller effective band gap (∼0.01eV in Ge). In general, sufficient thermal energy exists to ensure that all impurities are ionised therefore it can be shown that

$$n = N_D \tag{3.8}$$

where N_D is the donor concentration.

3.2.3 The p-n Junction

The basic operating principle of a semiconductor radiation detector relies on the concept of the p-n junction. In a p-n junction the nature of the dopants is altered across a boundary to create adjoining regions of p and n type material. An unbiased p-n junction is represented schematically in Figure 3.5.

When a good contact is made between the p-type and n-type regions, the increased concentrations of negative charge carriers in the n-type zone and positive carriers in the

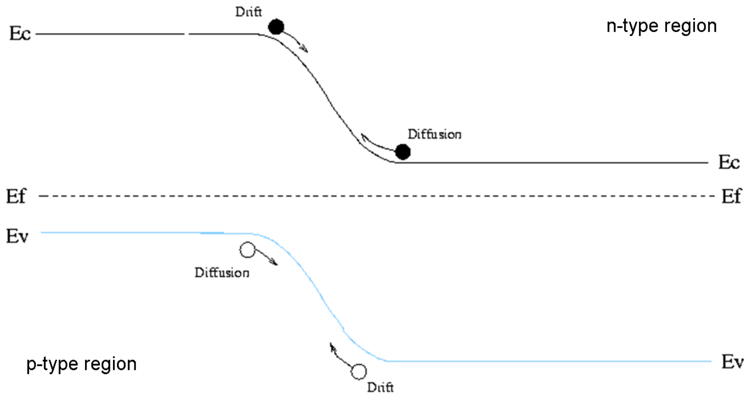

Figure 3.6: Energy band diagram of a p-n junction in thermal equilibrium. E_c and E_v are the energies of the conduction and valence band edges respectively and E_f is the Fermi level.

p-type section results in a large gradient in carrier concentration. This gradient results in carrier diffusion, that is, holes from the p-type side of the junction migrate to the n-type side and vice versa. As this charge diffusion takes place regions of space charge build up on either side of the junction as the migration of holes (electrons) from the p-side (n-side) leaves negative (positive) acceptor ions near the junction. The resulting negative space charge near to the p-side of the junction and positive space charge near the n-side creates a small electric field. This electric field, which is at a maximum at the contact point between the n-type and p-type materials, inhibits the diffusion of charge carriers and results in a dynamic equilibrium being established where the drift current counterbalances the diffusion current. This region free from charge carriers is known as the depletion region and forms the basic component of a gamma-ray detector.

Either side of this depletion region small transition zones are observed where the aforementioned space charge is partially compensated. In reality these regions result in diffuse boundaries between the depletion region and the neutral p and n-type regions but as they are very small compared to the width of the depletion region the geometry may be simplified and boundary conditions describing an abrupt junction may be applied. These boundary conditions can be applied to solve the one dimensional Poisson equation for the built in potential across the boundary. This equation is given by [Sze02] as

$$\frac{d^2V}{dx^2} = -\frac{\rho(x)}{\epsilon} \tag{3.9}$$

where $\epsilon = \epsilon_0 \epsilon_r$ is the dielectric constant of the material and $\rho(x)$ is the charge density.

Increasing this built in potential (V_{bi}) therefore clearly increases the depletion width. The total depletion layer width is given by

$$W = \sqrt{\frac{2\epsilon}{q}\left(\frac{N_A + N_D}{N_A N_D}\right) V_{bi}} \tag{3.10}$$

where N_A and N_D are the concentration of acceptor and donor impurities respectively.

If a semiconductor p-n junction is to be used as a radiation detector the depletion region must be made as large as possible to maximise the sensitive region of the device. In order to preserve the proportional response of the detector it is also essential that the charge carriers liberated following a gamma-ray interaction do not recombine. Both of these requirements can be met by application of a reverse bias across the p-n junction. The width of the depletion region as a function of applied reverse bias can now be given by

$$W \cong \sqrt{\frac{2\epsilon V_{bias}}{q N_{imp}}} \tag{3.11}$$

where, in the case of a semiconductor detector, N_{imp} is the chemical impurity concentration.

Typically, the reverse bias is increased until the depletion region extends through the full volume of the junction and the so called depletion voltage (V_d) is reached. The operating voltage of a radiation detector is usually larger than the depletion voltage in order to ensure saturation of charge carrier drift velocity and hence optimise charge collection performance.

From Equation 3.11 one can observe how the size of the depletion region, and therefore the active volume of a germanium detector varies as a function of the square root of both the applied bias and one over the square root of the impurity concentration. Hence, the values of V_{bias} and N_{imp} place fundamental limits on the dimensions of germanium detectors, the implications of which will be discussed in more detail in the next section.

3.3 High Purity Germanium Detectors

Germanium has been the workhorse of gamma-ray spectroscopy for many years, mainly due to its excellent energy resolution and relatively good efficiency. This energy resolution is

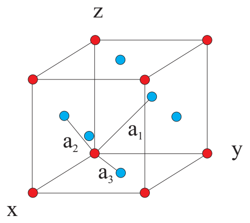

a) Germanium crystal structure

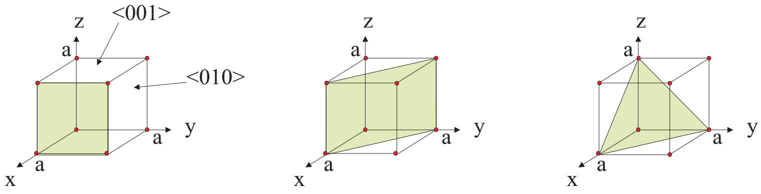

b) <100> plane c) <110> plane d) <111> plane

Figure 3.7: Figure showing the crystal structure of germanium. Image (a) shows the Face Centered Cubic (FCC) structure of germanium while (b),(c) and (d) denote the lattice planes <100>, <110> and <111> respectively in terms of Miller indices [Kit76].

superior to that of scintillation detectors due to the number of charge carriers liberated as a result of a gamma-ray interaction.

A scintillator may typically require $\approx 100eV$ for the liberation of a charge carrier where the semiconductor nature of germanium and small energy gap mean only $\approx 3eV$ is required to promote a charge carrier from valence band to conduction band. Consequently, for a given gamma-ray interaction, a larger number of 'information carriers' are produced per unit energy deposited in a germanium detector as opposed to a scintillation detector. The inherent statistical fluctuations associated with the charge production process place a fundamental limit on the achievable energy resolution and, by increasing the number of information carriers produced per unit energy deposition, this statistical uncertainty is reduced.

Germanium is a group IV element of atomic number 32 and has a face centered cubic (FCC) structure (see Figure 3.7). The electrical properties of germanium are tabulated in Table 3.1.

Atomic Number, A	32
Atomic Weight, Z	72.6
Atoms	4.4×10^{22} cm^3
Density	5.32 g/cm^{-3}
Dielectric Constant, ϵ_r	16.2
Intrinsic Carrier Concentration (300 K)	2.0×10^{13} cm^{-3}
Intrinsic Resistivity	47 Ω·cm
Energy Gap (300 K)	0.67 eV
Energy Gap (0 K)	0.75 eV
Ionisation Energy (77 K), E$_{pair}$	2.96 eV
Electron Mobility (300 K)	3900 cm^{2}V/·s
Hole Mobility (300 K)	1900 cm^2/V·s
Lattice Constant (a)	556.75 pm

Table 3.1: Physical properties of intrinsic germanium [Kno99]

3.3.1 Detector Geometry

A Germanium detector is essentially a fully depleted p-n junction with the volume typically limited by the finite impurity concentration (from Equation 3.11). In order to provide adequate efficiency for stopping intermediate to high energy gamma-rays the depletion width must be at least a few centimeters. This is demonstrated by considering the linear attenuation co-efficient (μ) of germanium for 500keV gamma rays is around 0.5cm^{-1} [Mar00] and the fraction of an incident gamma-ray beam penetrating a material is given by

$$\frac{I(x)}{I_0} = exp(-\mu x). \tag{3.12}$$

If I_0 is the initial intensity and *I(x)* is the intensity remaining at a distance x through an attenuating medium, a simple calculation reveals that around 2.7cm of germanium is required in order to attenuate a beam of 500keV gamma-rays by a factor of four.

In order to achieve depletion regions of this size the impurity concentration must be reduced. In the past this was done by creating a compensated material through the process of lithium ion drifting. More recently, from the 1970s onward [Hal06] crystal manufacture techniques have been developed allowing the fabrication of ultrapure Germanium. These detectors, known as High Purity Germanium (HPGe) detectors typically have impurity

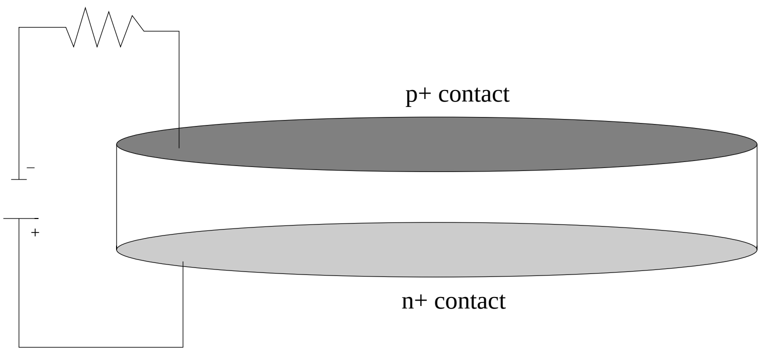

Figure 3.8: Schematic representation of a planar detector.

levels as low as 10^{10} atoms cm^{-3}.

In general we can consider a Germanium detector to have one of two geometries; planar or closed-end coaxial. The following discussion will be limited to that of the planar Germanium detector. Information regarding coaxial Germanium detectors can be found in [Kno99]. A planar Germanium configuration is essentially a wafer of HPGe where the electrical contacts are fabricated on the outer surfaces. A schematic representation is shown in Figure 3.8.

This schematic diagram shows a p-type detector with typical p^+ and n^+ contacts. These contacts are commonly Lithium drifted on the n^+ side with the p^+ side made through Boron implantation. In order to deplete a detector with this configuration a positive high voltage (reverse bias) is applied to the n^+ contact relative to the rectifying p^+ contact. The application of high voltage depletes the crystal from the n^+ face towards the p^+ side. Figure 3.9 shows how the current flow through a p-n junction varies as a function of applied voltage. This figure shows how the current-voltage characteristics display a strongly rectifying behaviour. Under forward bias the current increases exponentially with voltage and becomes strongly conducting. With the application of reverse bias however, the current simply tends toward the saturation current, I_0. In the case of a HPGe detector the saturation current is around 1nA and represents the leakage current observed during normal operation.

In order to avoid dielectric breakdown the maximum reverse bias that may reasonably be applied to a planar germanium detector is limited to a few thousand volts. With this in mind along with the impurity concentration of 10^{10} atoms cm^{-3} stated previously, equation

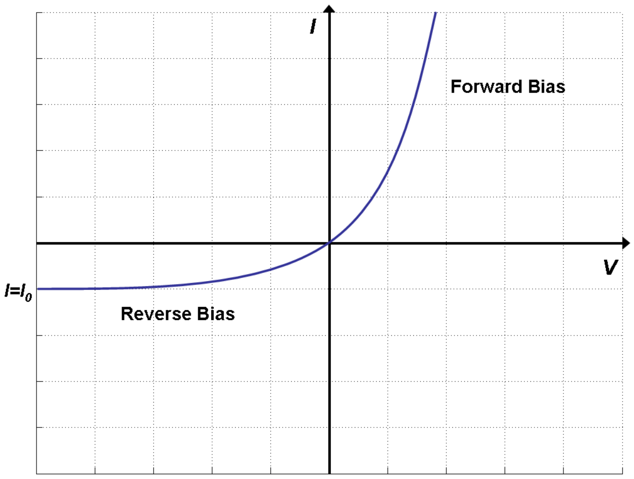

Figure 3.9: The strongly rectifying behaviour observed when applying reverse bias across a HPGe detector.

3.11 limits the maximum active volume of a planar HPGe detector to around 20mm.

3.3.2 Charge Production and Energy Resolution

Following a gamma-ray interaction liberated electron-hole pairs drift toward their respective collecting electrodes under the influence of the electric field. As previously discussed this field ensures that recombination effects are minimised and should ensure that the drift velocity of the charge carriers is saturated. In germanium, a field strength of around 10^4 V/m is required to saturate the drift velocity of electrons at 77K while a factor of three stronger field is typically required for holes [Kno99]. This saturation effect is shown for electrons in Figure 3.10 where one also observes that the drift velocity is maximum along the <100> direction and minimum along the <111> direction. In order for any detector to provide spectroscopic information the number of charge carriers produced must be proportional to the deposited energy. As the number of holes created must be exactly equal to the number of electrons produced the number of charge carriers liberated can be related to the gamma-ray energy by

$$N_{pair} = \frac{E_{\gamma}}{E_{pair}} \tag{3.13}$$

where N_{pair} is the number of electron-hole pairs created for an energy deposition E_{γ}.

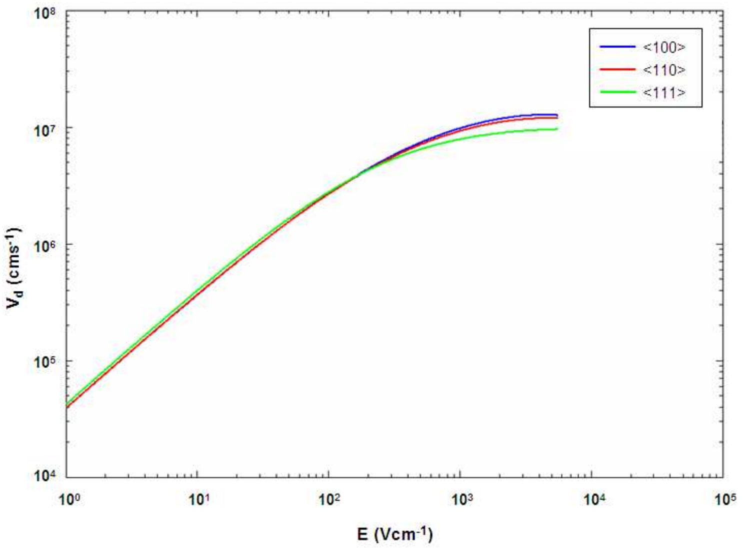

Figure 3.10: Dependence between electron drift velocity and the electric field strength in germanium along the <100>, <110> and <111> directions. The values were calculated according to the Multi Geometry Simulation (MGS) electric field simulation software [Med04].

The E_{pair} term is the ionisation energy required to liberate an electron from a germanium atom.

As E_{pair} is $\approx 3eV$ for germanium, a large number of charge carriers are liberated for a given interaction. If one assumes the creation of individual electron-hole pairs obeys Poisson statistics it can be shown that the associated uncertainty in N_{pair} should simply vary as $\sqrt{N_{pair}}$. The creation of one carrier pair is not independent of the next however and so a correction factor must be introduced to relate the observed variance to the theoretical variance described by Poisson statistics. This factor is known as the Fano Factor and is calculated empirically as the ratio of the observed variance in N_{pair} and the Poisson-predicted variance. In Germanium this value is found to be around 0.08 [Hem95].

In addition to the statistical fluctuations discussed here there are a number of other factors which combine to degrade the energy resolution of Germanium detectors. These are the charge collection efficiency or uncertainty therein and the electronic noise contribution. In general, the three factors can be added in quadrature to give the theoretical full width half maximum of a typical peak as

$$FWHM = \sqrt{W_D^2 + W_x^2 + W_E^2} \tag{3.14}$$

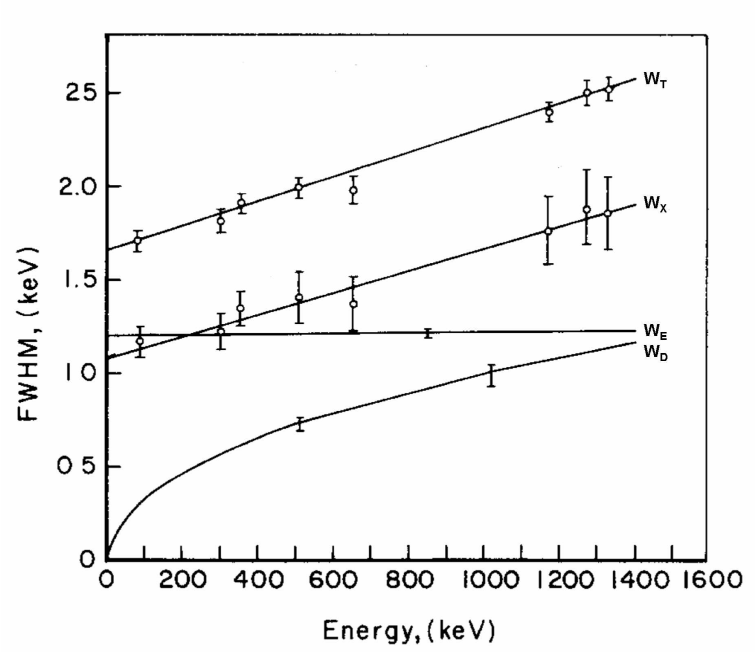

Figure 3.11: Variation of the FWHM of the full energy peak of a HPGe detector with gamma-ray energy. The plot shows the variation of the terms discussed along with the total FWHM, W_T, resulting from the combination of these factors. Reproduced from [Kno99] and [Owe85].

where the W terms are the peak widths that would be observed with no other contributing factors. W_D refers to the combination of statistical uncertainty and Fano factor, W_x is due to incomplete charge collection and, in general should not be a major factor assuming a fully depleted detector with sufficient applied bias and electric field strength. The final term W_E is a result of electronic noise in all system components. The relative role of each factor in degrading the energy resolution varies as a function of gamma-ray energy. For example, at low energies the contribution from electronic noise and collection efficiency dominate the peak broadening while at higher gamma-ray energies the carrier statistics term becomes more significant. This behaviour is illustrated in Figure 3.11.

3.3.3 Signal Generation

In order to build a spectroscopic system the charge carrier production discussed must be measured and quantified. In a germanium detector the movement of electrons and holes towards their collecting electrodes is measured as a current in the circuit external to the detector. The Schockley-Ramo theorem [Sho38] [Ram39] provides a mathematical framework for understanding the current induction process and it may be applied to calculate the magnitude of the instantaneous current as a function of the charge of the carrier (q), the drift velocity (v_d), the intensity of the electric field at the position of the charge (E) and the electric potential of the electrode (ψ) according to

$$i(t) = q\frac{E(x,t)v_d(x,t)}{\psi}. \tag{3.15}$$

Calculations can be simplified by the introduction of the so called weighting field and weighting potential. These non-physical entities which describe the coupling between a charge carrier and a given electrode (in units of cm^{-1}) and vary only with device geometry allow the instantaneous current and charge induced to be computed by treating the problem electrostatically as a function of charge carrier position (x). In order to perform these calculations a number of assumptions must be made:

- The collecting electrode is at unit potential
- All other electrodes are at zero potential
- No space charge is present

While these assumptions are clearly not the case for real devices it has been shown by [He00] that the induced charge on any electrode cannot depend on the applied potentials on each electrode nor stationary space charge. This conclusion has enabled the Schockley-Ramo theorem to be widely applied to advanced semiconductor devices including single polarity charge sensing devices such as Cadmium Zinc Telluride detectors in a coplanar grid configuration [Luk00] and multi electrode germanium detectors [Med04]. The current and charge induced on an electrode by moving charge is then given by

$$i = qv_d.E_0(x), \tag{3.16}$$

$$Q = -q\phi_0(x) \tag{3.17}$$

where ϕ_0 and E_0 are the weighting potential and weighting field respectively. The charge induced on an electrode by moving charge (q) as a function of time (t) can therefore be given by

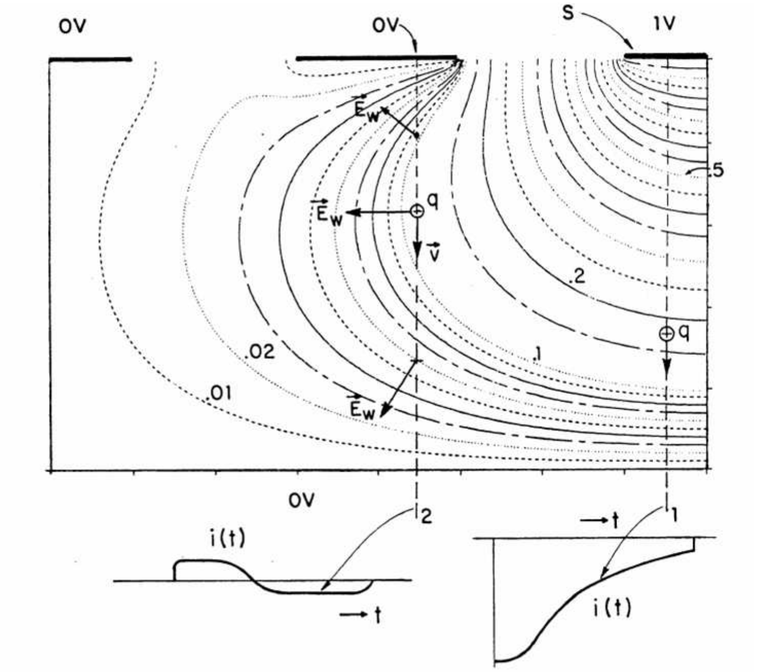

Figure 3.12: Schematic plot of the weighting field in a strip detector [Rad88]. The current pulses induced by the movement of localised charge (q) are shown at the bottom of the figure. For charge travelling along line 1 it can be seen that the current decreases with distance from electrode 1 as the electrostatic coupling decreases. For a charge moving along line 2, the induced current shape is bipolar, since the weighting field direction changes along the path.

$$Q(t) = -q\phi_0(x(t)). \tag{3.18}$$

Figure 3.12 is reproduced from [Rad88] and shows the numerically calculated weighting field in a strip detector of planar geometry. Two examples of charge transit are shown along with the resulting induced current pulses.

3.3.4 The Preamplifier

In order to extract the signal generated by a gamma-ray interaction an interface between the detector and processing chain is required. In the case of Germanium detectors this usually takes the form of a charge sensitive preamplifier (Figure 3.13) which integrates the induced current resulting in a charge pulse with magnitude proportional to the energy deposited by

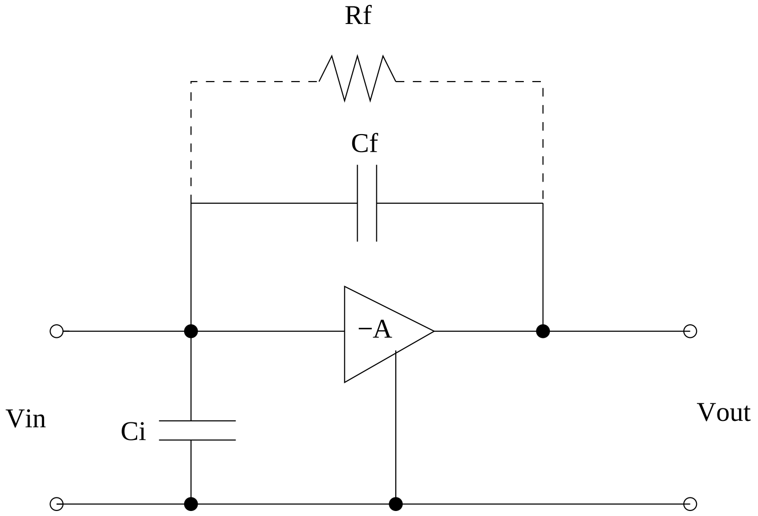

Figure 3.13: Circuit diagram of a typical charge sensitive preamplifier.

the gamma-ray. Any good preamplifier must have good signal to noise properties and it is for this reason that they are usually located as close to the detector as possible in order to minimise capacitative loading [Kno99]. In Germanium detectors a Field Effect Transistor (FET) input stage is included which provides an initial amplification while maintaining a large signal to noise ratio.

Charge sensitive preamplifiers operate in such a way so as to ensure that the output voltage, Vout, is proportional to the total integrated charge in the pulse provided to the input terminals. For a typical charge sensitive preamplifier, values of feedback resistance (Rf) and feedback capacitance (Cf) may be $\sim$1GΩ and 1pF respectively.

3.3.5 Pulse Shape Analysis Techniques

The development of germanium detector technology over the past ten years has, in addition to improved energy resolution and durability already discussed, resulted in the production of position sensitive detectors through electrical segmentation of the contacts. This segmentation, commonly achieved today through the use of lithographic techniques, provides increased granularity while maintaining full detection efficiency. By reading out each of the electrodes on a detector, the position of a gamma-ray interaction may be localised to within that voxel or segment.

Composite germanium detectors [Duc99] have been used successfully at international facilities around the world for a number of years providing the increased position sensitivity required for improved Doppler correction [But87], [Nol85] and Compton polarimetry [But73], [Sim83]. While these type of detectors typically provide position resolution of the order of several cubic mm, finer granularity is required if the goal of a 4π gamma-tracking array [Sim05] is to be realised and germanium detectors are to compete with scintillation detectors in the field of medical imaging.

In order to improve the spatial resolution achievable with a germanium detector beyond this raw segmentation, Pulse Shape Analysis (PSA) techniques must be employed. These techniques study the waveform response of the preamplifier and extract precise three dimensional position information on an event by event basis. In general, these techniques have two distinct components, one which yields the interaction position between the AC and DC coupled contacts (interaction depth in a planar) and a second which can be used to determine the interaction position relative to a segment boundary. In a coaxial detector this position is the azimuthal angle between the core and a given boundary while in the case of the simple planar geometry it is the lateral interaction position in both the x and y planes.

The first of these components requires analysis of the real charge pulse produced according to the Schokley-Ramo theorem previously discussed. If one makes the assumption that the bias voltage applied to the detector is sufficient as to ensure the drift velocity of free electrons and holes is saturated then the time taken for these charge carriers to drift to their collecting electrodes can only be a function of the distance they must travel. Therefore, the charge collection time - represented by the risetime of the charge pulse - is indicative of the gamma-ray interaction position. The second stage in determining the three-dimensional interaction position requires analysis of the transient charges (often referred to as image charges or mirror charges) induced in neighbouring strips by the movement of charge carriers in the interaction strip. These signals have no net charge and are produced as a consequence of the electrostatic coupling between moving charge carriers and the electrodes. In a planar germanium detector the relative magnitude (and area) of the transient charges on the strips either side of a collecting electrode varies with the proximity of the interaction. That is, the closer to a given neighbour strip the interaction takes place, the larger the image charge will be. As a result, the position sensitivity in the lateral plane can be calibrated using the image charge asymmetry parameter, A_{ic} defined by Equation 3.19, where Q_L and Q_R are the image charge areas in the strips to the left and right of a collecting strip respectively.

$$A_{ic} = \frac{Q_L - Q_R}{Q_L + Q_R} \tag{3.19}$$

Using pulse timing and image charge analysis techniques has been shown to provide sub-mm spatial resolution in a planar HPGe detector when applied to mean pulse shapes resulting from single pixel interactions [Mil05]. The application of event by event PSA techniques is presented in greater detail in later chapters.

Chapter 4

The SmartPET System

The SmartPET (Small Animal Reconstruction Tomograph for Positron Emission Tomography) is an imaging system based on the use of two planar Double Sided Germanium Strip Detectors (DSGeSDs) referred to as SmartPET1 and SmartPET2. To facilitate PET imaging these detectors are mounted in a rotating gantry in a Dual Head PET Camera configuration. This frame allows data acquisition over a full 180° range for image reconstruction.

4.1 The SmartPET Detectors

Each ORTEC manufactured SmartPET detector contains a 74×74×20mm High Purity Germanium crystal (a schematic diagram is displayed in Figure 4.1) which includes a 7mm wide guard ring (designed to maintain electric field uniformity towards the edge of the crystal) and a 1mm thick aluminium entrance window. The active region of each detector has dimensions 60×60×20mm with 12×12 orthogonally segmented outer contacts. The HPGe crystals have an impurity concentration of $\sim 6{\times}10^{9}\mathrm{cm}^{-3}$ where the maximum variation through the depth of the crystals is less than 5% [San05]. As discussed in Chapter 4, section 3.2, the charge carrier drift velocity is maximum along the <100> direction and as a result the SmartPET crystals were cut in such a way as to ensure that the depth profile is parallel to this axis (to within 1° uncertainty) thus maximising charge collection efficiency. According to the manufacturer's specifications both SmartPET detectors are fully depleted at -1300V and have a recommended operating voltage of -1800V.

Both faces on each detector are thought to have implanted contacts although specific information on their nature has not been made available by the manufacturer. The AC coupled (p^+) contacts are $\approx 0.3\mu$m thick separated by 180μm while the DC (n^+) contacts are segmented into 50μm deep strips with 300μm separation. The strip pitch on each contact is 5mm, produced by lithographic techniques.

All 24 strips on each SmartPET detector are furnished with ORTEC designed fast charge sensitive preamplifiers with a warm FET configuration and a gain of 300mV/MeV. These low noise, high bandwidth preamplifiers, believed to be based on the Heidelberg-Cologne design [Ebe01], have a decay time constant of approximately 54μs (calculated by performing an exponential fit to the decay of the charge pulse) and according to [Tur06] a rise time of 30ns[1].

A picture of one of the SmartPET detectors is shown in Figure 4.2 along with a schematic diagram of the crystal geometry in Figure 4.1, and the exposed charge sensitive preamplifiers in Figure 4.3.

4.1.1 Energy Resolution

The energy resolution of the SmartPET detectors is typically around 1.5keV FWHM at 122keV and less than 3.0keV FWHM at 1332keV. In PET measurements, the 511keV gamma rays produced following positron-electron annihilation are subject to Doppler broadening due to the positron momentum upon annihilation, resulting in a typical energy resolution of around 3.0-3.5keV FWHM. The variation in energy resolution as a function of energy for a typical AC strip is shown in Figure 4.4 while the energy resolution at 511keV for each strip of the two detectors can be found in Appendix A.

In Figure 4.4 one can observe how the energy resolution is consistently worse for data recorded through digital electronics than analogue electronics. This is due to incomplete use of the dynamic range of the digital electronics resulting in greater spread of calculated energies. Further details of the digital electronics employed by the SmartPET system are presented in subsequent sections. Energy spectra from the twelve AC channels of SmartPET1 recorded through these digital electronics in the presence of a ^{22}Na point source

---

[1] The rise time is a measure of system response and is conventionally defined as the time difference between 10% and 90% of the maximum of the charge pulse.

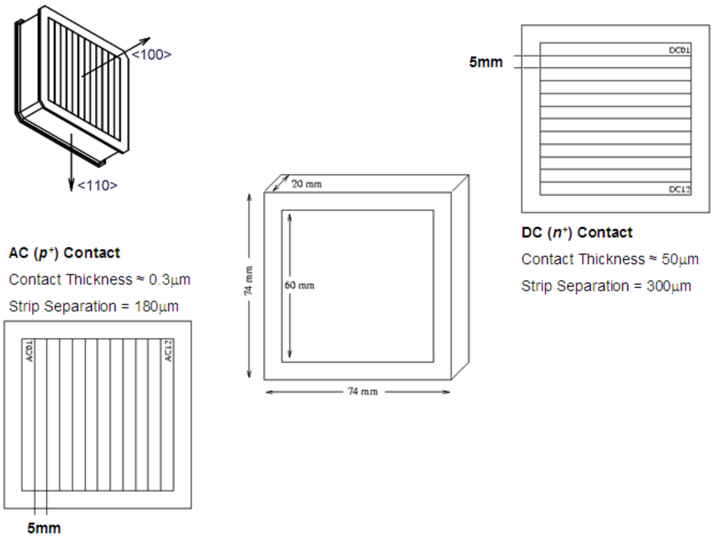

Figure 4.1: A schematic representation of one of the SmartPET HPGe crystals, cut with the depth profile parallel to the <100> axis. Each crystal has an active area of 60×60×20 mm surrounded by a 7mm guard ring. The AC coupled (p^+) contacts are ≈ 0.3μm thick separated by 180μm while the DC (n^+) contacts are segmented into 50μm deep strips with 300μm separation.

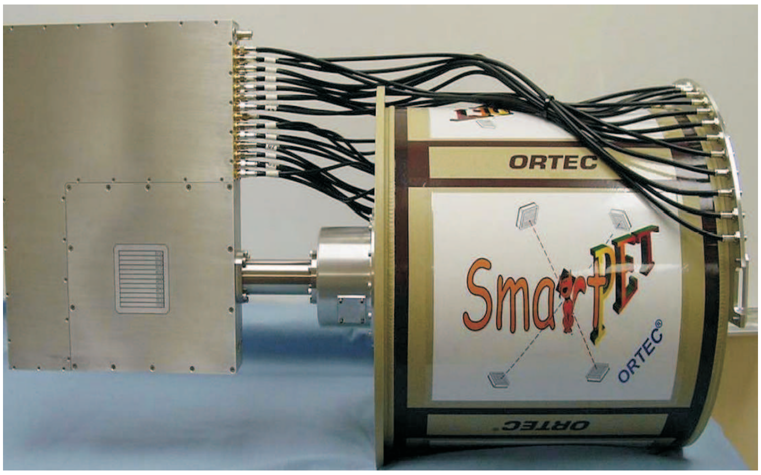

Figure 4.2: A picture of one of the SmartPET planar HPGe detectors.

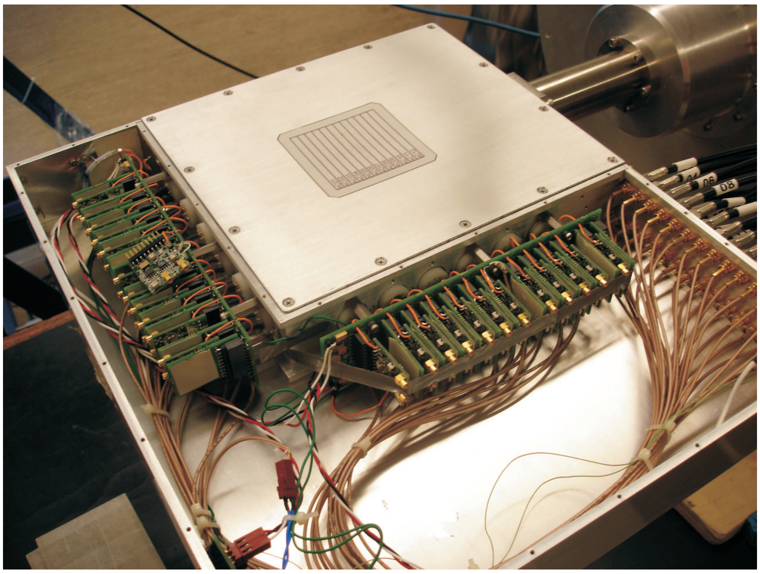

Figure 4.3: One of the SmartPET detectors with the housing removed to expose the charge sensitive preamplifiers. The circuit boards contain the preamplifiers with warm FET input stage, with one bank reading out the AC channels and one the DC.

are shown in Figure 4.5. These spectra show the 511keV annihilation photopeak and the 1275keV peak characteristic of ^{22}Na decay. These spectra exhibit a uniform response across the twelve strips.

4.1.2 Efficiency

The absolute efficiency of a gamma-ray detector, ϵ_{abs}, may be calculated as a function of gamma-ray energy according to Equation 4.2 where the count rate is given by

$$Count\ rate = \frac{Net\ area\ of\ photopeak}{Count\ time}. \tag{4.1}$$

If P_γ is the branching ratio corresponding to the gamma-ray of interest, The absolute efficiency can then be defined as

$$\epsilon_{abs} = \frac{Count\ rate}{Source\ Activity \times P_\gamma}. \tag{4.2}$$

In order to calibrate the absolute efficiency of the SmartPET1 detector a measurement was performed using a range of point sources (^{152}Eu, ^{133}Ba, ^{241}Am and ^{60}Co) positioned 25cm above the AC coupled face of the detector. From Equations 4.1 and 4.2 the absolute

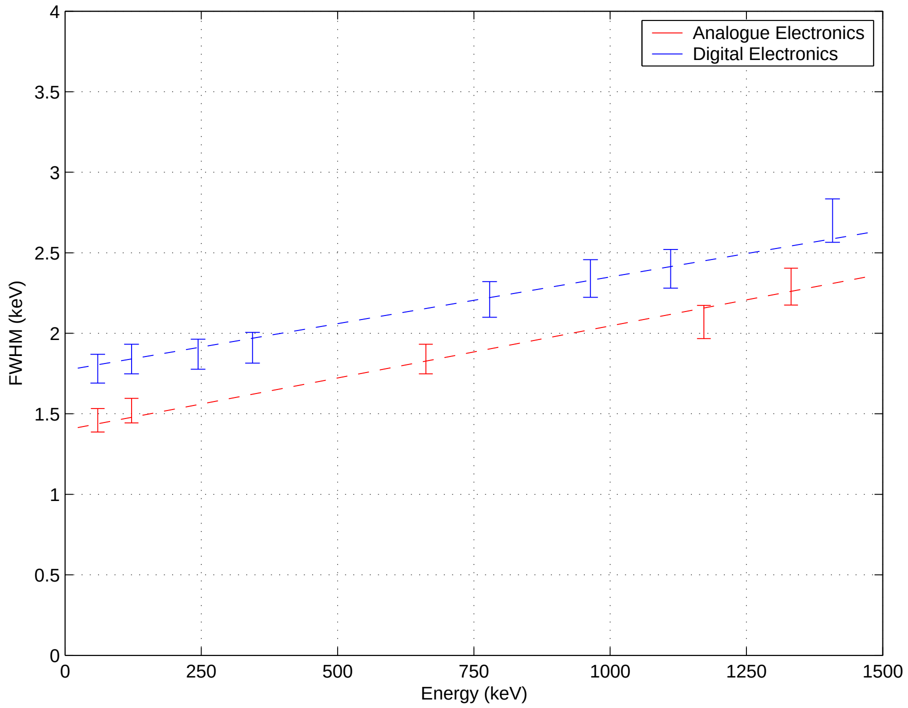

Figure 4.4: Energy resolution as a function of energy for a typical AC strip of the SmartPET1 detector. The plot shows values recorded through both analogue and digital electronics.

efficiency of the AC face of detector was calculated as a function of energy. This result is displayed in Figure 4.6 and shows how the absolute efficiency reaches a maximum of ∼0.3% for gamma-rays of around 80keV. The figure shows the efficiency resulting from fold one interactions (fold$_{AC}$ = 1) and the total efficiency when the detector is operated in 'Add-Back mode'. The fold of an event is defined as the number of strips recording real charge. In order to assign fold to an event the pulse shape digitised from each strip is analysed in order to distinguish between signals containing net charge, image charge and noise. The noise level of each pulse shape is calculated as the standard deviation, σ, of the baseline over the first 25% of the trace. If the difference in amplitude between the start and end of the pulse is found to be $\geq 3\sigma$ the signal is considered to be a real charge pulse and the fold incremented by one. As the Root Mean Square (RMS) noise value is approximately 5mV (the peak to peak noise typically being around 7mV), this technique allows identification of real charge pulses above around 10keV. In this work the fold of the AC and DC faces are defined seperately as fold$_{AC}$ and fold$_{DC}$. The orthogonal strip configuration of the

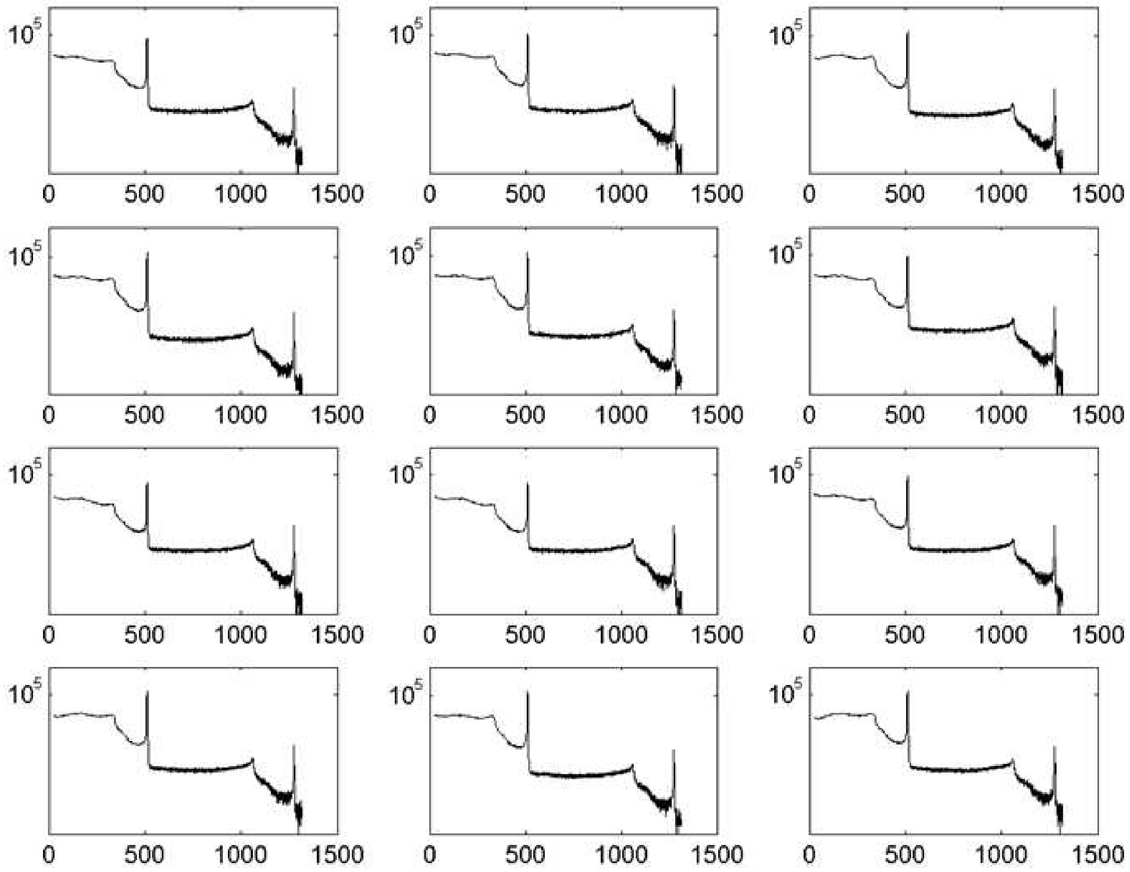

Figure 4.5: Experimental ^{22}Na gamma-ray spectra from the twelve AC channels of the SmartPET1 detector. The spectra show the 511kev annihilation photopeak and the higher energy (1275keV) peak characteristic of ^{22}Na decay. The x-axis denotes energy in keV while the y-axis displays the number of counts on a logarithmic scale.

SmartPET detectors allows pixels to be defined in terms of AC and DC strips. An event with $\text{fold}_{AC} = \text{fold}_{DC} = 1$ may therefore be referred to as a single pixel hit. In Add-Back mode the energy of the initial gamma ray may be recovered through the correlation of events which scatter between strips. By summing the partial energies the photopeak intensity may be maintained. When implementing the Add-Back procedure, a correction must be applied which accounts for cross-talk between strips, an effect which would otherwise result in the calculation of an incorrect energy. A comprehensive discussion of the Add-Back procedure and cross-talk correction methodology applied to the SmartPET detectors is provided in Appendix B. From Figure 4.6 it can be seen how the absolute efficiency of the detector is

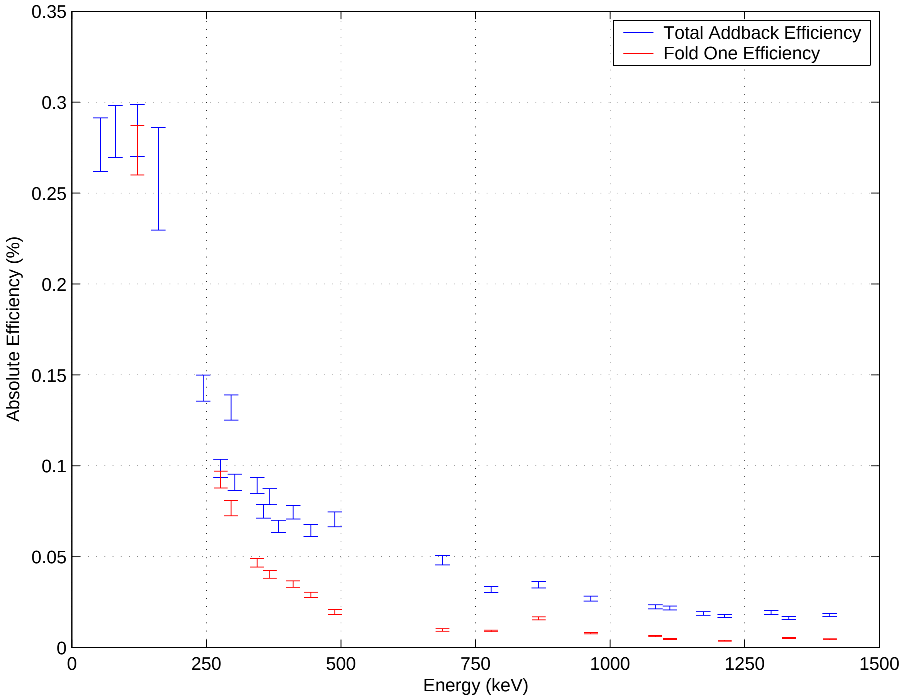

Figure 4.6: Absolute efficiency of the SmartPET1 detector as a function of gamma-ray energy.

0.071(0.004)% for 511keV gamma rays.

4.1.3 Intrinsic Efficiency

Of greater relevance to the discussion of detector performance is the concept of intrinsic efficiency. This metric takes account of the solid angle between the source and detector, allowing for the fact that only a small fraction of emitted gamma rays are incident on the detector. Modelling the surface of the SmartPET1 detector as a circle of radius 30mm, it is calculated that at a source-detector distance of 25cm, the detector surface covers only 0.36% of the total 4π solid angle over which the isotropic point sources emit gamma rays. By correcting for this factor, the intrinsic efficiency of the SmartPET1 detector is found to be around 19% at 511keV.

4.1.4 Peak to Total Ratio

The peak to total (P:T) ratio (also known as the photofraction) of the SmartPET1 detector was measured for 662keV gamma rays. The value was calculated as the ratio of the number of events in the photopeak to the total number of counts in the photopeak and Compton continuum. Values were calculated from Add-Back spectra for a range of (AC) fold scenarios and from a total Add-Back spectrum. Table 4.1 summarises these values showing how the P:T ratio improves as the fold of the event increases. The photofraction of a detector is an important consideration for clinical PET [Man02] where the significant scatter fraction presented by human subjects makes photopeak gating essential [Tow04]. In pre-clinical PET imaging the photofraction is less significant as the scatter fraction is much lower for small animal subjects.

AC Fold	Peak to Total Ratio (%)
1	2.88(0.03)
2	23.47(0.05)
3	46.97(0.16)
All Folds	22.96(0.04)

Table 4.1: Peak to total ratio for the SmartPET1 detector for a range of event folds. The Peak to Total ratio calculated from the total Add-Back spectrum for the AC face is 22.96(0.04)%.

4.1.5 Timing Resolution

The timing resolution of the SmartPET1 detector was measured relative to a Sodium Iodide (NaI(Tl)) detector using a ^{22}Na point source positioned between the two detectors with gamma rays incident on the AC face of the SmartPET detector. The preamplifier response of strip AC06 on SmartPET1 was processed by an ORTEC 474 TFA, set to 20ns integration and 100ns differentiation, followed by an ORTEC 473A CFD configured with 20ns constant fraction delay. The CFD threshold was set to just below 511keV. The output of the NaI detector was processed using a single channel of an ORTEC 863 Quad TFA (50ns integration and 100ns integration) followed by a LeCroy 623B Octal Discriminator with the threshold again set just below 511keV. The output of the NaI (discriminator) and Ge (CFD), once delayed by 200ns, then formed the respective ‘start’ and ‘stop’ signals to an ORTEC 566 Time to Amplitude Converter (TAC), the output of which was histogrammed using the ORTEC Maestro software [MAE]. The resultant time spectrum, recorded through analogue electronics showed a prompt coincidence peak with FWHM of 11.67(0.64)ns. This spectrum is displayed in Figure 4.7(right) along with a time spectrum of the NaI detector relative to another NaI (left). The prompt coincidence peak in the spectrum on the left was calculated to have a FWHM of 4.14(0.16)ns. The structure to the right of the prompt coincidence peak in Figure 4.7(right) results from the late arrival of 'stop' signals from the SmartPET detector relative to the 'start' signals from the NaI. This is believed to be an effect caused by the strong variation in pulse shapes originating from the SmartPET detector which in turn is a result of the charge collection process and high bandwidth ($\sim$12.5MHz) of the preamplifiers. The variation in pulse shape response as a function of interaction position is discussed in Chapter 5 where the distribution of charge pulse rise times appears consistent with the extent of the tailing observed in Figure 4.7(right).

The coincidence timing resolution of a PET system is important for the rejection of random coincident events. Based on the time spectrum presented in Figure 4.7(right) it is reasonable to assume that the coincidence window between the two SmartPET detectors, when operated in PET mode, may be set to around 10ns (based on the time window of each detector being set to one standard deviation of the prompt coincidence distribution). This value is unlikely to be optimal as the time resolution of Ge detectors with analogue electronics may be as good as 5ns for a coaxial HPGe detector or 1ns for a thin Ge(Li) planar detector [Poe97]. Digital CFD algorithms for HPGe detectors [Gas00] are designed to be insensitive to variations in the shape and amplitude of the charge pulse thus providing a robust trigger and optimum timing performance. By using these techniques the tailing observed in Figure 4.7(right) may be eliminated [Mih07] thus improving the timing resolution while maintaining the prompt coincidence efficiency. As discussed subsequently in Section 4.3, ongoing developments of the SmartPET system include the commissioning of digital electronics incorporating such an algorithm.

4.1.6 PET Sensitivity

The absolute sensitivity of a PET system may defined in a number of ways. In [Lar06] several commercially available small animal imaging systems are reviewed, with the absolute sensitivity defined in terms of the absolute efficiency for coincident detection of 511keV gamma-rays emitted from an isotropic source placed at the centre of the field of view

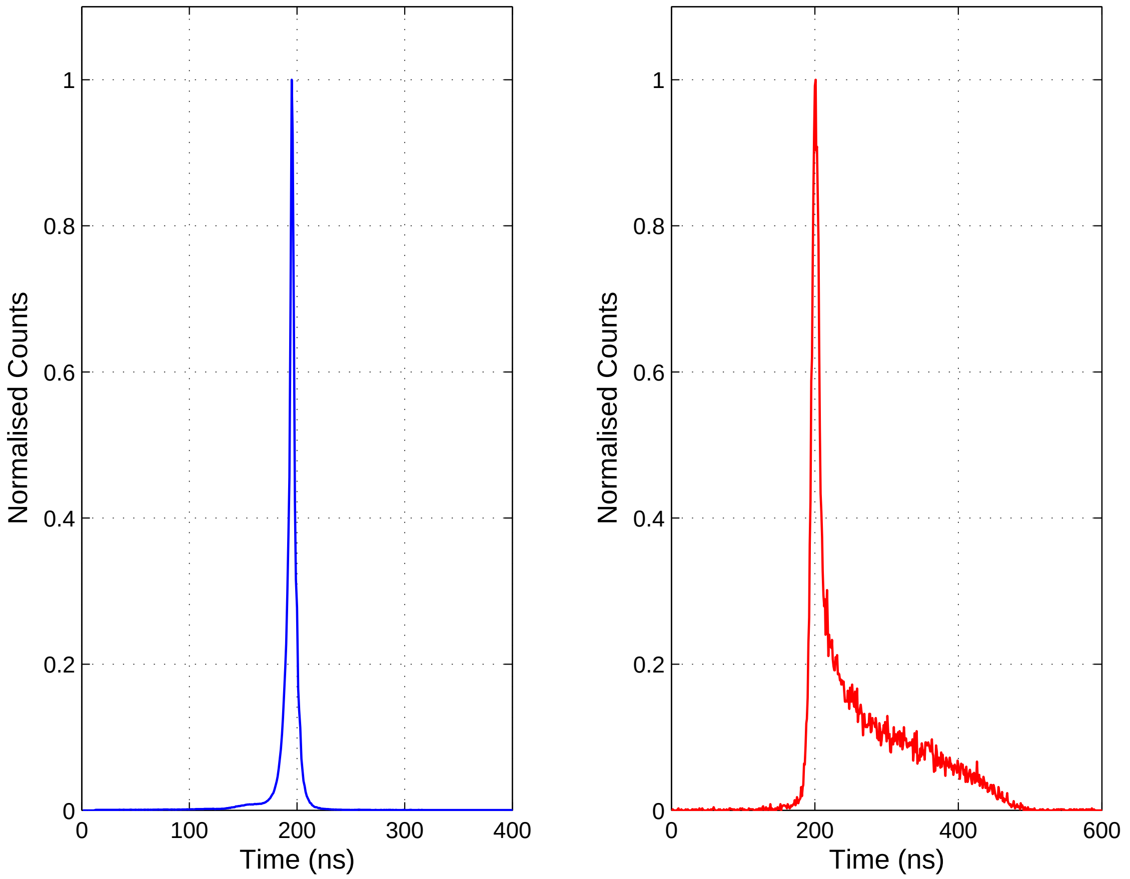

Figure 4.7: Left: The time spectrum recorded between two NaI detectors showing a prompt coincidence peak with FWHM 4.14(0.16)ns. Right: The time spectrum recorded between the SmartPET1 detector and a NaI detector. The prompt coincidence peak of this spectrum has a FWHM of 11.67(0.64)ns. The structure to the right of the prompt coincidence peak results from the late arrival of discriminator signals from the SmartPET detector relative to those from the NaI detector. This is believed to be due to the large variation in pulse shapes from the SmartPET detector.

(FOV). There is however no requirement for full energy deposition to occur (as is the case for the absolute efficiency values calculated previously).

In order to determine the PET sensitivity of the SmartPET system a 0.0307MBq ^{22}Na source was placed at the centre of the FOV with the SmartPET detectors separated by 130mm (65mm source-detector separation).

During data acquisition a trigger request rate of 400 coincidences per second was recorded. Due to limitations in the electronics data transfer capacity the accepted trigger rate was

Event Type	Sensitivity (%)
Absolute Sensitivity	0.992
Single Pixel Events	0.122
Single Pixel Photopeak Events	0.001

Table 4.2: Summary of the PET sensitivity of the SmartPET system in a number of event scenarios. The absolute PET sensitivity for a source at the centre of the field of view is found to be ∼1%.

220cps. By vetoing events depositing more than 520keV in either detector (a cut was applied above the 511keV photopeak) the average count rate from coincident 511keV gamma-rays depositing some energy in both SmartPET detectors was found to be 176cps. A dead time correction was applied where the correction factor, τ, for a nonparalysable system is described in terms of the trigger request rate, n, and accepted trigger rate, m, by [Kno99] as

$$n = \frac{m}{1 - m\tau}. \tag{4.3}$$

Application of this correction factor results in a coincident count rate from 511keV gamma-rays of 276cps. The system sensitivity was then calculated as the ratio of events recorded to source activity, factoring in the 90.5% branching ratio for β^+ decay from ^{22}Na. This calculation yields an absolute PET sensitivity of 0.99%. Similar calculations were performed for events where energy was deposited in only a single pixel in each detector and for events where full energy deposition occured within a single pixel in each detector (single pixel photopeak events). The absolute sensitivity of the SmartPET system for each of these scenarios is summarised in Table 4.2.

A comparison of the performance of the SmartPET system relative to commercially available small animal PET imagers will be provided in later stages of this work. However, the efficiency and sensitivity results presented here suggest that 20mm of germanium is insufficient for stopping 511keV gamma rays. This is unlikely to pose a problem for small animal imaging as the low scatter fraction reduces the need for photopeak gating. In a high scatter scenario, such as clinical imaging for example, this is no longer the case and the use of only photopeak events for imaging becomes essential.

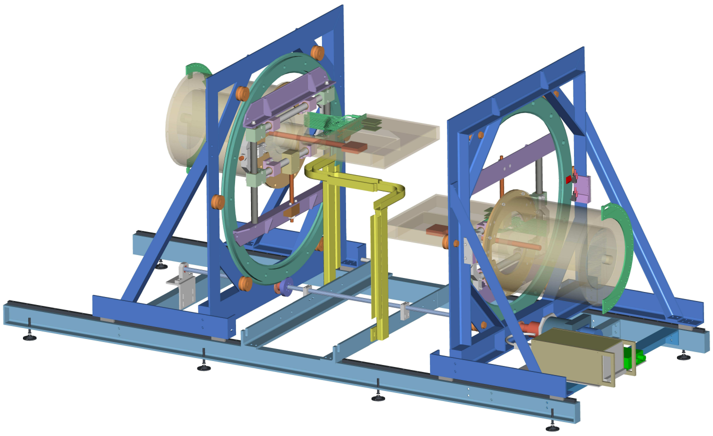

Figure 4.8: Three dimensional CAD model of the SmartPET detectors in the rotating gantry.

4.2 The Rotating Gantry

In a dual head PET camera, the imaging detectors must be rotated around a stationary subject. For the SmartPET system, a specially designed gantry provides both a secure holding structure and precision rotation mechanism for the HPGe detectors. The software controlled rotation is delivered through a Mclennan stepper motor with 400 step per revolution resolution. The gantry control software allows the user to select the range of rotation, angular step size and dwell time at each position while ensuring inhibition of data transfer during movement. In its current configuration the step size is set to 1°. A low rotation speed is maintained in order to minimise the induction of microphonic noise through the movement of liquid nitrogen within the dewars. A 3D CAD model of the SmartPET detectors in the rotating gantry is displayed in Figure 4.8.

4.3 Digital Electronics

The SmartPET system uses digital pulse shape analysis techniques to extract time, position and energy information from the charge pulse response of the detectors following a gamma-ray interaction. It is therefore necessary to digitally record these waveforms on an event by event basis. Throughout its development, the SmartPET has utilised the STFC (formerly

CCLRC) Daresbury designed GRT4 VME cards [Laz03] to digitise the detector response. The VME based design of the GRT4 system places a fundamental upper limit on the rate of data transfer which can be achieved (4Mb/s) while the nature and capacity of the Field Programmable Gate Array (FPGA) infrastructure limits the implementation of online pulse processing algorithms. As a result, the final SmartPET prototype will use a commercial Compact PCI based electronics solution provided by Lyrtech. This system uses the Total Data Readout (TDR) [Pag03] [Col05] technique in order that each channel be free running with the absence of an external hardware trigger (as with the GRT4 system). This requires the definition of an 'event' in software and allows, for example, the coincidence time window to be varied. Crucially, the system also employs user programmable[2] dual level FPGA and Digital Signal Processor (DSP) processing. This provides an environment for the development and implementation of pulse shape analysis and image reconstruction algorithms, the ultimate objective being fully online data analysis.

4.3.1 The GRT4 VME Cards

The Gamma Ray Tracking 4-Channel (GRT4) VME Module is designed to perform the digital pulse processing required for gamma-ray tracking [Sim05]. Each VME module contains four input channels each operating in parallel. These channels digitise the preamplifier signal from a HPGe detector using a 14bit 80MHz flash ADC. Two dedicated Xilinx Spartan 2 FPGAs, each with 200k gates available, provide data processing and buffering for each channel. A programmable pretrigger delay and digital trigger is included in the first FPGA while the second provides a calculation of energy through a Moving Window Deconvolution (MWD) [Geo94] algorithm. A 40MHz low pass filter is applied to the input prior to digitisation and an optional differentiation stage is also provided.

Routinely, the GRT4 cards are operated with an external trigger input provided by a NIM logic pulse. Each card requires one trigger signal which is distributed to all four channels while an inhibit signal synchronises multiple modules prohibiting acceptance of events during readout of pulse traces.

---

[2] The FPGAs may be programmed using the Handel-C based development environment from Celoxica [CEL]. Algorithms, developed using a language based on C are then converted into VHDL and downloaded directly to the FPGA via ethernet connection.

Chapter 5

Detector Performance

In order to fully understand the performance of a HPGe detector and develop PSA techniques, the response of the detector as a function of gamma-ray interaction position must be quantified. This is achieved by performing high precision scans of the crystals using finely collimated gamma-ray beams at a range of energies. This technique is known as detector characterisation [Des02] and in addition to facilitating PSA allows the uniformity of response of the detector to be investigated, and the charge collection performance to be assessed. This section discusses details of the characterisation procedure employed for the first SmartPET detector and presents results from subsequent analysis of the scan data.

5.1 Scanning System

The scanning system utilises a high precision Parker Automation positioning table [Des02] which allows a collimated beam of gamma rays to move independently in both the x and y axes. This positioning table is driven by Pacific Scientific stepper motors which are operated by software controlled indexers. For the scan results presented within this work, the system was configured with 100μm resolution.

The results from two complementary characterisation measurements performed on the SmartPET1 detector are presented here:

- A surface scan performed with a collimated 1GBq ^{241}Am source. The low energy of the characteristic ^{241}Am gamma ray (59.4keV) provides a means of investigating the uniformity of response across the surface of the detector. Results from this measurement are presented in Section 5.2.

- A scan of the depth profile (side scan) of the detector using a collimated 1850MBq ^{57}Co source to provide a calibration of the depth of interaction sensitivity of the detector. The 122keV ^{57}Co gamma ray maximises the photoelectric absorption cross section while still being of sufficiently high energy to ensure penetration of the aluminium housing the HPGe crystal. This measurement is discussed in detail in Section 5.3.

The scanning system is represented schematically in Figure 5.1 while Figure 5.2 shows a photograph of the SmartPET1 detector during the ^{241}Am surface scan. In order to perform a sidescan the detector must be rotated through 90°. The distance between the top of the collimator and the aluminium entrance window was 3mm for the ^{241}Am surface scan performed. The physical distance from the injection beam to the HPGe crystal was therefore 1.8cm. For the ^{57}Co sidescan, the top of the collimator was positioned 2mm away from the aluminium can housing the HPGe crystal. The crystal is separated from the can by 64mm in this dimension, the total distance from the top of the collimator to the HPGe crystal was therefore 66mm.

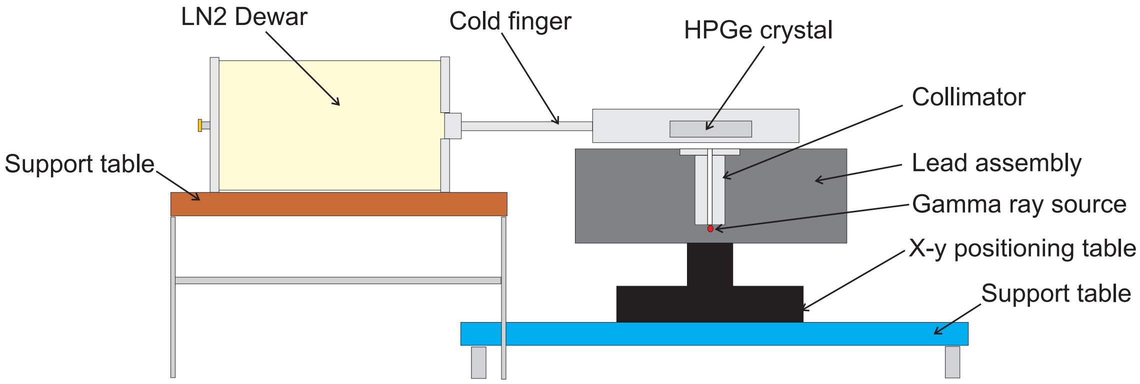

Figure 5.1: Diagram of the SmartPET1 detector on the scanning table in surface scan configuration. A gamma-ray source housed within a lead assembly is collimated through a tungsten collimator.

To produce the fine gamma-ray beam required for characterisation, a source, housed within a lead assembly, is collimated through a 80mm long x 1 mm diameter tungsten collimator. The lead shield surrounding the collimator is designed to minimise the count

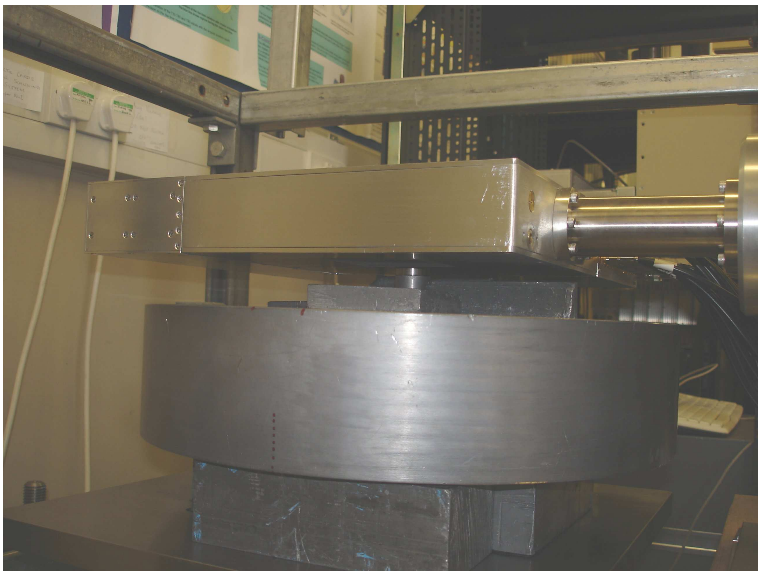

Figure 5.2: SmartPET1 on the scanning table during a surface scan. The finely collimated gamma-ray beam housed within the lead assembly is raster scanned across the surface of the detector in order to investigate the detector response as a function of position.

rate outside the area defined by the collimated beam. Simulations have been performed in MCNP [MCN], a multi purpose Monte Carlo code, to investigate the effectiveness of this design and quantify the beam divergence. The flux of gamma rays from a ^{137}Cs source (E_γ=662keV) was calculated as a function of lateral distance from the collimator. Figure 5.3 shows how the beam profile falls away significantly as distance from the collimator hole increases. The FWHM of the beam is found to be $\sim$ 1.6mm at a source-detector distance of 1.5cm. This simulation was performed with a ^{137}Cs source as at 662keV, gamma rays penetrating the collimator walls may reasonably be expected to contribute to increasing the beam divergence. Thus, one may be confident that at lower energies the FWHM of the beam profile will not exceed the value quoted above.

5.1.1 Trigger Electronics and Data Acquisition System

In order to process the 24 strip signals in addition to the guard ring signal, 7 GRT4 modules were required for the front face and side scans. The GRT4 cards were provided with an external NIM logic trigger through the fast timing circuit presented in Figure 5.4. The

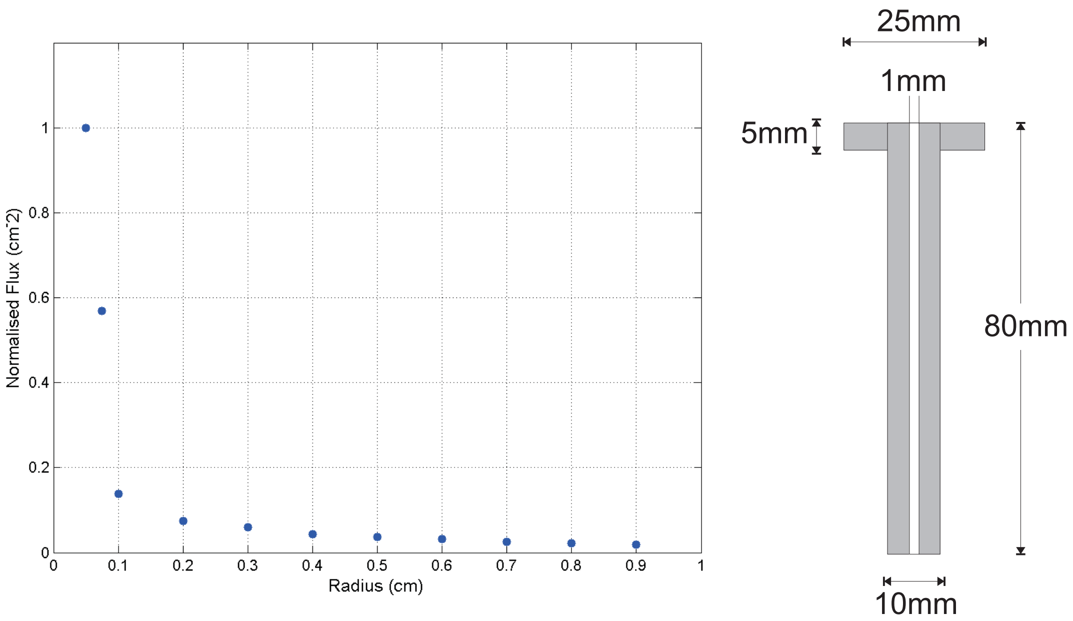

Figure 5.3: Dimensions of the tungsten collimator forming part of the scanning system alongside the results of a Monte Carlo simulation which shows how the flux of 662keV gamma-rays falls away as a function of radial distance from the collimator. The FWHM of the beam is found to be ~1.6mm at a source-detector distance of 1.5cm.

output from each of the twelve AC coupled strips was split into two branches where the first branch was connected directly to the input of the GRT4 cards whilst the second branch formed the input to the triggering chain. Each of the twelve AC signals were processed by Ortec 863 Quad Timing Filter Amplifiers (TFAs), operated with maximum differentiation and minimum integration, followed by Ortec 935 Quad Constant Fraction Discriminators (CFDs). The CFDs were configured with 20ns constant fraction delay and a threshold such that the units would be triggered by a pulse of around 30keV. The twelve fast trigger lines from the CFDs were then connected to a Phillips Scientific 785 Quad Logic Unit which provided the primary trigger in the form of a logical OR of the inputs. This primary trigger formed the input to a Phillips Scientific 794 Quad Gate and Delay (G&D) generator, the output of which being the master trigger. The master trigger was duplicated with a logic Fan In/Fan Out module in order to provide the global trigger required by the GRT4 cards. Following the receipt of a valid trigger signal data were read out sequentially. The data collection was inhibited during data read out by utilising the busy signal from the GRT4

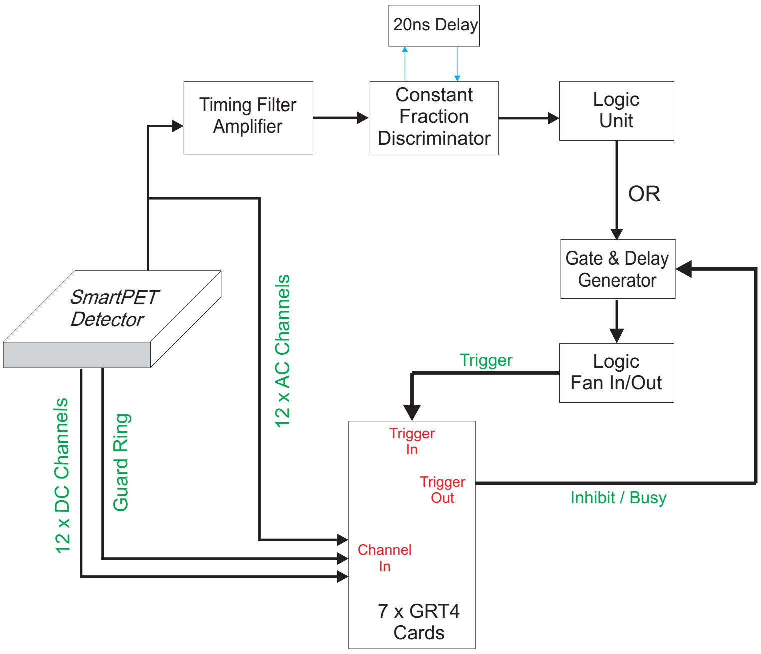

Figure 5.4: Circuit diagram of the analogue electronics used to trigger the data acquisition system during scanning of the SmartPET1 detector.

cards.

5.2 ^{241}Am Surface Scan

The SmartPET1 detector was scanned using a 1GBq annular ^{241}Am source through a 80mm long x 1mm diameter tungsten collimator. The objective of this measurement was to use the low energy characteristic ^{241}Am gamma ray (59.4keV) to investigate the uniformity of response across the surface of the detector. The collimated beam of gamma rays was raster scanned across the surface of the crystal in 1mm steps. Data were recorded for 3 minutes per position with an average count rate of around 15cps. This procedure was repeated with the gamma rays incident on both the AC and DC coupled faces of the SmartPET detector.

A photopeak gate of around 5keV was applied to data from the AC surface scan and an intensity plot displaying the number of full energy gamma-ray events as a function of collimator position for the scan of the AC face is shown in Figure 5.5(left) where the x and y axes show the collimator position in mm. In constructing the matrix in Figure 5.5(left) the photopeak gate was applied to spectra of the sum of energies deposited (individual spectra were incremented for the AC and DC coupled faces). These spectra were only incremented if a strip was identified as containing real charge according to the procedure discussed in Section 4.1.2.

This result shows a relatively uniform response across the surface of the crystal with the exception of the first DC strip where the presence of wire bonded contacts for the AC face reduces the number of gamma rays interacting in the active volume of the crystal. While this effect reduces the low energy efficiency of this strip the attenuating material has a negligible effect for gamma rays with energy above a few hundred keV. The same feature may be observed in the corresponding intensity plot from the DC surface scan presented in Figure 5.6(left) where this time the bonded contacts for the DC coupled strips result in discrete regions of reduced intensity.

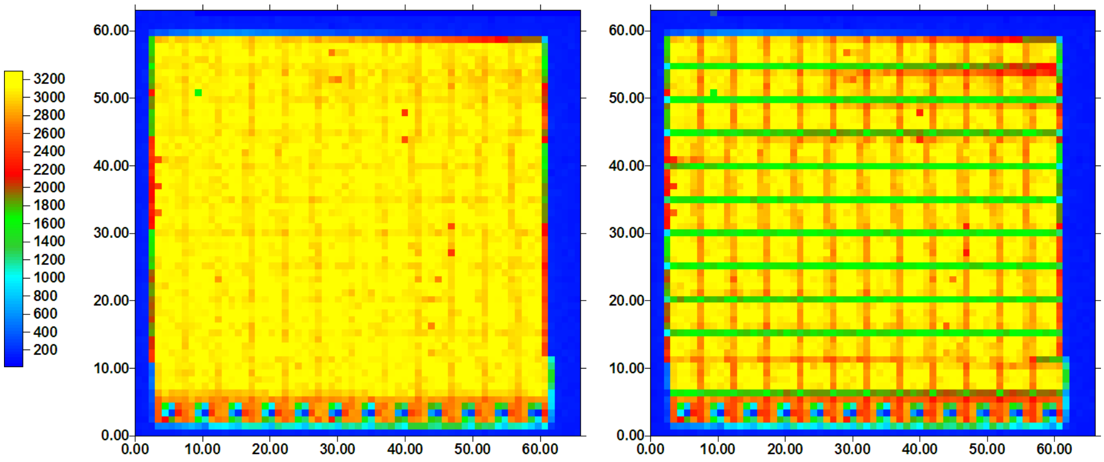

Figure 5.5: Response matrices from a high precision ^{241}Am scan of the AC surface of the SmartPET 1 detector. Left: The number of full energy (sum energy) interactions as a function of collimator position. Right: The number of full energy single pixel hits as a function of collimator position. In both images the x and y axes show the position of the collimator in mm.

Comparing the response matrices for the AC and DC surface scans a number of features may be observed. From Figure 5.6(left) a reduction in the number of counts recorded in two AC coupled strips can be seen. This is a result of too high a CFD threshold being applied in the trigger electronics associated with these strips and leads to a 15-20% drop in counts. One also observes a reduction in counts, of similar magnitude, when the collimator is positioned over AC strip gaps. As the matrix was produced by gating on the total energy

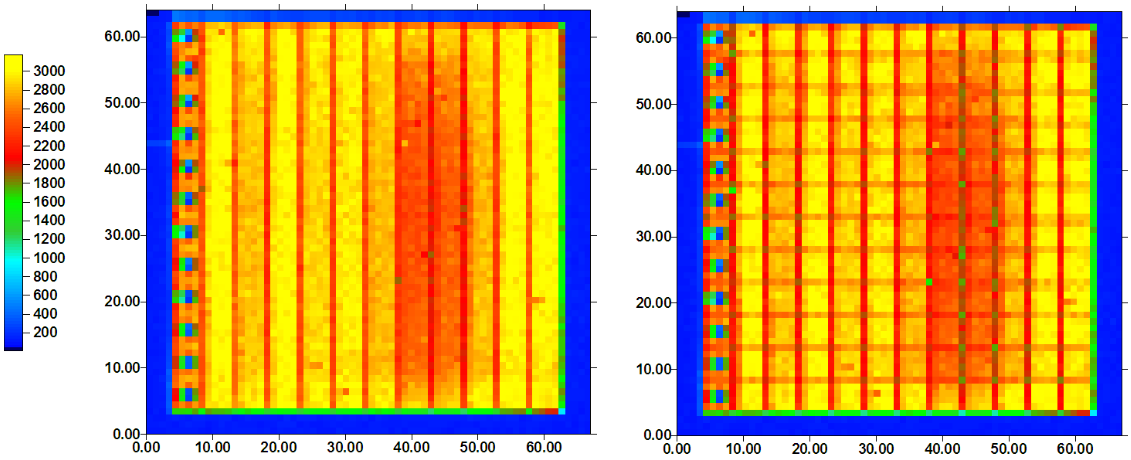

Figure 5.6: Response matrices from a high precision ^{241}Am scan of the DC surface of the SmartPET 1 detector. Left: The number of full energy interactions as a function of collimator position. Right: The number of full energy single pixel hits as a function of collimator position. In both images the x and y axes show the position of the collimator in mm.

deposited in the detector, this suggests that for these events some charge is being lost, resulting in a reduced number of photopeak counts. A similar effect has been previously observed in HPGe strip detectors [Cob03] due to the splitting of the charge cloud between adjacent electrodes. Incomplete charge collection occurs due to weak lateral electric field regions between these adjacent electrodes. In some cases a small amount of charge may be lost to the gap or collected to the surface between two electrodes, resulting in the event falling outside the photopeak. It is also possible that rather than charge being physically lost, the amount of charge being collected by a given electrode may simply be below the low energy threshold, typically around 10keV, used to identify real charge. When the DC face of the detector is scanned with higher energy gamma rays the charge loss effect is no longer observed [Bos07] suggesting that this may in fact be the case. In the scan data presented here, the influence of these events on detector performance is relatively small with no significant tailing being observed in ^{241}Am photopeaks.

In order to further investigate the contact structure an additional requirement on the fold of the interaction has been applied. Figures 5.5(right) and 5.6(right) show intensity matrices from the AC and DC surface scans where full energy gamma-ray events which exhibit real charge in only one AC and one DC strip are included. These plots show a drop in intensity when the collimator is positioned over the inter-strip boundaries[1]. This effect is due to a reduced number of events in which only one pixel records real charge. This scenario, alluded to previously, occurs when the charge carriers resulting from a gamma-ray interaction in or close to the strip gap are collected by two adjacent electrodes. This type of event may be said to result in charge sharing. The low probability of Compton scattering at 59.4keV (5% of the photoelectric absorption cross section) suggests that the vast majority of photopeak events registering a fold greater than one will be due to charge sharing. The data recorded from the ^{241}Am scan therefore provides an opportunity to investigate this event type as the contribution from Compton scattering may be assumed to be negligible.

5.2.1 Charge Sharing in the Inter-Strip Gap

In [Amm00], Amman and Luke demonstrate how the charge cloud produced following a gamma-ray interaction may be split by the warping of field lines between electrodes, resulting in charge being collected by two adjacent electrodes. This may result in the calculation of a fold which is (erroneously) indicative of a Compton scatter event, leading to complications in any subsequent data analysis. In order to quantify the fraction of charge sharing events in the SmartPET1 ^{241}Am surface scan, the difference of the left and right response matrices in Figures 5.5 and 5.6 is taken on a (1mm x 1mm) pixel-by-pixel basis. The resulting matrices are shown in Figure 5.7 and reveal that around 10% of ^{241}Am gamma rays incident on the AC face result in charge sharing (Figure 5.7(left)) while performing a similar analysis for the DC surface scan yields a value of 5% (Figure 5.7(right)). For gamma rays incident on the DC coupled face the analysis is complicated somewhat by the charge loss discussed in the previous section.

Interestingly, the intense regions in Figure 5.7(left) do not correspond to strip gaps on the AC face of the detector, but rather those on the opposite (DC) face showing that for shallow interactions near the AC surface, charge sharing occurs more preferentially between the distant DC coupled contacts. In Figure 5.7(right) it appears, for gamma rays incident on the DC face, charge sharing occurs almost equally on both the AC and DC coupled contacts. However, the presence of event losses in the AC inter-strip gap in the

---

[1] An anomaly exists where no significant drop in counts is observed on the boundary between strips DC10 and DC11. This is likely to be due to complications arising from a defect in DC11 which is discussed in subsequent sections.

matrix shown in Figure 5.6(left) will reduce the difference observed when performing the subtraction. This results in the matrix in Figure 5.7(right) showing a falsely low intensity in the regions corresponding to AC strip gaps. It is therefore proposed that for gamma rays incident on the AC face charge sharing occurs preferentially between DC coupled strips while for gamma rays incident upon the DC face, charge sharing is more likely to occur between AC coupled strips. That is, for gamma rays which deposit their energy in shallow interactions near a given face, charge sharing is more likely to occur between strips on the opposite face. This is believed to be due to the long drift time toward the opposite face maximising the probability of the charge cloud splitting.

As the charge sharing mechanism is a consequence of regions of weak lateral electric field between adjacent strips, and the strength of field is likely to fall off as a function of lateral distance, it follows that one would expect that in a charge sharing event, the amount of charge collected by a given electrode relative to its neighbour will vary as a function of interaction position. This hypothesis has been tested by producing energy spectra for all AC and DC strips involved in charge sharing events for gamma rays incident on the AC face. Spectra for typical AC and DC coupled strips are shown in Figure 5.8(left) and (right) respectively. In order to remove the complication of charge loss events, these spectra were produced using events where the total energy collected falls within the sum ^{241}Am photopeak and more than 5keV is recorded in each of two adjacent strips. Both spectra show local maxima at a few keV and just less than 60keV, while there is a minimum at around 30keV. This minimum is believed to correspond to an interaction equidistant from two electrodes resulting in charge being shared equally between the contacts in question. The shape of the spectra presented is thought to be characteristic of the electric field distribution between the contacts. The strong splitting of field lines between adjacent AC strips results in high probability of non-equal charge sharing while Figure 5.8(right) shows a somewhat different distribution, the energy collected being much more evenly distributed due to the less intense splitting of field lines between DC electrodes. The high probability of non-equal charge sharing exhibited between AC coupled strips indicates it is likely that one strip may collect an amount of charge below the low energy threshold used to define collection of real charge. This may explain the appearance of events referred to as charge loss in Figure 5.6(left) but not Figure 5.5(left). The difference between the number of counts

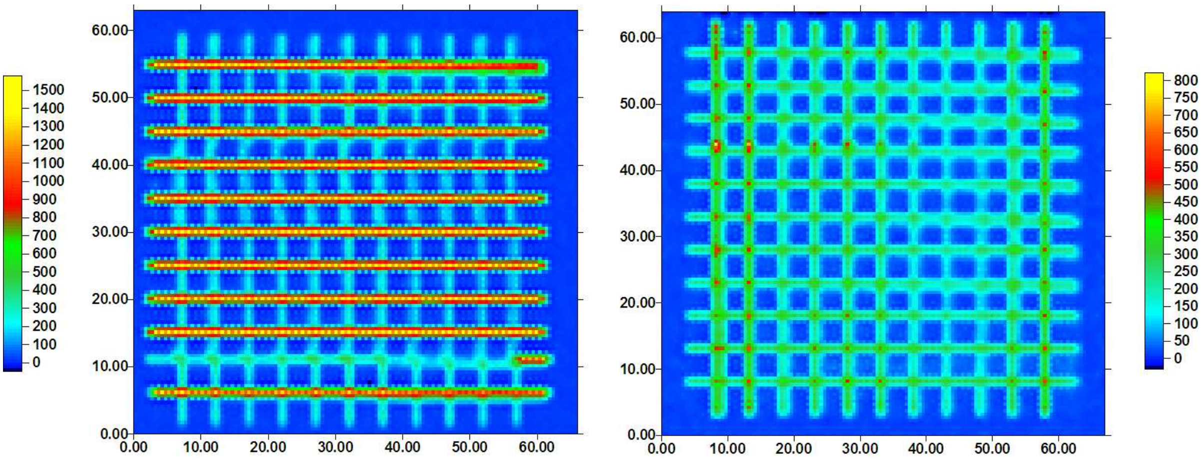

Figure 5.7: Response matrices from a high precision ^{241}Am scan of the surface of the SmartPET1 detector. The maps show the number of full energy events registering a pixel fold greater than one for gamma rays incident on the AC face (left) and the DC face (right).

in the two spectra results from the increased charge sharing between DC contacts relative to AC contacts.

It has not been possible to apply an event-by-event correction at this stage although it is likely that analysis of the charge pulse leading edge may hold the key to differentiating between charge sharing events and true Compton scattering [Mih05]. In order to facilitate the development of such a technique it may be prudent to perform a high precision scan measurement using a more finely collimated gamma-ray beam. A collimator with diameter 0.5mm or less should be employed in scanning across the boundary between strips in order to fully understand the position dependent pulse shape response from charge sharing events.

5.2.2 Image Charge Response

As previously discussed, the use of PSA techniques is essential if the position sensitivity of the SmartPET detectors is to be optimised. Data from the ^{241}Am surface scan were used to investigate the image charge response as a function of collimator position. Figure 5.9 shows how the average transient charge pulse shape in AC05 and AC07 varies as the collimator is stepped across AC06 in 1mm steps. The asymmetry between the image charges either side of the interaction strip can be observed. At the average interaction depth of the 59.4keV

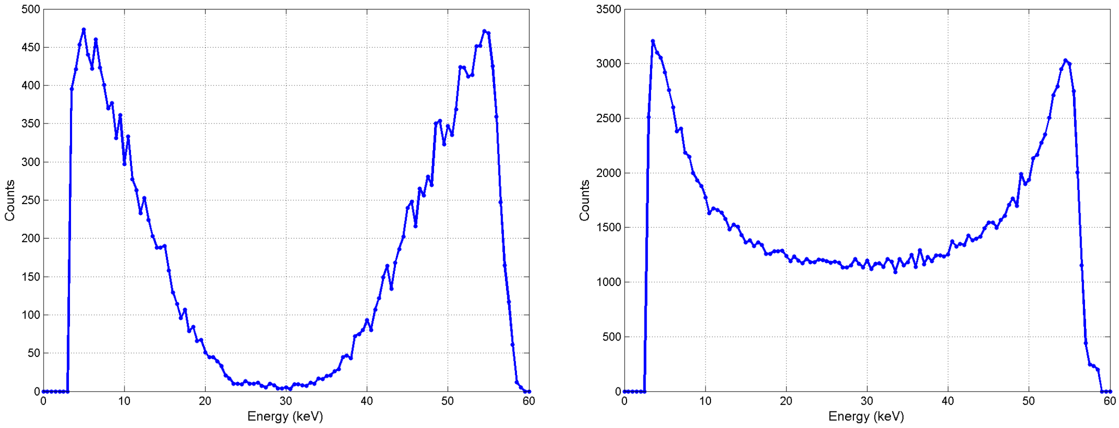

Figure 5.8: Energy spectra for typical AC (left) and DC (right) strips resulting from fold two photopeak events. These spectra are for gamma rays incident on the AC face of the detector. The shape of the distributions is believed to be indicative of the position dependent nature of the charge sharing mechanism.

gamma rays, which is typically around a millimeter [Kro99], the magnitude of the transient charges varies from $\sim 17\%$ of the incident energy to around $\sim 5\%$ as a function of lateral interaction position. The application of image charge asymmetry analysis techniques is discussed in Section 5.4.2.

5.3 ^{57}Co Side Scan

To investigate the performance of the SmartPET1 detector as a function of interaction depth, a sidescan was performed using a collimated 1850MBq ^{57}Co source. The collimated beam of gamma rays was raster scanned across the side of the detector in 1mm steps with data being recorded for 120s per position. This scan was performed using a ^{57}Co source as the relatively low energy, 122keV, of the most abundant gamma ray (93%) maximises the photoelectric absorption cross section relative to that of Compton scattering. The use of a lower energy source, such as ^{241}Am was impractical as the Aluminium can surrounding the HPGe crystal would provide sufficient attenuation as to reduce the beam intensity to an unacceptable level.

As with the ^{241}Am surface scan previously presented, the trigger was provided by a

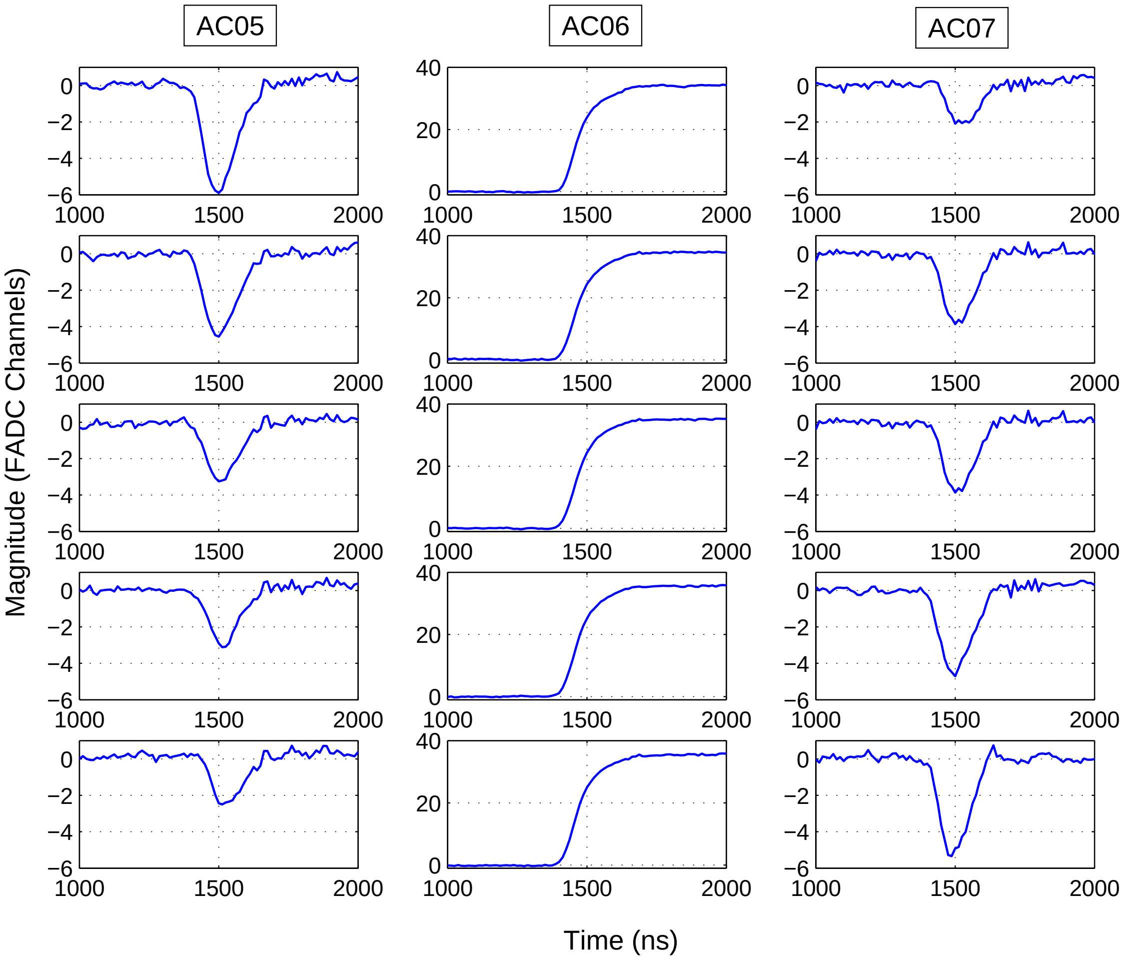

Figure 5.9: Mean pulse shape response of the SmartPET1 detector as a function of collimator position during the ^{241}Am surface scan. Mean pulse shapes are shown for strips AC05, AC06 and AC07 as the collimator was stepped along AC06 towards AC07 from AC05 (top to bottom of figure). The mean pulses are constructed from 200 single pixel hits where each event deposited full energy in AC06 and DC06. The asymmetry between image charges in neighbouring strips may be observed.

logical OR of the twelve AC coupled strips where on this occasion the CFD threshold was set to be around 60keV. The detector was scanned such that the DC coupled strips were perpendicular to the incident beam. As a result the intensity of the beam dropped off exponentially as a function of DC strip number by attenuation in the germanium. Further information on the experimental set up of this measurement may be found in [Bos07].

From the scan data, a gate of around 6keV was applied to the 122keV photopeak and an intensity matrix displaying the number of single pixel hits as a function of collimator

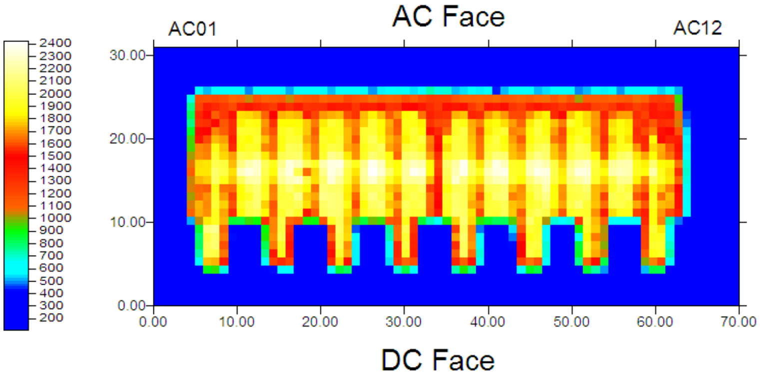

Figure 5.10: Intensity as a function of position from ^{57}Co side scan of SmartPET1. The matrix is produced from events where full energy is deposited within a single pixel. The axes show the collimator position in mm while the relative orientation of the strips is denoted.

position produced. This matrix is displayed in Figure 5.10 and while the response exhibits a good level of uniformity throughout the majority of the detector, a number of interesting features may be observed.

The regions of low intensity which appear to be cut away from the crystal near the DC face indicate the presence of some attenuating material between the beam and the HPGe crystal. This is likely to be some kind of holding structure housed within the cryostat. These structures are no longer observed when scanning with higher energy gamma-ray beams as the material no longer provides significant attenuation. This effect may be observed in the ^{137}Cs side scan presented in [Coo07a] and [Tur06]. Similarly, regions of slightly decreased intensity are observed near the AC coupled face, extending across the depth of the detector near the centre of this face. These regions are also believed to be due to attenuation in some mechanical structure, perhaps associated with the cooling mechanism. As discussed in Section 5.2 the fold requirement results in the strip boundaries being visible in the intensity matrix.

5.3.1 Risetime Response

As outlined in Chapter 3 the depth of interaction sensitivity of a planar detector may be calibrated through analysis of the charge collection time. In order to investigate this for the SmartPET1 detector, response matrices have been produced which show the mean risetime as a function of collimator position as the depth profile is scanned.

In this work the risetime has been parameterised according to fixed percentages of the magnitude of the pulse shape. Figure 5.11 illustrates how values of t10, t30 and t90 are defined. These values correspond to the time taken for the charge pulse to reach 10%, 30% and 90% of its maximum respectively. The risetime is then described in terms of T30 and T90 where T30=t30-t10 and T90=t90-t10.

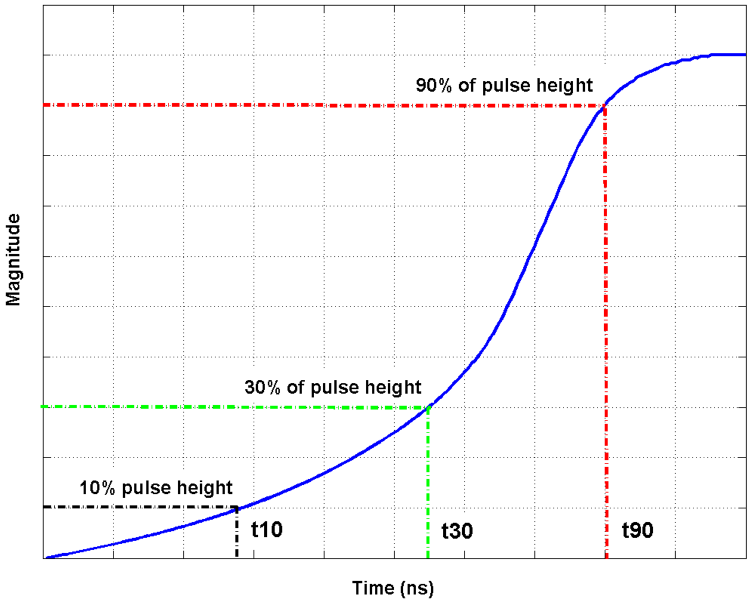

Figure 5.11: Example of a normalised charge pulse, showing how the leading edge may be parameterised in terms of its timing characteristics. The values of t10, t30 and t90 correspond to the time taken for the charge pulse to reach 10%, 30% and 90% of its maximum respectively. The risetime is then described in terms of T30(t30-t10) and T90(t90-t10).

The T90 value provides a measure of the time required for full charge collection while the T30 risetime is more closely related to the charge carrier with the shortest drift distance to its collecting electrode. The T30 risetime is therefore more sensitive to the point of interaction, reflecting the movement of charge carriers local to the interaction site [Des02].

From the ^{57}Co side scan data, the mean risetime resulting from single pixel, full energy hits was calculated for each collimator position. Four response matrices are displayed in Figure 5.12 showing mean T30 and T90 values in nanoseconds for the AC and DC faces as a function of collimator position.

These plots demonstrate the variation in risetime observed as a function of interaction

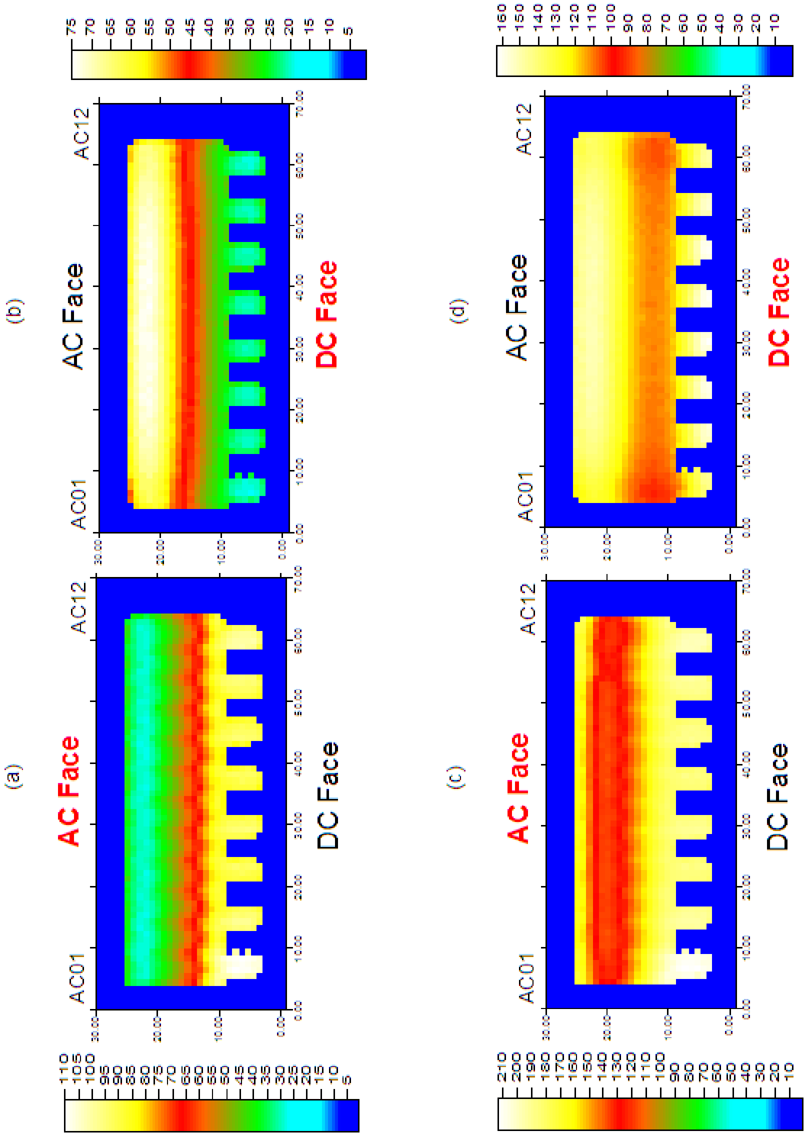

Figure 5.12: Mean risetime as a function of collimator position from the ^{57}Co sidescan of SmartPET1. The mean risetime is calculated from events depositing full energy in a single pixel. The figure shows the T30 values for the AC and DC coupled faces respectively in matrices (a) and (b) while the T90 values for the AC and DC faces are displayed in (c) and (d). The intensity map shows the mean risetime in ns where the face from which the risetime was measured is highlighted in red.

depth in the detector. It can be seen that the rise time value appears consistently longer for the AC face relative to the DC face with the AC risetimes also exhibiting a larger spread. This can also be seen by inspecting the average pulse shapes displayed in Figure 5.13. The mean pulse shape resulting from 200 full energy events in the pixel defined by AC06 and DC02 is displayed for each of the 20 collimator positions through the depth of the SmartPET1 detector. In these plots one can observe how the AC pulse shapes exhibit consistently slower timing characteristics both in terms of T30 and T90. This is perhaps explained by the difference in electron/hole drift velocities and difference in inter-strip capacitance due to the AC and DC contact geometries. The AC contact is 0.3μm thick with an inter-strip gap of 100μm while the DC contact is 50μm thick with strips separated by 300μm. A simple calculation, modelling the strip gap as a parallel plate capacitor, yields the inter-strip capacitance of AC strips as being two orders of magnitude larger than that between DC strips. If this capacitance acts at the input stage of the preamplifier then an increased capacitance may result in an apparent ‘slowing’ of the charge pulse, AC pulse shapes will therefore exhibit slower timing characteristics than DC counterparts.

By taking one-dimensional slices through the response matrices in Figure 5.12 the variation in risetime response as a function of interaction depth may be assessed from the point of view of position sensitivity. Figure 5.14 shows how the mean risetime varies as a function of position for both the AC and DC faces. The plots are constructed by taking a slice through the risetime matrices at x = 38mm and show collimator position in mm where position one is close to the DC coupled face and position twenty near the AC face.

The T30 risetime for a given face is short for interactions close to that contact and rises to a maximum for interactions occurring near to the opposite face. The point at which the T30 for each face is equal corresponds to the point in the detector where each charge carrier experiences the same drift time to its collecting electrode. As the drift velocity of holes is 30% lower than that of electrons [Mih00] this point is offset from the centre of the depth profile towards the AC coupled contact at a collimator position 15mm from the DC face. The plot of T90 against depth shows a significant difference in response between the AC and DC coupled contacts. The DC risetimes drop to a minimum at around 10mm from the DC face before quickly rising again. This minimum should correspond to the position in the detector where the electron and hole collection times are equal but appears inconsistent

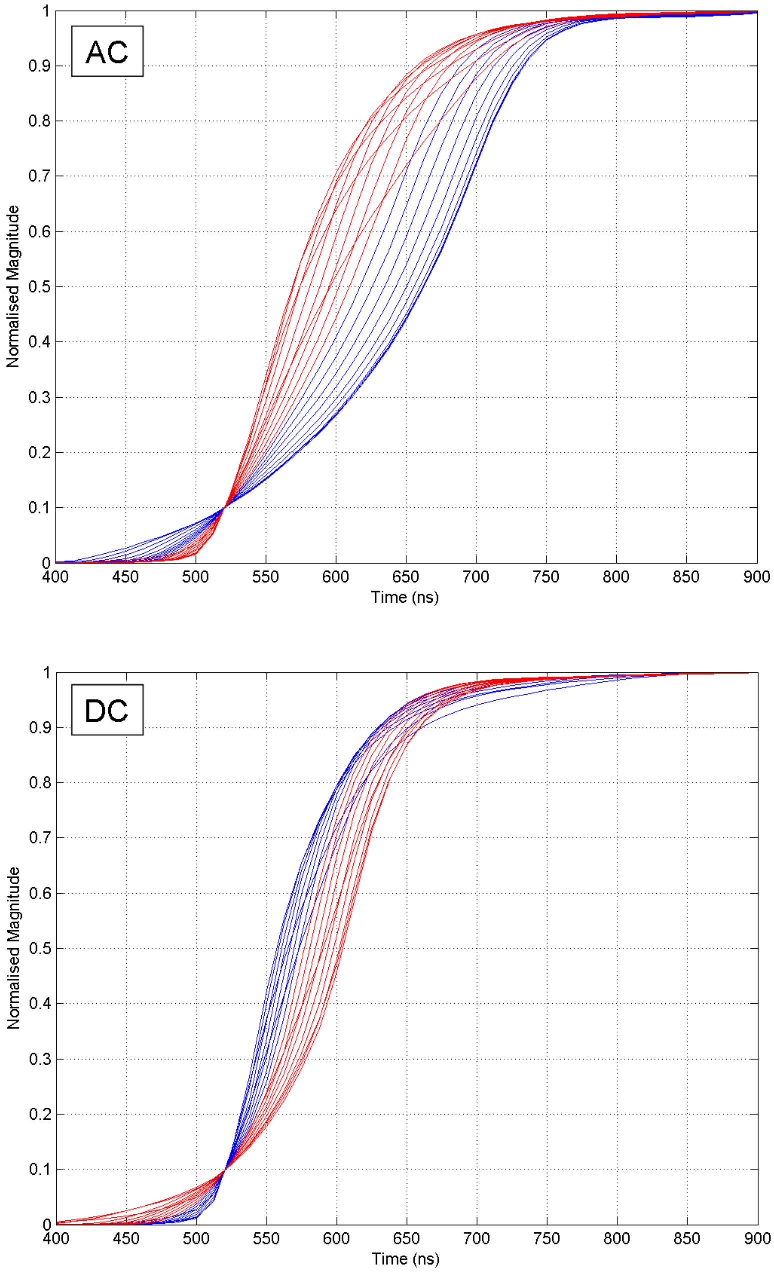

Figure 5.13: Mean pulse shapes for each of twenty collimator positions through the depth profile of the SmartPET1 detector during the ^{57}Co side scan. The mean pulse shapes were calculated from 200 events depositing full energy in the pixel defined by AC06 and DC02 where the top plot shows the pulse shape response of AC06 and the bottom plot DC02. Pulse shapes in red correspond to collimator positions close to the DC face while those in blue represent positions close to the AC face. The mean pulse shapes have been time aligned at the t10 value for display purposes. These plots show the strong variation in pulse shape response on a millimeter by millimeter basis through the depth of the SmartPET1 detector.

with both the position derived from the T30 plot and the difference in charge carrier drift velocity. The AC T90 varies linearly throughout the bulk of the crystal depth reaching a minimum at around 18mm from the DC coupled face before rising again.

Taking the saturated charge carrier drift velocity along the <100> axis to be 10^7 cm/s (Figure 3.10 and [Mih00]), the maximum charge collection time for the 20mm thick SmartPET detectors is expected to be ∼200ns. The minimum expected charge collection time is ∼100ns, based on the assumption that the point where positive and negative charge carriers have the same drift time is located at the midpoint between the AC and DC faces[2]. The results presented in Figures 5.12 and 5.14 therefore suggest that the T90 response of the AC face is consistent with this calculation while the DC T90 values are generally too fast.

Studying the pulse shapes in Figure 5.13 reveals that in many cases for DC pulse shapes, a significant amount of information is contained in the part of the leading edge after the T90 point as the charge pulse continues to rise slowly to its maximum value. Although the reason for this effect is unclear it implies that the discrepancy between AC and DC risetime response is due to the parameterisation applied. Based on these findings it is perhaps worth investigating the use of a risetime parameter such as T95 in the future, although the presence of electronic noise may make this problematic.

From the plots presented in Figure 5.14 one can observe for interactions near the DC face there is little or no variation in either the AC or DC T30 value over the first four or five millimeters while the T90 plot shows a similar effect for the AC risetime. In addition it can be seen how interactions close to either contact can result in the same T90 value. This is particularly apparent for the DC coupled contact and will result in ambiguities in any depth of interaction calculation as will the loss of sensitivity in T30 for interactions close to the DC contact.

Risetime Correlation Technique

In [Bos07] the use of a single parameter approach to risetime analysis was proposed. However, from the results presented therein and those in Figures 5.12 and 5.14 it can be seen how the ambiguities in the rate of change of risetime would result in regions of low posi-

---

[2] In reality this point will be offset towards the hole collecting face due to a difference in saturated drift velocity between the two species of charge carrier.

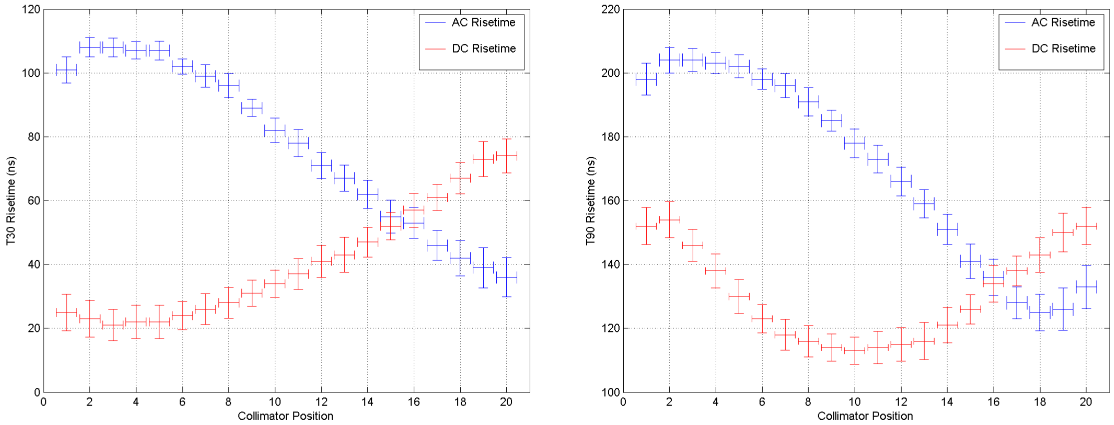

Figure 5.14: Plots showing the variation of mean risetime as a function of collimator position for a cross section through the ^{57}Co side scan response matrix. The variation in T30 for the AC and DC face is shown on the left while the plot on the right displays the mean T90 value for both contacts. The collimator position, in mm, is relative to the DC coupled face.

tion sensitivity within the detector. The use of T30-T90 risetime correlation techniques to resolve this issue was first proposed in [Kro96] and has since been applied to a segmented closed end coaxial HPGe detector in [Des05a] and a Clover HPGe detector in [Gro05]. Parameterisation in terms of both the T30 and T90 risetime values provides a more accurate representation of the charge pulse leading edge and therefore the charge collection process. In this way the ambiguities which occur in the distributions of single risetime parameters may be overcome. The application of two-dimensional gates to T30-T90 response matrices allows discrete regions through the depth profile of the SmartPET detectors to be selected. In Figures 5.15 and 5.16 the measured T30 versus T90 values at different interaction depths in the SmartPET1 detector are shown for strips AC06 and DC02 respectively. These plots were produced from the ^{57}Co side scan where the depth of interaction is known precisely. The depth, in mm, is defined as the distance between the DC face and the collimator position. These plots are produced for events which deposit full energy in the pixel defined by AC06 and DC02 while the matrices shown in Figure 5.17 show T30-T90 correlation plots for any event depositing energy in AC06 or DC02.

Once again the discrepancy between AC and DC risetime response is apparent. The AC T30-T90 matrix in Figure 5.17 shows how, for interactions close to the DC face, the AC pulse shapes exhibit a slow initial charge collection resulting in large values of T30 biasing the shape of the distribution.

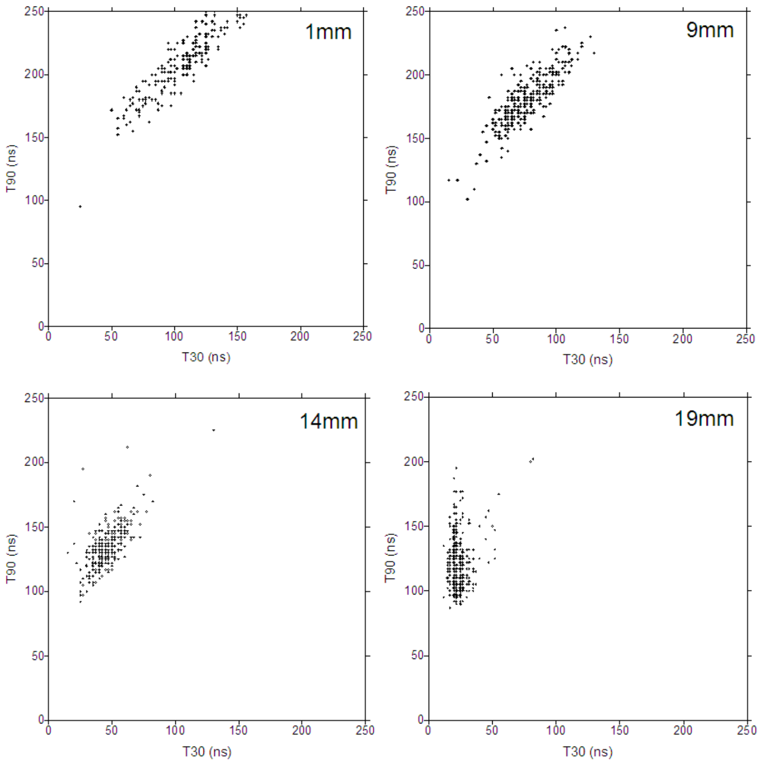

Figure 5.15: T30 vs T90 risetime spectra for strip AC06 at four different collimator depths. The depth refers to the position of the collimator relative to the DC face of the detector.

From Figures 5.15 and 5.16 it can be observed how the cluster of T30-T90 values shifts as a function of collimator position. While this approach does indeed reduce the ambiguity in the calculation of interaction position, reduced sensitivity is still observed for interactions near the DC face. For both AC and DC risetime values, the shift in the distribution occurring between depths of 1mm and 9mm from the DC face is much less significant than the changes observed near the AC face.

In Figure 5.18 two dimensional gates have been applied to the complete T30-T90 matrix for AC06. These gates effectively split the depth of the detector up into five discrete regions of sensitivity. Throughout this work the number of two-dimensional gates applied is limited to five. Recent work has however suggested that this approach may be extended to provide ten or more discrete regions of sensitivity [Gri07].

Based on the five positions derived, the mean pulse shape resulting from 200 full energy,

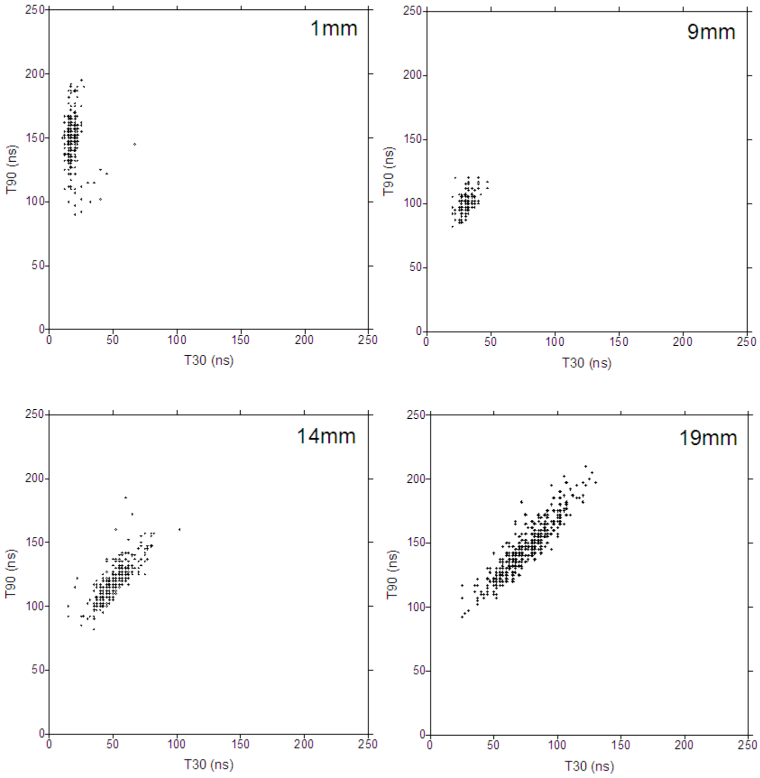

Figure 5.16: T30vsT90 risetime spectra for strip DC02 at four different collimator depths. The depth refers to the position of the collimator relative to the DC face of the detector.

single pixel (defined by AC06/DC02) interactions in each region was produced. These pulse shapes are shown to the right of the image and show good agreement with the expected trend from the mean pulse shapes presented in Figure 5.13, providing added confidence in this method for depth of interaction identification. In this figure the gating procedure has been arbitrarily applied to the AC matrix to provide an example of the technique. As discussed later, in order to identify the depth of interaction on an event-by-event basis the same approach is applied to all AC and DC coupled strips. Similar results from a ^{137}Cs surface scan of the detector are presented in [Coo07b].

5.4 ^{22}Na Flood Measurement

As the SmartPET detectors form part of a PET system the performance of the detectors at 511keV, the energy of interest for PET was investigated. Both SmartPET detectors were placed in the rotating gantry with a 0.0307MBq ^{22}Na point source at the centre of

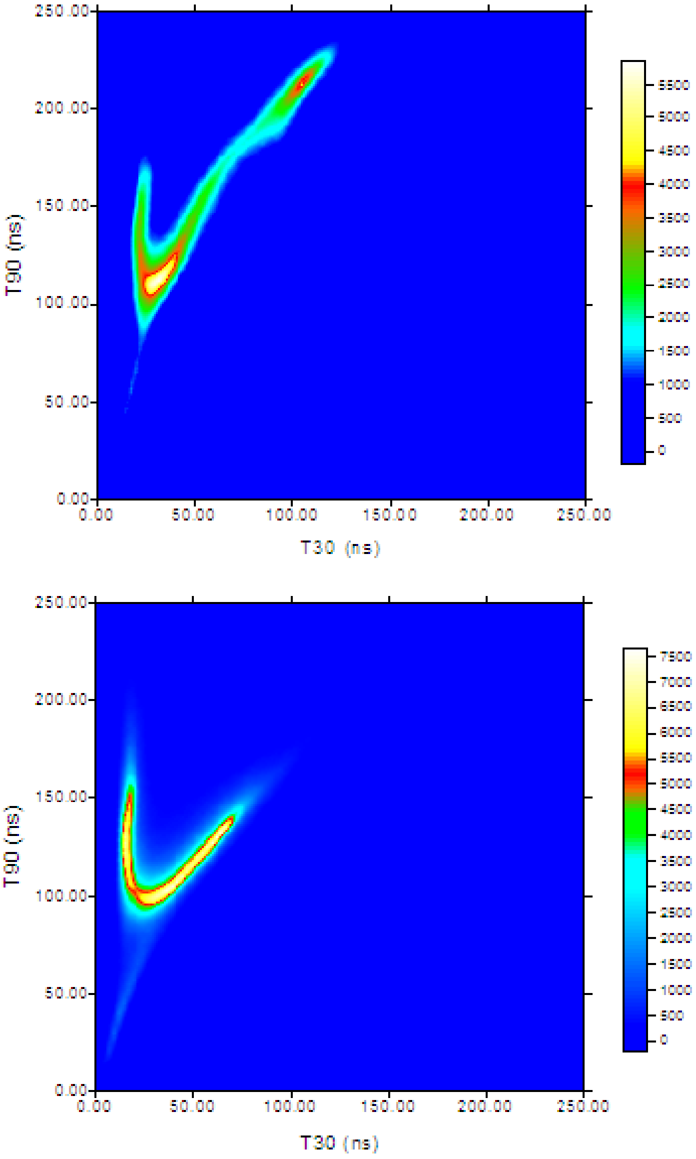

Figure 5.17: T30 versus T90 risetime distribution plots for all events depositing energy in AC06 (top) and DC02 (bottom) during the ^{57}Co side scan of SmartPET1.

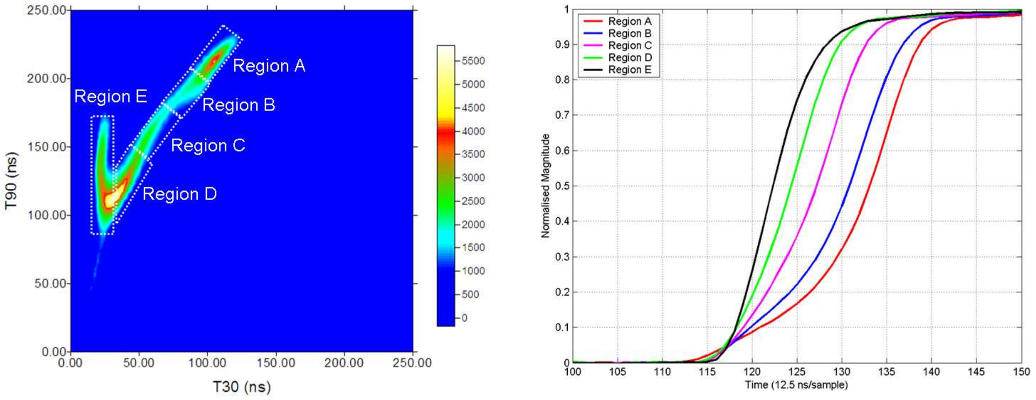

Figure 5.18: The image on the left shows the T30-T90 response matrix for all events in AC06 during the ^{57}Co sidescan along with a series of two-dimensional gates applied to select discrete regions of depth. The mean pulse shapes associated with 200 full energy events in each region are shown on the right. These mean pulse shapes follow the expected trend demonstrating the effectiveness of the risetime correlation technique.

the field of view, 65mm from the front face of each detector. Data were collected in singles mode with a CFD threshold of ∼60keV resulting in a trigger request rate of 2.2kcps per detector. Analysis of this data has been used to provide calibration of the three-dimensional position sensitivity of the SmartPET detectors. These calibrations have then been used to develop parametric PSA techniques which may be applied to PET imaging data on an event-by-event basis.

5.4.1 Depth of Interaction Identification

From analysis of the ^{57}Co sidescan, it has been demonstrated how the paramaterisation of risetime response may allow the depth of a gamma-ray interaction to be calculated. The risetime correlation approach presented has been applied to the ^{22}Na flood measurement and a T30-T90 matrix produced for each of the 24 strips on each detector. Figure 5.19 shows the distributions for all AC coupled strips on the SmartPET1 detector. The coefficients describing each gate were then tabulated in order that they may be applied event by event during analysis of PET data. It is perhaps worth noting that while in this case individual gates have been calculated for each of the 48 strips, the response of the two detectors is extremely similar and, in principle, a set of universal AC and DC gates may reasonably applied.[3]

5.4.2 Image Charge Asymmetry

In analysis of SmartPET data sets, the spatial resolution in the lateral plane is refined using image charge asymmetry approaches. Data from the flood measurement were used in order to calibrate the image charge response of the SmartPET detectors. For all events where fold_{AC}=fold_{DC}=1, the areas of the image charges present in the strips either side of the hit strip were measured. The image charge asymmetry parameter was then calculated on an event-by-event basis according to Equation 3.19. This provides an asymmetry distribution for each of the forty non-edge strips on the two SmartPET detectors. The asymmetry distributions for the twelve AC coupled strips of SmartPET1 are shown in Figure 5.20. These plots show Gaussian like distributions with a mean of zero. From Equation 3.19 all image charge asymmetry values must lie between limits of -1 and 1, but in Figure 5.20 the values are rescaled due to the technical constraints of the analysis software.

The image charge asymmetry distribution of each strip has been used to provide a calibration of the position sensitivity. In doing this two major assumptions are made:

1. The image charge asymmetry parameter is directly related to the position of interaction within a given strip. That is, a value of around zero results from an interaction close to the centre of the hit strip, while values of -1 and 1 indicate interactions have occurred towards strip boundaries.
2. There is an equal probability of an interaction occurring anywhere in a strip.

A limitation of this PSA technique arises from the second of these two assumptions. In calibrating the image charge asymmetry of the SmartPET detectors, the asymmetry distributions are generated using only single pixel hits. Placing this constraint on the event fold may bias the data towards those events interacting near the centre of a given strip. Events interacting near strip boundaries may be more likely to Compton scatter out of the strip resulting in the event being omitted from the asymmetry calibration procedure. In

---

[3] With the exception of strip DC11 on SmartPET1 where a high probability of charge sharing results in systematically longer T90 risetimes and a slight distortion of the distribution shape.

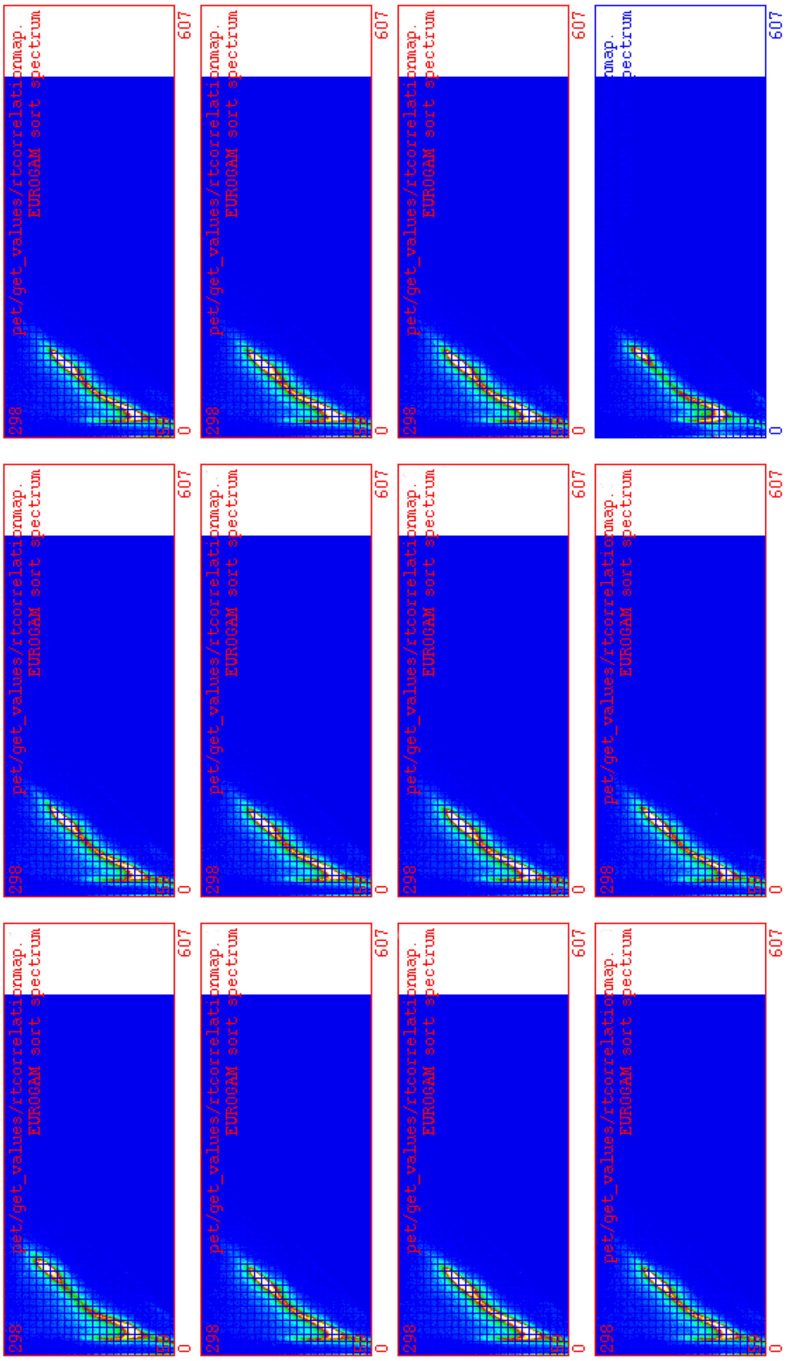

Figure 5.19: The T30-T90 matrix associated with the twelve AC coupled strips of the SmartPET1 detector. These matrices were produced from all events depositing less than 520keV during the ^{22}Na flood measurement. A high level of uniformity may be observed in the response of the twelve strips.

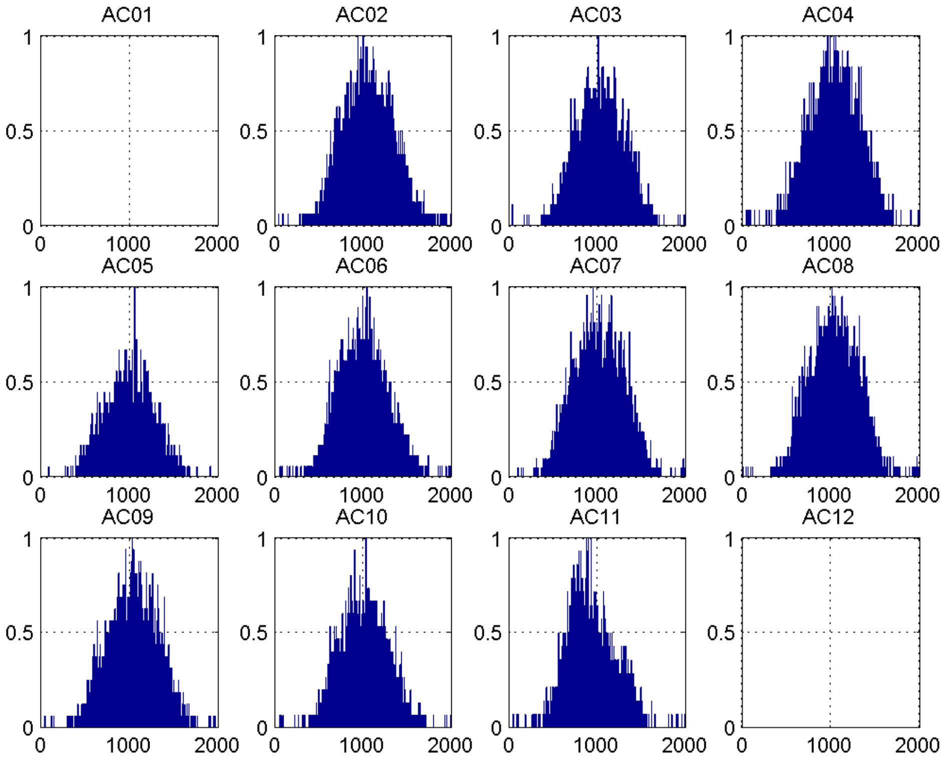

Figure 5.20: Histograms of the image charge asymmetry distributions for each of the twelve strips on the AC coupled face of SmartPET1. The x-axis of each distribution, which shows the value of the asymmetry parameter, has limits of -1 and 1 but are rescaled here due to technical considerations with the analysis software. The edge strips (AC01 and AC12) do not have asymmetry distributions as they lack two adjacent neighbour strips in which to observe image charge. The y-axis shows the number of counts individually normalised to the maximum of each distribution.

addition, no methodology for dealing with gamma rays undergoing multiple interactions in the same pixel is included in this analysis technique.

In this work, each distribution has been divided into five regions of equal area. The boundaries of these sections were then stored in a look up table which, along with the gate coefficients generated from the risetime correlation matrices, can be applied to further experimental data on an event-by-event basis to assign a sub-strip hit position for every event. By splitting up these distributions in this way, each substrip has a size of 1mm which is consistent with the limit of spatial resolution expected to be achievable with HPGe detectors at this time [Bru06], [Des05b], [Ide03].

This method has previously been successfully applied to SmartPET imaging data in [Mat06] and [Coo07b] both of which include a validation of the approach using a finely collimated beam of gamma rays. According to [Mat06], over 78% of events are either identified correctly or with an error of one sub-strip with the correct sub-strip being correctly identified at least 50% of the time.

5.4.3 Interactions in Edge Strips

In the previous section it has been shown how one limitation of the image charge asymmetry approach to PSA is its inability to process interactions occurring in edge strips. This is due to the requirement of a strip on either side of the hit strip in which to observe image charge. As a result a different approach has been developed which allows the image charge in the single neighbouring strip to be used to calculate the gamma-ray interaction position. Using the assumption that the area of an image charge varies due to the influence of three parameters:

1. The energy deposited by the gamma ray
2. The depth of interaction
3. The lateral interaction position,

one can use knowledge of two of these variables to calculate the third. In this way, by calculating the interaction depth through the risetime correlation method, a parameter which varies as a function of lateral interaction position can be defined as

$$A_{single} = \frac{Q_{L/R}}{E_\gamma} \tag{5.1}$$

where $Q_{L/R}$ is the area of the single image charge to the left or right of the hit strip and E_γ is the energy deposited in the gamma-ray interaction.

This technique has been validated by performing a surface scan of the SmartPET1 detector with a 70MBq ^{137}Cs source incident on the AC face of the detector through a 1mm collimator. As the collimator was scanned across strip AC01 in 1.0mm steps, the depth was identified using the risetime correlation approach and the single image charge parameter calculated event-by-event according to Equation 5.1. Figure 5.21 shows how this parameter

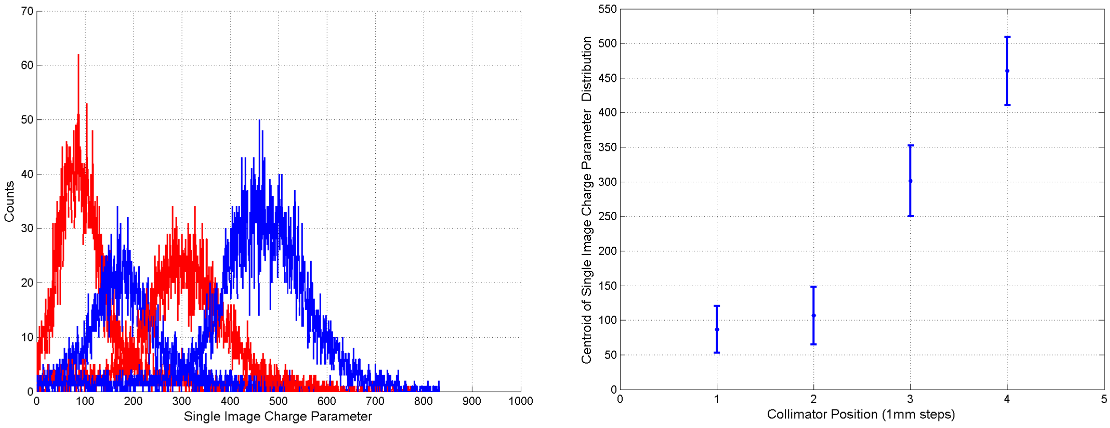

Figure 5.21: Left: Histograms showing the variation of the single image charge parameter as a function of step position across strip AC01 on SmartPET1 in 1mm steps. The image charge in AC02 is used to calculate the parameter for events identified as occurring in the central region of the detector (full energy deposition is demanded from single pixel hits). Right: The centroid of the distribution as a function of collimator step position. As the collimator position moves across AC01 towards AC02 the value of the parameter increases.

varies as a function of collimator position for events identified as interacting in the central region of the detector's depth profile.

From these results it is estimated that the technique provides roughly the same accuracy as the image charge asymmetry approach. However, the use of this method is complicated by the relatively large uncertainty in the identification of interaction depth.

Using the ^{22}Na flood data, histograms of the single image charge parameter at each of the five interaction depths have been produced for each edge strip. Figure 5.22 shows the five distributions computed for strip AC01 on SmartPET1 where the depth refers to the region of depth selected from the risetime correlation matrix for AC01. Depth 1 corresponds to interactions near to the AC face while Depth 5 refers to interactions close to the DC coupled contact.

These distributions are split into five regions of equal counts in a similar way to that previously discussed for the image charge asymmetry parameter in Section 5.4.2. Once again the coefficients describing the boundaries between regions are stored in a look-up table, as a function of calculated depth, for application in PET analysis. It may be observed from Figure 5.22 that the distributions of A$_{single}$ exhibit low statistics in comparison to the

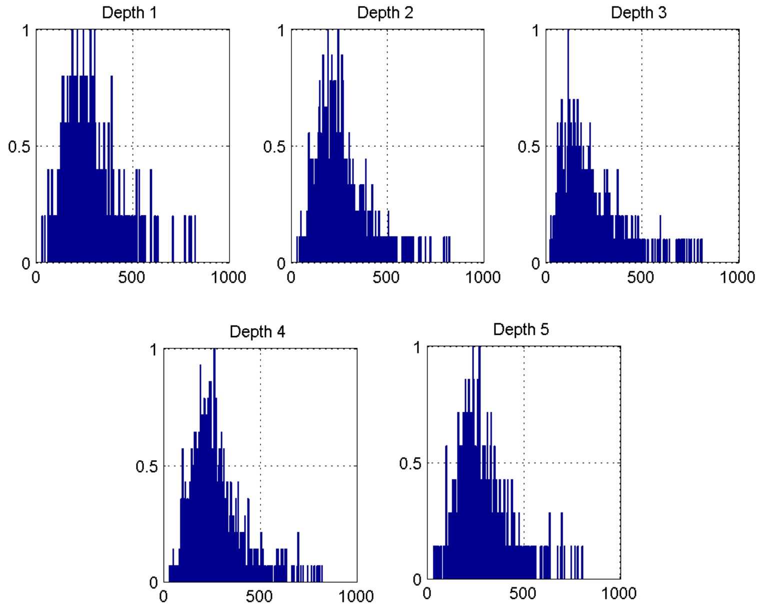

Figure 5.22: Histograms showing the single image charge parameter for interactions in strip AC01 of SmartPET1. In order to calibrate position sensitivity a histogram exists for each of the five depth regions defined by the T30 vs T90 risetime correlation method. Here, depth 1 refers to interactions close to the AC coupled face and depth 5 to interactions close to the DC face. The x-axis shows the value of the single image charge parameter while the y-axis denoted the number of counts individually normalised to the maximum of each distribution.

image charge asymmetry distributions presented previously. This is a result of the relatively small fraction of events depositing full energy in edge strips and the subsequent process of producing an individual distribution for each of five regions of depth.

5.5 Charge Collection Performance

Analysis of the prototype GREAT planar HPGe detector [Dob05] revealed incomplete charge collection leading to degradation of spectroscopic performance. Two major mechanisms of charge loss were investigated and both were found to be due to the nature of the contacts. This is illustrated by the significantly superior charge collection observed on the implanted contact over the drifted contact and the increased charge loss observed on the saw cut face. The SmartPET detectors use new thin contact technology developed by ORTEC, the nature of which is propriety. The charge collection performance of the SmartPET1 detector has been investigated by uniformly illuminating the AC face of the detector with an uncollimated ^{152}Eu source. In addition, a second measurement was performed using a ^{137}Cs source in order to develop a method for the correction of charge sharing resulting from interactions in DC11.

5.5.1 AC vs DC Charge Collection

Following a gamma-ray interaction the number of electrons liberated must be exactly equal to the number of holes. As a result, the energy derived from the charge pulse should, within the associated uncertainties, be identical for each face. If however, charge is lost as it drifts towards its collecting electrode then this cannot be the case and energy resolution may be reduced. In order to investigate this effect the total charge collected on the AC contact was plotted against the total charge collected on the DC contact on an event by event basis for all events. For an ideal detector this plot should take the form of a straight line through the origin where $\text{Energy}_{AC} = \text{Energy}_{DC}$. This result for SmartPET1 is displayed in Figure 5.23 where a logarithmic intensity scale is applied.

This result shows that for the vast majority of events an identical amount of charge is collected on both faces of the detector. The regions of high intensity correspond to the characteristic ^{152}Eu gamma rays (photopeaks). For a very small fraction of events (0.7% of 122keV gamma rays) incomplete charge collection occurs on the DC coupled face. These events are represented by the vertical line running from the diagonal toward the x-axis and, if occuring in sufficiently large numbers would typically result in low energy photopeak tailing in a gamma-ray spectrum. It is likely that these events occur from the same mechanism discussed in Section 5.2 and the effect can be seen to become less severe with increasing gamma-ray energy.

5.5.2 Fold 2 Charge Loss Events

A second charge loss mechanism may also take place which results in charge being lost in the dead region of the interstrip gap [Cob02]. In order to investigate this effect in the SmartPET detectors, fold 2 events were selected and the charge collected on each strip plotted in the form of a gamma-gamma energy matrix. These matrices have been produced for two distinct fold two scenarios; where the two strips collecting real charge are adjacent

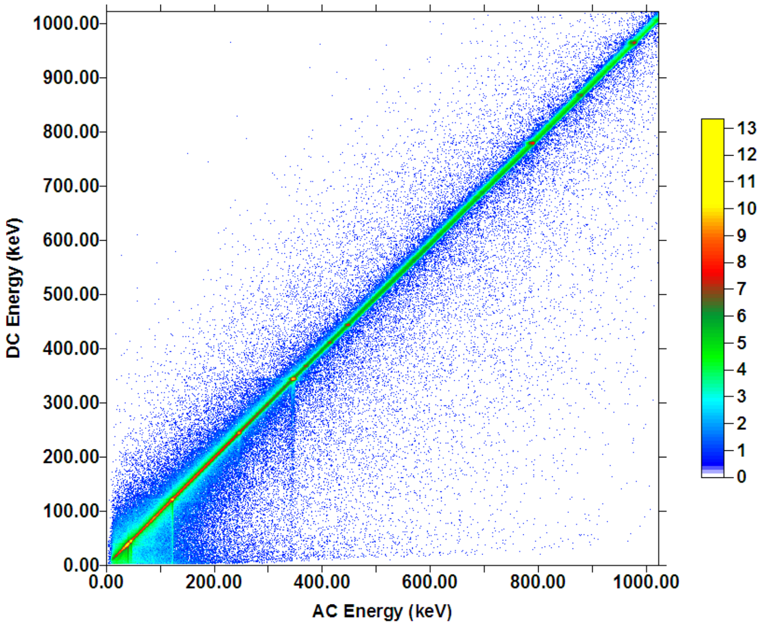

Figure 5.23: A plot of the energy collected on the AC face of SmartPET1 against the energy collected on the DC face. This plot is produced from data recored from an uncollimated ^{152}Eu source incident on the DC face of the detector. All fold are included in the analysis and the number of counts is displayed on a logarithmic scale.

(left) and for events where the two strips are non-adjacent (right). In each case the matrices have been produced for both the AC and DC coupled faces[4] of the SmartPET1 detector with Figure 5.25 showing the results for gamma-rays incident on the AC face. In these plots the diagonal lines represent events where summing the two energies yields full photopeak energy without loss of charge. In [Dob05], an analysis of the GREAT (Gamma Recoil Electron Alpha Tagging) planar HPGe detector, the presence of arcs below these diagonal lines is shown to be indicative of the charge loss mechanism discussed. This is demonstrated in Figure 5.24, a gamma-gamma matrix for fold two events recorded on the AC coupled face of the GREAT planar detector. The matrices presented, and those for the DC face, which are not displayed, show no presence of such characteristics and as a result one must conclude that the evolution of contact technology has resulted in improved charge collection performance.

Projecting the diagonal line corresponding to the 122keV and 344keV gamma rays onto

---

[4] Due to the subsequently discussed mechanical fault on DC11, this strip was excluded from the analysis.

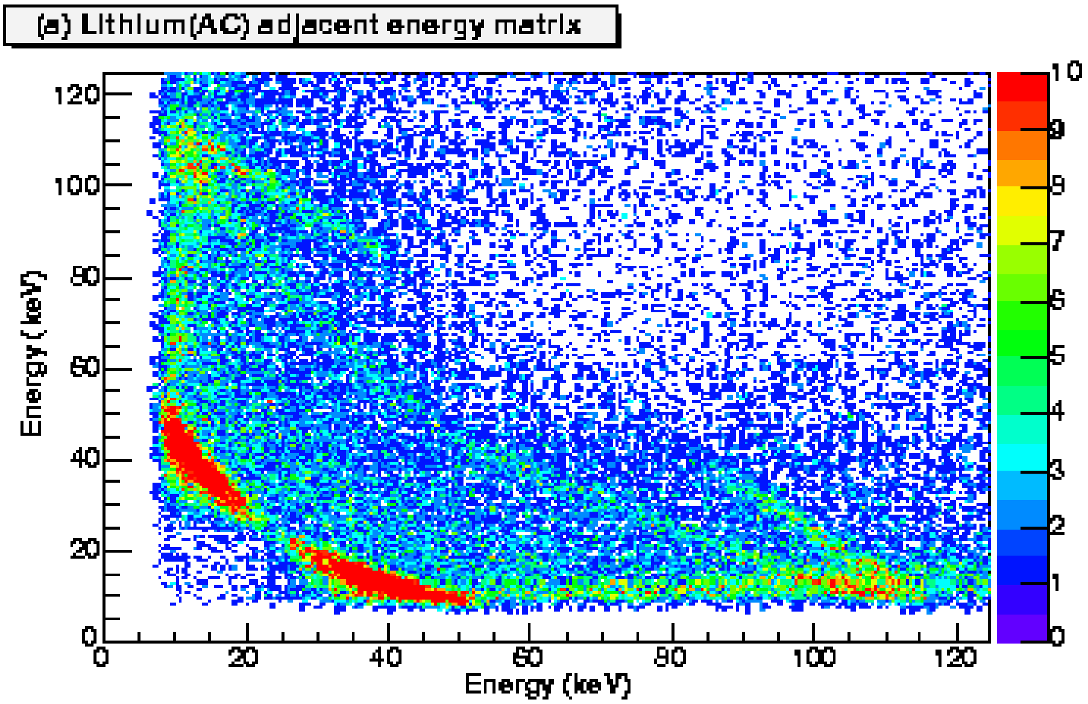

Figure 5.24: Gamma-gamma matrix from the GREAT planar detector [Dob05] showing energy deposition from 60keV and 122keV fold two events recorded on the AC coupled face. The presence of arcs below the diagonal lines are indicative of charge loss.

the x-axis produces the energy distributions shown in Figure 5.26. These distributions of energy deposition are representative of the Compton scattering profile associated with each energy. It can be seen that as the gamma-ray energy increases the profile becomes much more forward focused, preferentially depositing similar energy in each of the two strips. If the same distribution for the 122keV gamma ray is produced for events which scatter to non-adjacent strips, the energy deposition pattern shown in Figure 5.27 results. Here we see that the number of counts in the region around 60keV has been drastically reduced. This is believed to be due to geometrical constraints resulting in a region of ‘forbidden’ energy deposition. That is, if a 122keV gamma ray is to scatter through an angle such that it may cross two strip boundaries and undergo a second interaction in a non-adjacent strip, the range of energies it may deposit is limited. Where the gamma ray interacts in two neighbouring strips, the geometrical factors are not the same and therefore this energy range is no longer ‘forbidden’.

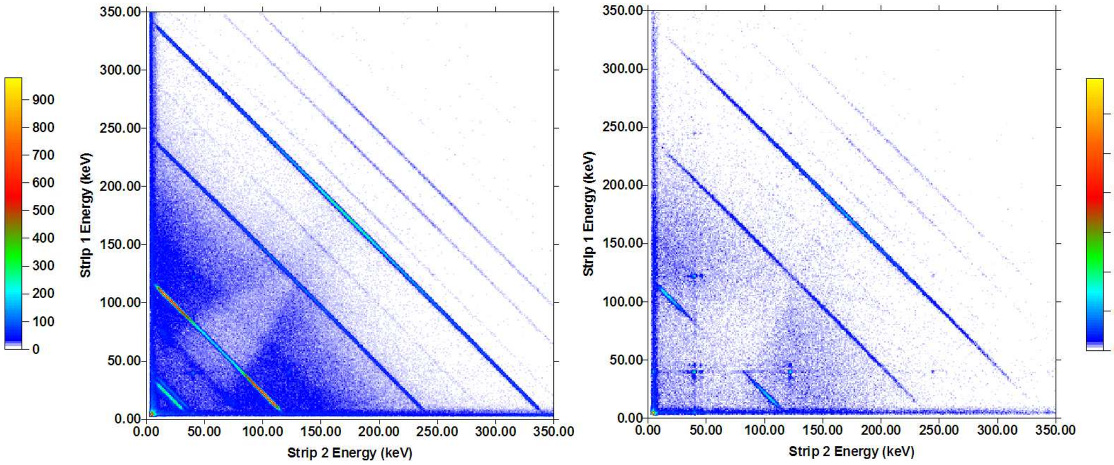

Figure 5.25: Gamma-gamma matrices for events scattering between two AC coupled strips. The matrices show all events which scatter between adjacent (left) and non-adjacent (right) strips.

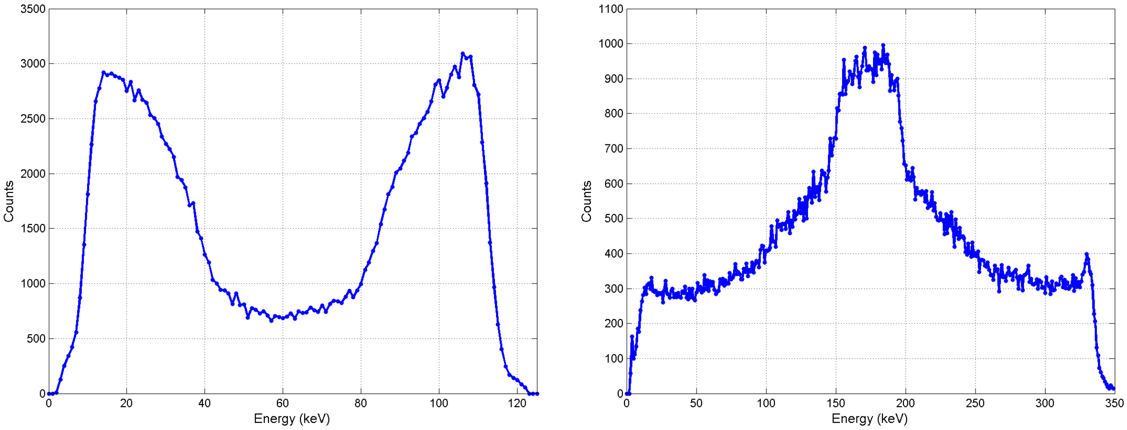

Figure 5.26: Energy profiles associated with 122keV (left) and 344keV (right) gamma rays scattering between adjacent AC coupled strips.

5.5.3 DC11 Charge Sharing Correction

During tests of SmartPET1 performed at ORTEC Oak Ridge, strip DC11 was reported to exhibit poor energy resolution [San04]. Upon arrival at Liverpool, tests revealed several anomalies in the performance of the strip including:

- Double peaking at intermediate to high gamma-ray energies. An example of this can be seen in Figure 5.30(left) which shows the 662keV photopeak from a ^{137}Cs spectrum.
- Abnormally long T90 risetime. Figure 5.28 shows the average DC T90 risetime re-

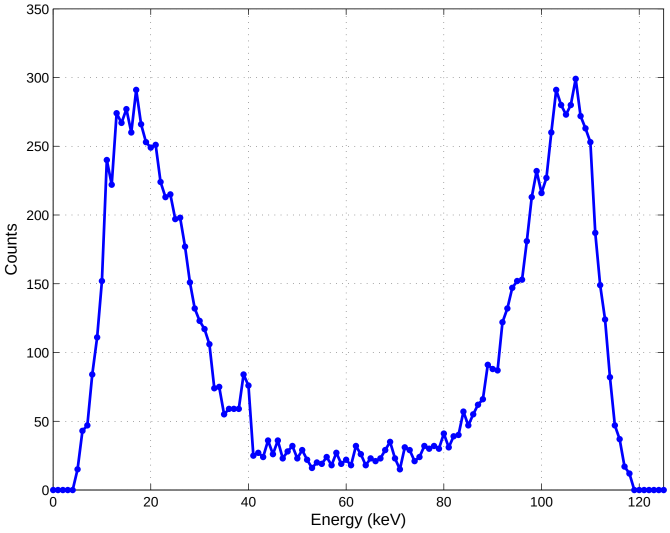

Figure 5.27: Energy profile of 122keV gamma rays scattering between non-adjacent AC strips.

sponse of the SmartPET1 detector as a function of position for a 1mm collimated beam of ^{241}Am gamma rays incident on the DC face. The detector displays uniform response across all DC strips with the exception of DC11 which exhibits consistently longer values of T90. Close to the bonded contact the risetime response is consistent with other strips but quickly degrades within ∼5mm from this point.

- The strip rarely registered a fold one event.

Based on these observations it was proposed that the strip was suffering from a mechanical defect leading to charge sharing[5]. In order to investigate the nature of this charge sharing and attempt to provide a software correction, a series of two dimensional matrices were produced which show the energy collected on DC11 against the sum of the energies collected on its neighbours, DC10 and DC12. These matrices were produced for a range of fold scenarios where between two and five DC strips contain real charge. For comparison purposes the same matrices have been incremented for strip DC05 and its neighbours DC04 and DC06 as these strips do not show evidence of charge sharing.

---

[5] This charge sharing results from a different mechanism than that presented in Section 6.2.1. It is believed that a mechanical fault on strip DC11 of the SmartPET1 detector results in poor capacitative coupling leading to the strip sharing charge with its neighbours.

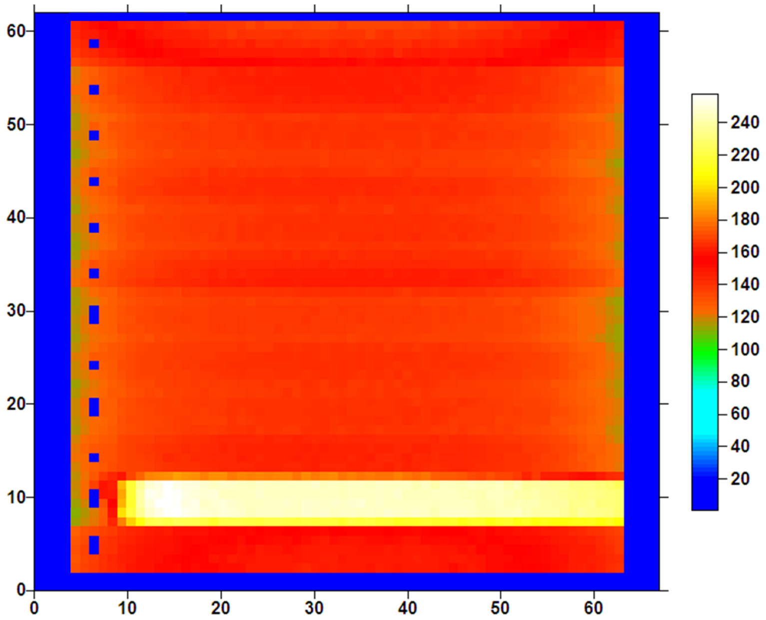

Figure 5.28: Mean DC T90 risetime (ns) as a function of collimator position (mm) from the ^{241}Am surface scan of the SmartPET1 detector where gamma rays were incident on the DC face. The mean risetime is calculated from all events depositing full energy in the detector. The detector generally exhibits a uniform response across all DC coupled strips with the exception of DC11 where the T90 value is consistently longer.

For events registering a fold three interaction, this matrix looks as shown in Figure 5.29(left). For comparison, the corresponding matrix for the non-charge sharing strips is shown in Figure 5.29(right). There are two distinct features in the left hand matrix. The diagonal line running from the top left to the bottom right of the plot corresponds to true Compton scattered 662keV gamma rays while the second region, running diagonally across the bottom of the image, is due to charge share events. For these events, the majority of charge is collected on DC11 with a small amount being shared with its neighbours. The gradient of this line indicates that this defect results in $\sim 2-3\%$ of the energy deposited in DC11 being shared with its neighbours. This is confirmed by the relative offset between the two photopeaks observed in uncorrected DC11 spectra. The ratio of counts in these two peaks also reveals that more than 80% of 662keV gamma rays which interact in DC11 result in charge sharing.

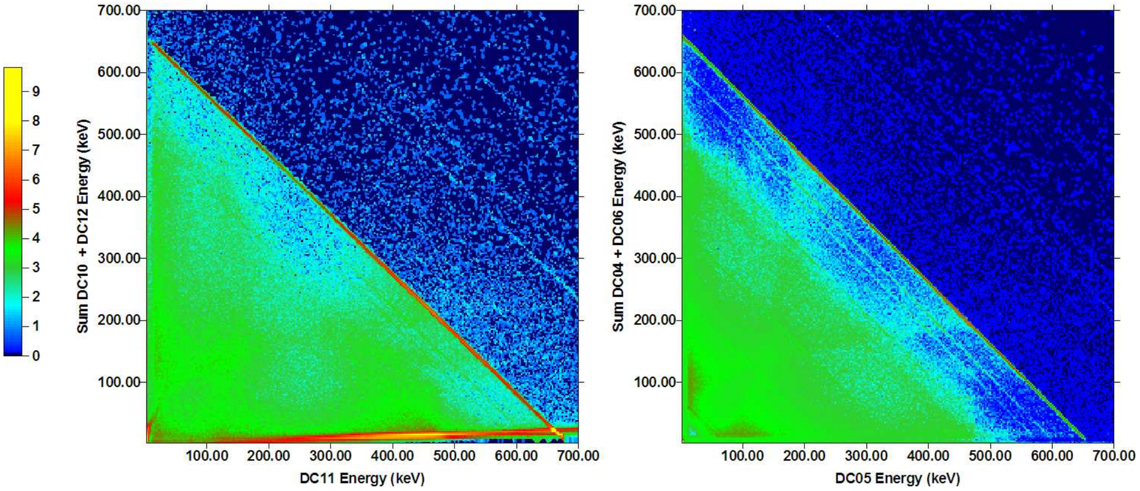

Figure 5.29: Left: A gamma-gamma matrix showing the energy deposited in DC11 against the sum of energy deposited in DC10 and DC12 for events registering fold three on the DC face of SmartPET1. The diagonal line running across the bottom of the plot corresponds to events where charge is shared between DC11 and its neighbours. Right: The same matrix for DC05 and its neighbours DC04 and DC06. No diagonal 'charge sharing' line is present. The matrices were produced by uniformly illuminating the DC face of the detector with a ^{137}Cs source and number the of counts in each matrix is displayed on a logarithmic scale.

In order to correct the double peaking observed for interactions in DC11, gates are applied to the charge sharing regions in the gamma-gamma matrices and the total energy added back to DC11 for events which fall within the two dimensional energy gates. This method results in the production of a correction spectrum which is shown in Figure 5.30(right). This approach ensures the photopeak efficiency of the SmartPET1 detector is maintained. The achievable energy resolution is degraded somewhat through the application of this algorithm with the FWHM of the corrected photopeak being around 3.5keV compared with 2.5keV at 662keV for a typical DC coupled strip. This peak broadening is expected to be due to the quadrature summing of electronic noise during the charge addback procedure.

The PSA techniques and DC11 charge sharing correction methodology discussed in this chapter form the basis of an algorithm for the processing of PET imaging data. These analysis techniques have been applied in the imaging of a number of point-like and distributed sources, the results of which are presented in subsequent chapters.

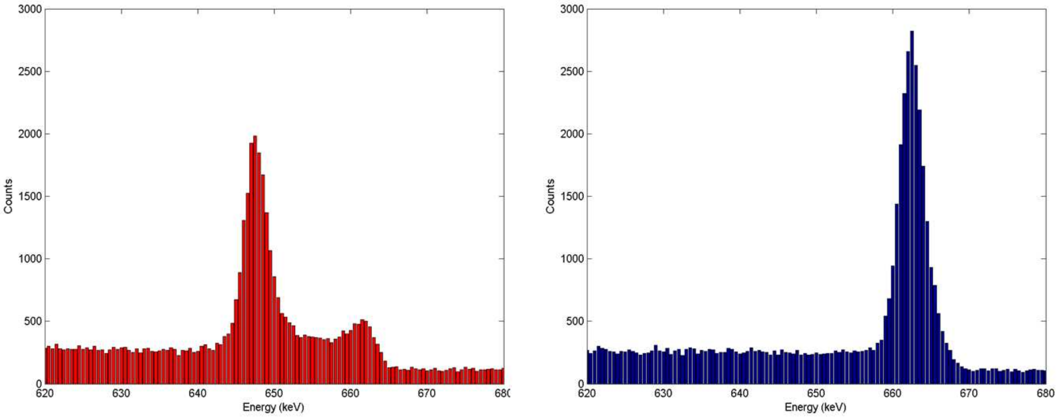

Figure 5.30: Gamma-ray spectra from strip DC11 on SmartPET1 with (right) and without (left) the application of charge sharing correction. The spectra show the ^{137}Cs photopeak before and after the correction has been made.

Chapter 6

PET Imaging With SmartPET

The imaging performance of the SmartPET system has been investigated by performing experimental measurements with both point-like and distributed sources. This section outlines the experimental details and discusses the data processing methodology employed in the application of parametric PSA techniques to event by event PET data.

6.1 Experimental Setup

The two SmartPET detectors were mounted in the rotating gantry as illustrated in Figure 6.1. The system was configured with the DC face of each detector facing inwards towards the source holder. This configuration is constrained by the design of the rotating gantry. As the DC coupled contacts are two orders of magnitude thicker than the AC contact the configuration may reduce the low energy efficiency of the system although the effect on performance is expected to be negligible when imaging with 511keV gamma rays. In the gantry 'home' position, the SmartPET1 detector is positioned above the source with SmartPET2 below. Each detector was positioned such that the DC coupled face was 65mm from the centre of the source holder, resulting in a detector-detector separation of 130mm.

6.1.1 Trigger Electronics

For all PET measurements, a coincident gamma-ray event between the two SmartPET detectors was required in order to trigger the data acquisition system. For each detector the output of the twelve AC coupled strips were processed by Ortec 863 Quad TFAs followed

Figure 6.1: The SmartPET detectors in the automated rotating gantry for data acquisition in PET mode. The structure between the two SmartPET detectors at the centre of the field of view is the gantry sample tray designed to house the source to be imaged.

by Ortec 935 CFDs configured with 20ns constant fraction delay and thresholds of around 60keV. The logical OR of each set of twelve AC coupled strips, generated using a Philips Scientific 785 Quad Logic Unit, was taken as a primary trigger from each SmartPET detector. These signals then formed the input to a LeCroy 380A Multiplicity Logic Unit providing a master trigger based on the logical AND of the two input signals. A circuit diagram of this trigger is shown in Figure 6.2.

The timing circuit was configured with a coincidence timing window of 100ns. It was decided that due to the relatively weak strength of the sources imaged, a window of this width would improve statistics without introducing too great an influence from random coincidences. Based on Equation 2.10 the random count rate is estimated to vary between 0.63cps for point source imaging and 350cps for phantom and pseudo-phantom imaging. These rates represent just 0.16% and 4.50% of the total coincidence count rate in these two cases.

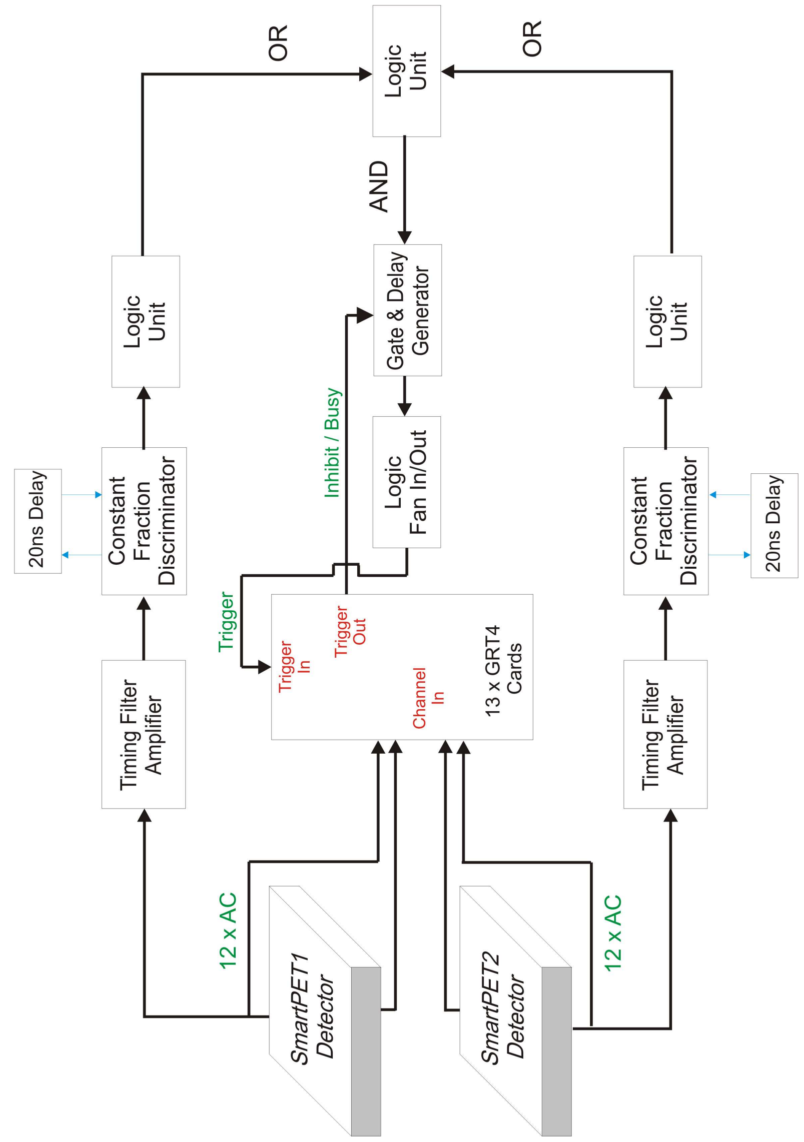

Figure 6.2: A circuit diagram of the trigger electronics employed in PET imaging measurements with the SmartPET system.

6.1.2 Point Source Imaging

Three ^{22}Na point sources were securely mounted into the gantry sample tray between the two SmartPET detectors. These point sources were positioned at different locations along the rotation axis and different r,ϕ coordinates relative to this axis. At the time of measurement these point sources labelled as NPRL319, NPRL361 and NPRL485, had activities of 0.0014MBq, 0.0037MBq and 0.0307MBq respectively. These point sources are shown in Figure 6.3(right) where their position relative to one another can be seen.

During data acquisition singles rates of ∼2.5kcps were recorded with each detector (equivalent to ∼0.2kcps per strip), resulting in a coincidence count rate of ∼400cps. Due to the limitations in the GRT4 cards (discussed in Chapter 4) the accepted count rate was limited to 220cps. In order to ensure sufficient statistics for image reconstruction, data were collected for four hours at each angular position, where the detectors were rotated in 5° steps between 0° and 175°. The choice of 5° angular increments was made based upon the trade off between adequate angular sampling and practical acquisition times.

6.1.3 Line Source imaging

A 0.9MBq ^{22}Na line source (3600Bq/μl) with dimensions of 50mm x 2.2mm internal diameter), shown in Figure 6.3, was imaged in two orientations relative to the system geometry. Data sets were recorded with the line source positioned parallel to the axis of rotation (the z-axis in Figure 6.9) with 0° and 45° elevation. As with the point source measurement, the SmartPET system was configured with a detector separation of 130mm. The singles count rate from each detector was 50kcps resulting in a coincidence trigger request rate of 8kcps, limited to 220cps accepted rate.

6.1.4 Pseudo-Phantom Imaging

A 'pseudo-phantom' was constructed using two ^{22}Na point sources (NPRL361 and NPRL485) and the ^{22}Na line source. The line source was positioned parallel to the rotation axis with point sources either side, creating a source distribution which contains some interesting features but without the complex structures present in the Jaszczak phantoms subsequently discussed.

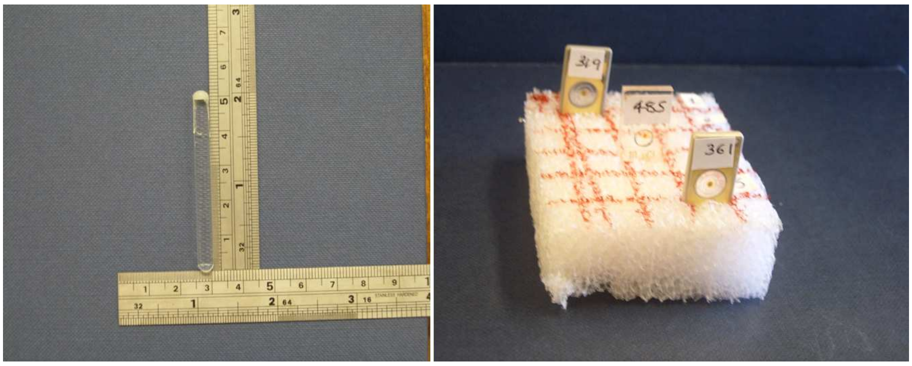

Figure 6.3: Left: The ^{22}Na linesource imaged with the SmartPET system. The line source is 50mm long with an internal diameter of ~2.5mm and activity 0.9MBq. Right: The three point sources which were imaged. The label on each source refers to the NPRL number identifying it.

6.1.5 Phantom Imaging

Two Micro Deluxe Flanged Jaszczak phantoms [JAS], pictured in Figure 6.4 were filled with 0.9MBq of liquid ^{22}Na. These phantoms each consist of a standard cylinder (5cm outside diameter) and a 'rod' insert consisting of six discrete regions of different diameter rods. These rods have diameter 1.2, 1.6, 2.4, 3.2, 4.0 and 4.8mm and length 3.3cm. One of the phantoms was in 'hot rod' configuration with the rods being filled with liquid ^{22}Na while the other is a 'cold rod' phantom, the main volume of the cylinder being filled while the rods remain empty. The 'hot' and 'cold' phantoms therefore have specific activity 570Bq/μl and 17Bq/μl respectively.

Each phantom was imaged individually with a coincident trigger request rate of 8kcps recorded and data collected for four hours per position over the angular range from 0° to 175°.

6.2 Data Processing

An important aspect of this work has been the development of data processing routines which when applied to event by event PET data will correct imperfections in detector performance and utilise PSA techniques to improve the achievable position resolution. With the introduction of the new digital electronics it is envisioned that these algorithms will be run in real time. It is for this reason that many of the approaches developed are based

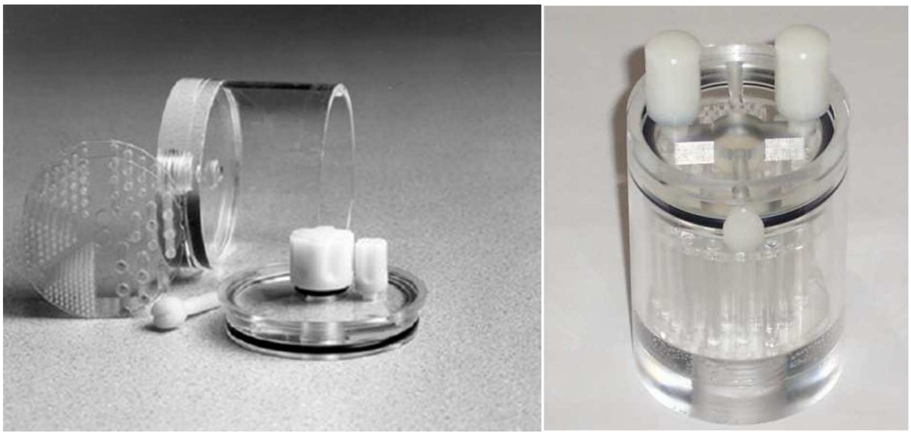

Figure 6.4: Pictures of a Micro Deluxe Flanged Jaszczak phantom. The image on the left shows the insert consisting of rods of various diameters.

on parameterisation of the detector response and as soon as is practicable data processing proceeds based on analysis of these parameters only. This data reduction is designed to avoid a bottle neck occurring in the case of online analysis. Figure 6.5 shows a schematic diagram of the data flow for both the current (GRT4) and the future (Lyrtech) DAQ systems both of which were discussed in Chapter 4. In each case the data processing chain has been partitioned into three stages. Stage A refers to the digitisation and energy calculation stage, stage B to the process of zero suppression (a data reduction technique discussed in Section 6.2.1) and stage C to the implementation of PSA algorithms and subsequent output of data to disc. Under the current conditions a bottle neck in data transfer occurs at the interface between stages A and B as data is written at a maximum rate of 4Mb/s, through a VME16 bus via an ethernet connection, from the VME crate housing the GRT4 cards. In the case of the Lyrtech electronics a Front Panel Data Port (FPDP) [Zhe02] readout will allow digitised trace data to be transfered from the cards at a maximum rate of 320Mb/s[1] alleviating the bottle neck encountered with the GRT4 system and allowing the SmartPET detectors to operate at a count rate of 50kHz per strip. Performing PSA online (implemented in FPGAs), thus removing the need to write out trace data, would then require a maximum data rate capability of 20Mb/s to disc via ethernet connection (assuming the output of the PSA algorithms take the form of parameter lists describing the

---

[1] Based on reading out 64 samples per trace from 100MHz, 14-bit FADCs [Laz06].

three-dimensional interaction position, energy and time of each interaction[2]). It therefore becomes clear that the use of fast PSA algorithms is essential if the goal of fully online data processing is to be realised. Thus, the techniques developed for the SmartPET system aim to provide improved spatial resolution on an event by event basis through the use of relatively simple, computationally inexpensive approaches. Consequently the accuracy is not expected to be the same as that which may be provided by more advanced PSA algorithms such as the Adaptive Grid Search [Rad04] and Singular Value Decomposition [Ola06] [Dox07] approaches under development for the Advanced Gamma Tracking Array (AGATA) [Baz04] and Gamma Ray Energy Tracking Array (GRETA) [Del99] projects. The methods developed within this work ultimately being influenced by both the complexity of the event and the assumptions upon which they are based.

Parametric approaches to PSA are ideally suited to imaging applications as the statistical nature of the problem allows for uncertainties in the calculation of interaction position to exist while still maintaining image quality. Indeed, as part of the future development of the SmartPET system one could consider modelling such uncertainties into the system matrix of an iterative reconstruction algorithm. One recent example of such an approach is the High Definition (HD) PET system [SIE] which compensates for the inherent lack of depth of interaction sensitivity in a commercial scanner by modelling the detector response in the reconstruction algorithm [Jon07]. This removes the induced image blurring providing diagnostic images of higher quality than was previously attainable.

6.2.1 Online Geometric Zero Suppression

In all data recorded a technique known as geometric zero suppression was employed online. This technique reduces the data storage requirements (and processing time for offline analysis) by retaining only those pulse shapes which are deemed useful for PET analysis. In order to do this each pulse shape is examined and those identified as having net charge above a specified lower limit (three standard deviations of the baseline noise as discussed in Section 5.2) are flagged. These pulse shapes are then kept along with those in the two adjacent channels which will contain image charge pulse shapes required to refine the lat-

---

[2] This calculation is based upon the output from coincident single pixel hits where one parameter list exists per detector face [Laz06].

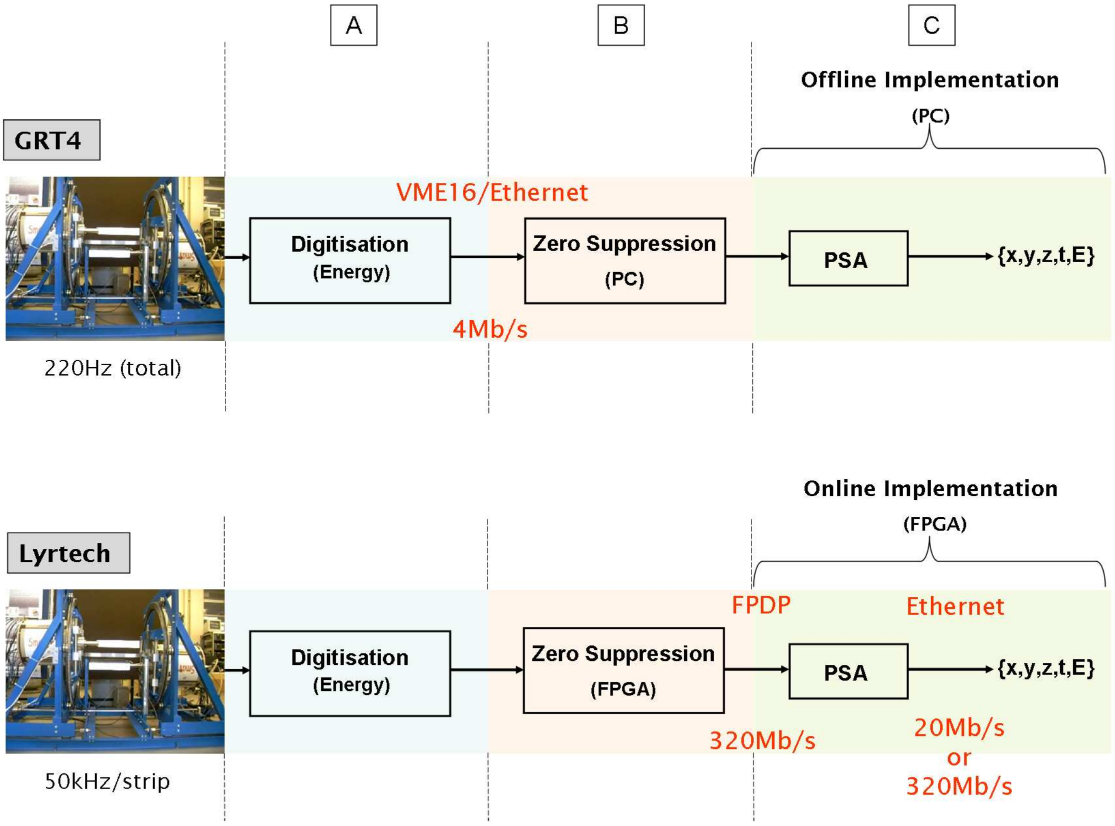

Figure 6.5: Diagram showing data flow with the GRT4 system (top) and the new Lyrtech electronics (bottom). The diagram shows how the bottle neck in data transfer currently occurs at the point at which the data is read from the GRT4 cards to disc in the form of digitised traces. In the case of the new electronics this will be alleviated by performing PSA online and writing parameter lists (which requires a rate of only 20Mb/s) to disc.

eral interaction position. Once every channel has been analysed, any strip not identified as containing a real charge, image charge or some convolution of the two is removed from the data stream prior to output to disc. It is found that this technique reduces the data size by around 25% while maintaining the number of events recorded.

6.2.2 Event Selection

In the first stage of offline analysis events are filtered based on the total energy deposited in each of the SmartPET detectors. As little or no scattering is likely to occur prior to gamma rays being incident on the detectors, no photopeak gate is applied. However, as

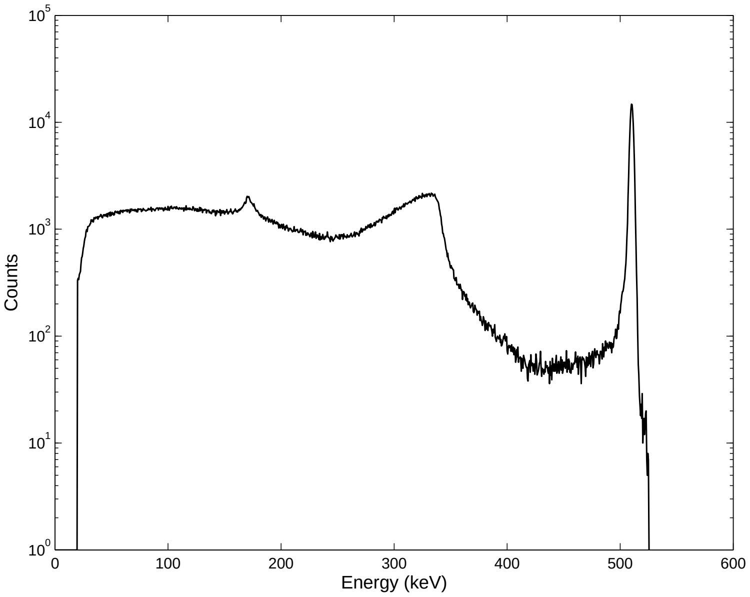

Figure 6.6: ^{22}Na Gamma-ray spectrum from a typical SmartPET strip following event selection based on energy deposition. A high energy threshold has been applied to reject events where the total energy deposited in one SmartPET detector is greater than 520keV while a low energy threshold of 20keV is also in place. In this spectrum a logarithmic scale is applied to the y-axis.

^{22}Na decays through the emission of a characteristic 1275keV gamma ray a high energy threshold is applied at 520keV limiting the impact of coincidences not originating from 511keV gamma rays. This approach maximises the imaging efficiency while minimising the influence of random coincidence events. In addition, a low energy threshold of 20keV is also applied. A typical gamma-ray spectrum from one of the SmartPET channels after the application of this filtering procedure is shown in Figure 6.6.

6.2.3 Application of DC11 Charge Sharing Correction Algorithm

For all events depositing energy in strip DC11 of SmartPET1, the energy of this strip is compared with the energy of its neighbours (according to the method discussed in Chapter 5) to determine if charge sharing has taken place. If charge sharing has taken place between DC11 and a single neighbour strip then the energy lost from DC11 is added back and the fold of the event is corrected accordingly. In the case of charge being observed in DC10, DC11 and DC12 the event is deemed to be unsuitable for further analysis with PSA and is vetoed.

6.2.4 Application of Parametric Pulse Shape Analysis

The PSA techniques developed through detector characterisation measurements and discussed in Chapter 5 have been applied to the PET data recorded with the SmartPET system. The precise implementation of the PSA algorithms depends upon the complexity of the gamma-ray interaction. In this work events are considered in which each face records real charge in either one or two strips. This section describes the methodology for handling each of these categories.

1. Fold One Events

For events where only one strip on each face of the two detectors records real charge, the lateral interaction position within each strip is calculated from the area of the image charges in neighbouring strips. The image charge asymmetry value is calculated according to Equation 3.19 and compared with the coefficients generated from the calibration discussed in Chapter 5. This yields the gamma-ray interaction position in the x-y plane for each detector. The depth of interaction is not calculated for fold one events as the reconstruction algorithm, discussed in a subsequent section, does not require the application of a correction for parallax error. As gamma rays interacting in edge strips result in the generation of only one image charge from which to calculate the interaction position, the technique discussed in Chapter 5 is applied.

2. Fold Two Events

Previous to this work, it has only been possible to image from single pixel hits using the SmartPET system. Here, steps have been taken to use the parametric PSA approaches developed in an attempt to include larger event data fractions in the reconstruction data set. In order to do this, fold two events have been dealt with in a number of ways depending on the complexity of the interaction.

In the case of a fold two interaction being recorded on any face of either detector, the depth of each interaction is calculated by comparing the T30-T90 value to the two-dimensional gates calculated during the calibration. For PET imaging, only the location of the first interaction is required. The first hit is therefore identified based on the depth of interaction. According to the Klein-Nishina distribution (Figure 3.3) it is likely that, at 511keV, a gamma ray will undergo forward scattering through the depth profile of the detector. As such, the first hit is defined as being the shallowest of the two. In addition, a further constraint is applied which ensures that this interaction must also be that which deposits the most energy. This energy constraint is required in order to allow the parametric PSA algorithms to be applied. By demanding that the first hit deposit the most energy, the influence of the second interaction on the image charges associated with the first interaction may be minimised. Monte Carlo simulations of the SmartPET system performed using the GEANT4 framework [GEA] and presented in [Mat04] show that this assumption is correct for around 70% of events. The result of a similar simulation for the closed end coaxial TIGRE (Tracking the Interaction of Gamma Ray Events) HPGe detector is reproduced from [Des05a] in Figure 6.7. In interpreting this plot one must consider that all full energy events are included, irrespective of the number of interactions the gamma ray has undergone within the crystal. At low energy it may be observed that for most events the first interaction deposits the most energy as photoelectric absorption is the dominant interaction mechanism. As the energy increases the probability of the first interaction depositing the largest fraction of energy decreases as the number of interactions required for complete absorption becomes larger. A minimum occurs for gamma rays around 500keV and above this the probabilty rises again as only those gamma rays depsoiting a large fraction of their energy in the first interaction contribute to a full energy event. The discrepency between the fraction of 511keV events in which the first interaction deposits the most energy quoted in [Mat04] and that presented in Figure 6.7 may be explained by the difference in geometry between the SmartPET HPGe detectors and the TIGRE detector. The smaller active volume of the SmartPET detectors leads to the minimum in the distribution occuring at 250keV (∼45% of events depositing the majority of their energy in the first interaction) before rising up again towards 511keV.

Following the definition of the first hit, analysis of fold two events in the SmartPET detectors proceeds as follows:

- The interaction defined as being the first hit is processed with the lateral interaction position being calculated through image charge analysis approaches. If the two interactions are separated by two or more strips (e.g. AC06 and AC09) then the influence of the second hit on the image charges neighbouring the ‘first’ interaction is assumed

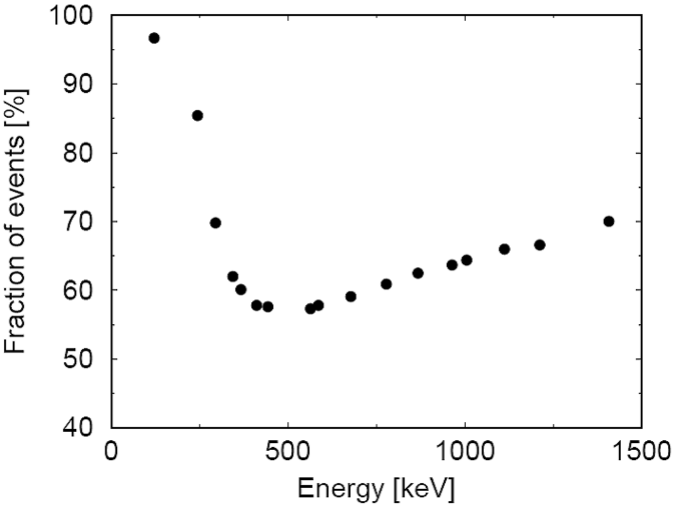

Figure 6.7: Fraction of full energy events where the first interaction deposits the most energy for a range of initial gamma-ray energies. This result, reproduced from [Des05a] is from a Monte Carlo simulation of the TIGRE detector.

to be negligible. The lateral interaction position is therefore calculated using the standard image charge asymmetry approach.

- For events where the two hits are separated by less than two strips then it is assumed that the presence of a convolved image charge to one side of the 'first' interaction prevents the use of the conventional image charge asymmetry technique. Instead the single 'useable' image charge on the other side of the hit strip is analysed in the same way as if the interaction was in an edge strip according to Equation 5.1.

6.2.5 Event Categorisation

In order to apply the parametric PSA techniques a number of assumptions have been made. It is clear that the validity of these assumptions will vary depending upon event type. For example, coincident single pixel events provide the highest quality data in terms of applying image charge asymmetry calculations. As the complexity of the gamma-ray interaction increases and the number of strips containing real charge becomes larger, the ability to accurately identify the interaction position is expected to decrease. Thus, it is useful to categorise gamma-ray events according to their perceived quality. In analysis of the point source data set events were grouped according to their fold with the convention [SP1 AC

Event Type	Fraction of Events (%)
1	19.30 (0.01)
2	16.54 (0.01)
3	24.55 (0.01)

Table 6.1: Breakdown of event types from the point source data set once the energy selection criteria has been applied. The uncertainty associated with each value is shown in brackets.

fold, SP1 DC fold, SP2 AC fold, SP2 DC fold] being employed. Using this labelling scheme the highest quality events (coincident single pixel hits) are defined as [1,1,1,1] because only one strip on each face of each detector records real charge. In this analysis all events from [1,1,1,1] up to and including [2,2,2,2] were considered. Table 6.1 shows a break down of the fraction of events falling into each category during the point source measurement. The three event types used during the analysis are:

1. : [1,1,1,1] events
2. : Any event where fold 2 is recorded on a single face (e.g. [1,1,1,2] events)
3. : Any event where fold 2 is recorded on more than one face (e.g. [1,1,2,2] events)

It has been shown by [Mat06] that Type 1 events can be successfully used to image point sources. It is clear from Table 6.1 however that the imaging sensitivity will be severely limited by including only these events in the imaging data set. By including all events up to and including [2,2,2,2] a factor of 3 increase in sensitivity is theoretically achievable. The remaining (∼ 40%) of events fall into the category of having at least one detector face recording a fold greater than two. The vast majority of these events record fold three interactions.

Fold Two Events

Of the event types discussed in the previous section it is the processing of fold two events which have the potential to be problematic for the parametric PSA techniques developed in this work. In the case of a fold two interaction being recorded on the face of one of

Strip Separation	Fraction of Events (%)
0	69.47 (0.25)
1	16.63 (0.10)
2	5.87 (0.06)
3	2.35 (0.04)
4	1.46 (0.03)
5	1.14 (0.02)
6	0.93 (0.02)

Table 6.2: Fraction of fold two gamma-ray events as a function of strip separation. The uncertainty associated with each value is shown in brackets.

the SmartPET detectors, it may be necessary to calculate the lateral interaction position through analysis of a single image charge in the manner outlined above. Assuming the interaction sequence is correctly identified then this image charge will be in the strip neigbouring the strip in which the first hit took place. The influence of the signal induced by the second hit on the shape of this single image charge will decrease as the separation between hits one and two increases. As a result it is expected that the position determination will become increasingly inaccurate as the distance between interactions decreases. As a scattering distance of several strips is much less probable than a scatter into an adjacent strip, the processing of these event types may place a fundamental limit on the spatial resolution and quality of the final image. This is highlighted in Table 6.2 and Figure 6.8 which shows how the fraction of fold two events recorded on the AC face of SmartPET 1 quickly falls away as a function of separation.

The trend exhibited by Figure 6.8 is consistent with the exponential distribution associated with the attenuation of gamma rays (see Section 3.3.1). One observes how scattering between adjacent strips is the most probable scenario. This is explained by a combination of effects arising as a consequence of Compton kinematics:

- The forward focussed scattering profile at 511keV (Figure 3.3) suggests that scattering angles which permit the crossing of more than one strip boundary are unlikely to occur.
- Those gamma rays scattering through relatively large angles such that several strip

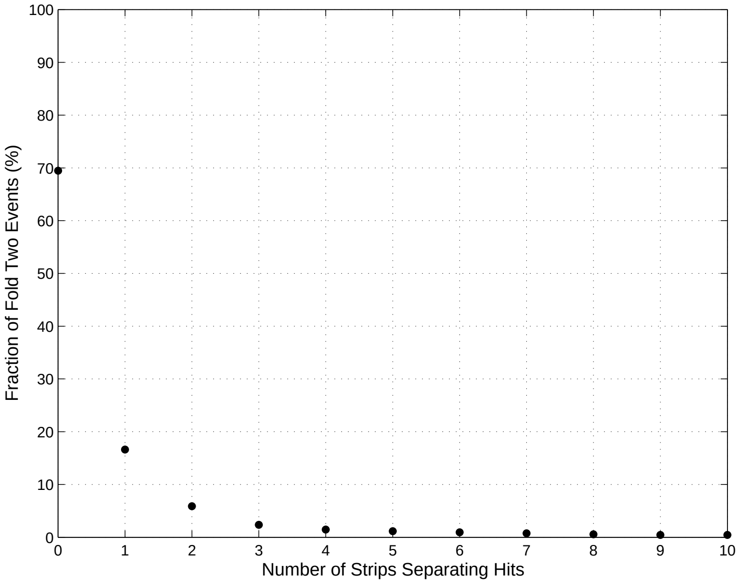

Figure 6.8: The fraction of fold two gamma-ray events as a function of the number of strips separating hits.

boundaries may potentially be crossed must deposit significant fractions of their incident energy in the first interaction (a 511keV gamma ray scattering through 90° deposits 255.5keV). The energy of the scattered gamma ray, and thus its mean free path [Kno99], is therefore sufficiently low as to minimise the probability that it will traverse several strips before full energy absorption occurs.

Ideally, a quantitative investigation should be performed into the impact of scatter distance on image quality. In the data sets presented here however, it was found that insufficient statistics exist for such an analysis to be reliably performed.

It is expected that as Type 2 events contain only one fold two interaction the impact on the degradation of image quality may be small. It is the Type 3 interaction however which may place a limit on the usefulness of simple PSA techniques. In the longer term, the development of more complex PSA algorithms will, in principle, allow all events to be processed with relative ease. In order to do this pulse shape decomposition algorithms will be required. These algorithms must decompose the pulse shapes resulting from two main interaction scenarios;

1. Gamma rays scattering between adjacent strips requiring the decomposition of convolved real and image charge

2. Scattering between non-adjacent strips requiring the decomposition of convolved image charge.

6.3 Image Reconstruction

During data acquisition the SmartPET system records all coincident events occurring between the two detectors. Each pixel-pixel combination defines a LoR which, in principle, could be used to reconstruct the source distribution. In this study however, a subset of all the possible LoRs are used due to limitations of the image reconstruction algorithms. In this work, only LoRs which are defined between directly opposite pixels (parallel LoRs) are included in the sinograms. These LoRs which are equally separated in both sinogram dimensions, (r,ϑ), cover the entire field of view and are therefore entirely adequate to reconstruct images from. However they represent only a small fraction (<1%) of all useable LoRs reducing the effective imaging sensitivity of the system. So long as sufficient statistics are collected at each LoR the impact on image quality is expected to be negligible.

To compensate in some way for this reduction in imaging sensitivity, a technique to provide additional elements in the sinogram is employed. This technique uses LoRs which connect opposite-but-one pixels and places the extra data point in a bin equally spaced between the two parallel LoRs. As the detector separation is large compared to the detector element spacing, these additional LoRs may be considered to also be parallel. In this way, an increase of $2(N\text{-}1)$ samples is achieved using ‘almost parallel’ LoRs. Upgrading the image reconstruction algorithms in order to use more LoRs is ongoing and should be considered an essential requirement for future development of the SmartPET system.

6.3.1 2.5D Image Reconstruction

Image reconstruction for the SmartPET system is handled in terms of discrete two-dimensional ‘slices’ through the rotation axis of the system (Figure 6.9). The twelve AC coupled strips of the SmartPET detectors run perpendicular to the rotation axis and can therefore be used to define these twelve slices. However, applying the ‘almost parallel’ LoR technique in the rotation axis increases the number of slices from twelve to twenty three. An individual sinogram is built for each of these slices where the x-axis contains the detector element and

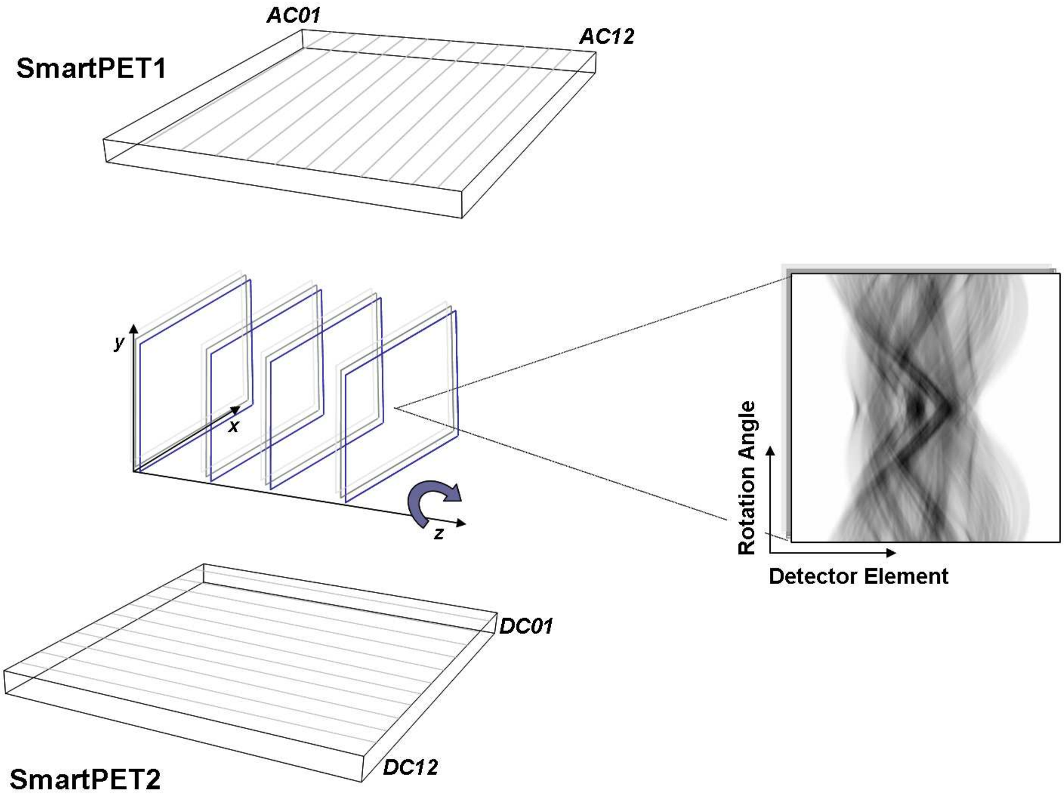

Figure 6.9: A schematic diagram of the experimental set up. Images are reconstructed from individual slices through the rotation axis (z-axis). For each sinogram the x-axis contains the detector element defined by the DC hit position while the AC strips define the slices. Parallel LoRs are defined between directly opposite pixels where the DC detector element is the same for both SmartPET1 and SmartPET2.

the y-axis the rotation angle of the system. Each sinogram may then be reconstructed, the combination of all slices providing a so called 2.5D (multislice) reconstruction.

6.3.2 The FBP and MLEM Algorithms

The image reconstruction algorithms employed in this work were developed specifically for the SmartPET project. Details of these algorithms, including a user guide for the FBP software, can be found in [Mat06]. All images presented in this work have been reconstructed onto a 256^2 uniform pixel grid representing an area of 60mm x 60mm with ramp filtering and linear interpolation applied in all FBP images. As the grid must have dimensions which are a power of two (due to software considerations) a grid size of 256^2 pixels was chosen so as to maintain spatial resolution while ensuring analysis procedures remained computationally efficient.

6.4 Image Quality Assessment

The assessment of image quality may be considered to be extremely subjective [Wan02] and as such no definitive single metric exists. Instead, a range of techniques which aim to measure the quality of an image in terms of characteristics such as noise, contrast or spatial resolution are employed. In reality, the relative importance of these image properties will vary depending upon the scenario in which the image is being used.

In this work, the quality of the images produced is taken to be indicative of the performance of both the data processing techniques and the system as a whole. The image quality is therefore judged using measures of the Peak Signal to Noise Ratio (PSNR) and the spatial resolution as improvement (degradation) in these two metrics is closely related to improvement (degradation) in system performance.

6.4.1 Assessment of Spatial Resolution

In all point source images the spatial resolution is defined in terms of the FWHM of the reconstructed point source profile. Such a measure is often referred to as the Point Spread Function (PSF) [Val03]. In the case of line source imaging the Line Spread Function (LSF) is measured as the FWHM across a slices (or slices) through the image of the line source.

6.4.2 Assessment of PSNR

The Peak Signal to Noise Ratio is a measure of the ratio between the maximum possible power of a signal and the power of corrupting noise that affects it. Commonly, the PSNR is used to evaluate the quality of reconstruction of an image which has undergone compression but may easily be applied to images reconstructed from PET data.

The PSNR is defined in terms of the Mean Squared Error (MSE) between two images I and K with dimensions (M,N) as

$$MSE = \frac{1}{MN} \sum_{i=0}^{M-1} \sum_{j=0}^{N-1} (I(i,j) - K(i,j))^2 \tag{6.1}$$

where one image is considered to be a noisy approximation of the other. The PSNR (dB) is then defined as

$$PSNR = 20 \log_{10} \left(\frac{255}{\sqrt{MSE}} \right). \tag{6.2}$$

The PSNR value is of use only when used as a means of comparison between two images. To that end, in all PSNR analysis presented in this work, reconstructed images are compared with a base image of a 256^2 pixel grid where each element is equal to unity. In this way quantitative comparisons may be drawn between individual PET images.

Chapter 7

Imaging Results

7.1 Point Source Imaging

The first data set reconstructed from the SmartPET system was that of three ^{22}Na point sources. After separating the events into the three categories discussed in the previous chapter, images were reconstructed for each event type in turn from the individual two-dimensional slices through the rotation axis of the system. For each data subset the image quality was assessed in terms of spatial resolution and Peak Signal to Noise Ratio. Following individual analysis of the subsets, images were reconstructed using all data up to and including [2,2,2,2] events.

7.1.1 Type One Events

For all Type 1 ([1,1,1,1]) events, FBP images were reconstructed. Figure 7.1 shows all twentythree two-dimensional slices revealing the location of the three ^{22}Na point sources. Each image is individually scaled and a consistent linear colour map applied. In these data, point sources can be seen in slices 5,6,13,14,21 and 22 with each point source appearing in two discrete slices. The appearance of a point source in multiple slices is explained by geometric considerations when using 'almost parallel' LoRs with it being possible for a point source to be measured in three slices. This is explained diagramatically in Figure 7.2 where possible 'almost parallel' LoRs are defined for a source positioned between two detector

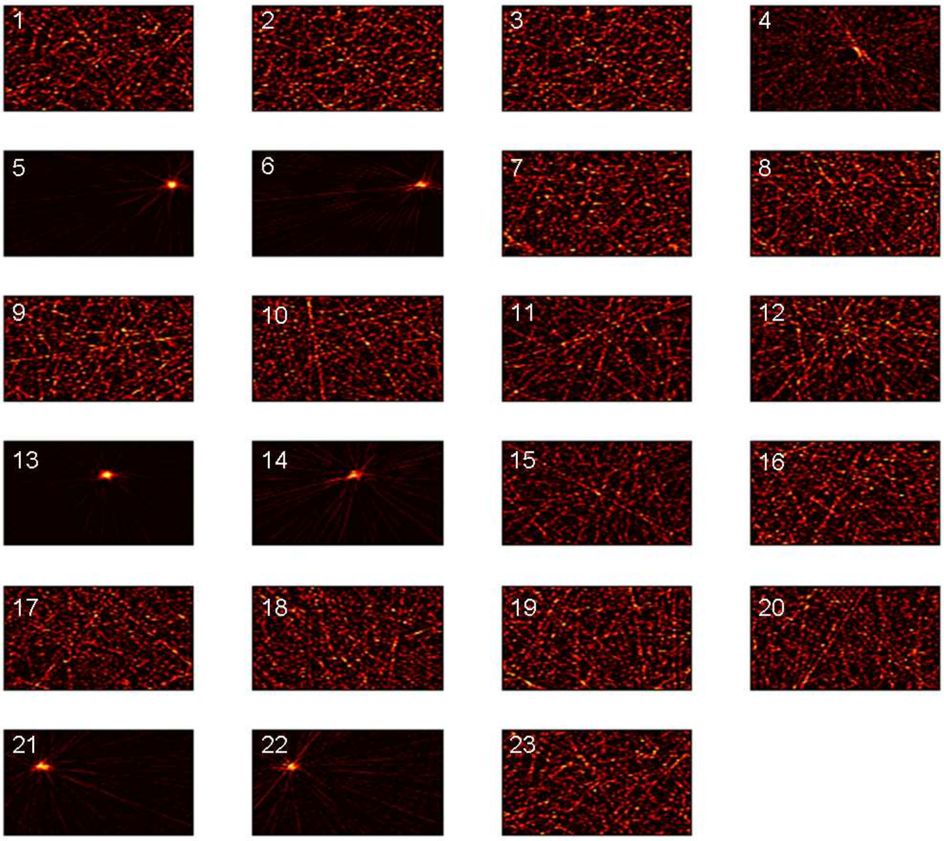

Figure 7.1: FBP reconstructed images of three ^{22}Na point sources using only Type 1 ([1,1,1,1]) events. The figure shows the image reconstructed from each of twenty-three discrete two-dimensional slices through the rotation axis of the SmartPET system where the slice number is displayed in the top left corner of each image. Each image is individually scaled and a consistent linear colour map applied.

elements. It can be seen how, depending upon the source location it is possible for LoRs to be measured in either two or three slices.

From the images presented in Figure 7.1 the strong source appears in slices 5 and 6, the weak source in slices 21 and 22 and the intermediate source in slices 13 and 14. Therefore, only these slices were considered in subsequent analysis of the point source data set. The FBP images reconstructed from these six slices are displayed in Figure 7.3 along with an assessment of the image quality, tabulated in Table 7.1. The FWHM is calculated for slices through the x and y axes along with the resulting mean value. Each image is reconstructed

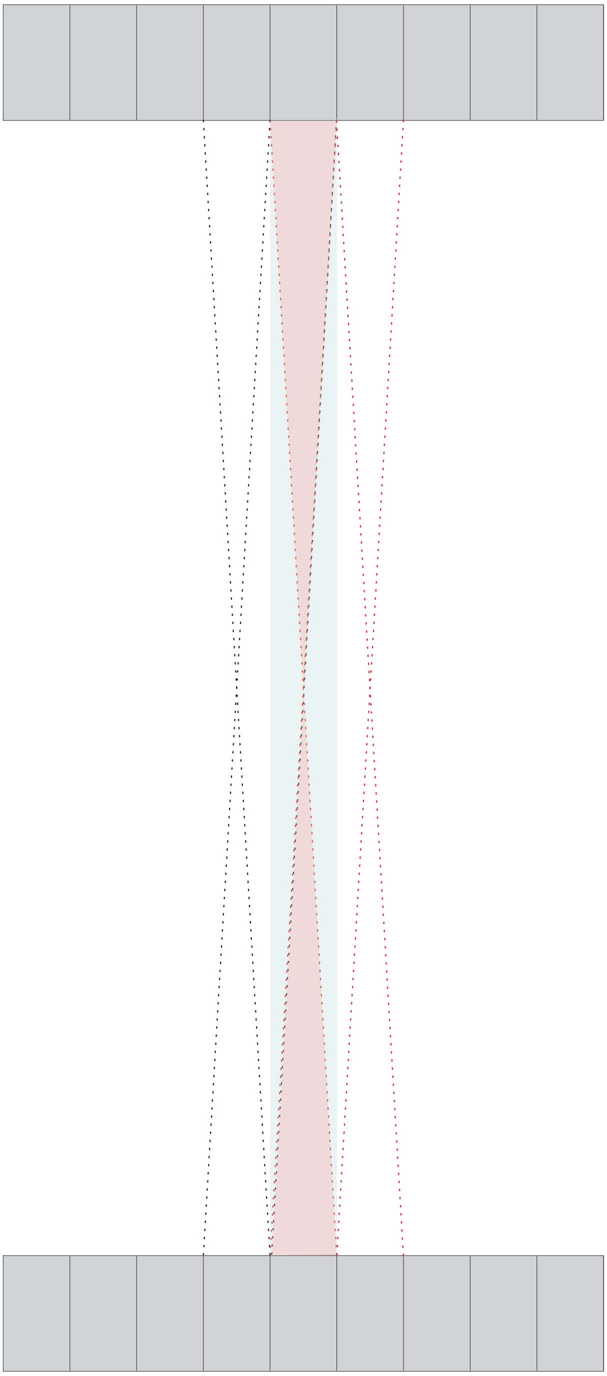

Figure 7.2: Diagram explaining the appearance of a point source in two or three image slices where the ‘almost parallel’ LoRs are shown by broken black and red lines. For a region covered by a single parallel LoR, the turquoise region highlights areas covered by two sinogram slices while purple regions are covered by three slices.

Slice	PSNR(dB)	FWHM$_x$ (mm)	FWHM$_y$ (mm)	FWHM$_{mean}$ (mm)
5	12.15	2.34(0.17)	3.40(0.17)	2.87(0.12)
6	10.56	3.28(0.17)	1.76(0.17)	2.52(0.12)
13	16.37	3.05(0.17)	2.90(0.17)	2.98(0.12)
14	1.09	2.58(0.17)	1.52(0.17)	2.05(0.12)
21	8.24	3.75(0.17)	2.81(0.17)	3.28(0.12)
22	1.21	1.64(0.17)	2.70(0.17)	2.17(0.12)

Table 7.1: Summary of results for the quality assessment of the six images presented in Figure 7.3.

into a 256 x 256 pixel grid with dimensions 60 x 60 mm corresponding to the field of view of the SmartPET system. Due to a variation in the number of counts present, each image has been independently scaled and a consistent linear colour map applied.

Each slice shows the presence of a point source, well localised within the field of view, with a FWHM of the PSF ranging from 2 to 3.5mm. The star like artefacts which are clearly present in each image are an affect associated with the use of FBP reconstruction and may be minimised through increased angular sampling. Slices 5,13 and 21 contain the most intense representations of each point source with the neighbouring slices containing consistently fewer counts. The effect of decreased statistics on the quality of the resulting images may be observed qualitatively in terms of the relative impact of the star artefacts and quantitatively in terms of the reduced PSNR values measured for slices 6,14 and 22. Due to the limited number of counts in the peak, the PSF profile of these slices is often extremely asymmetric, resulting in FWHM values inconsistent with other slices. In Table 7.1, values less than 2mm are a result of this. The uncertainty associated with each value of spatial resolution is the uncertainty resulting from the calculation of FWHM. Statistical uncertainties related to the number of counts in a given point source profile are not accounted for.

Achievable Spatial Resolution

In Chapter 2 the factors limiting the spatial resolution achievable in a PET image were discussed. In [Mos93] Moses and Derenzo define the FWHM (mm) of a reconstructed point source profile, Γ, to be

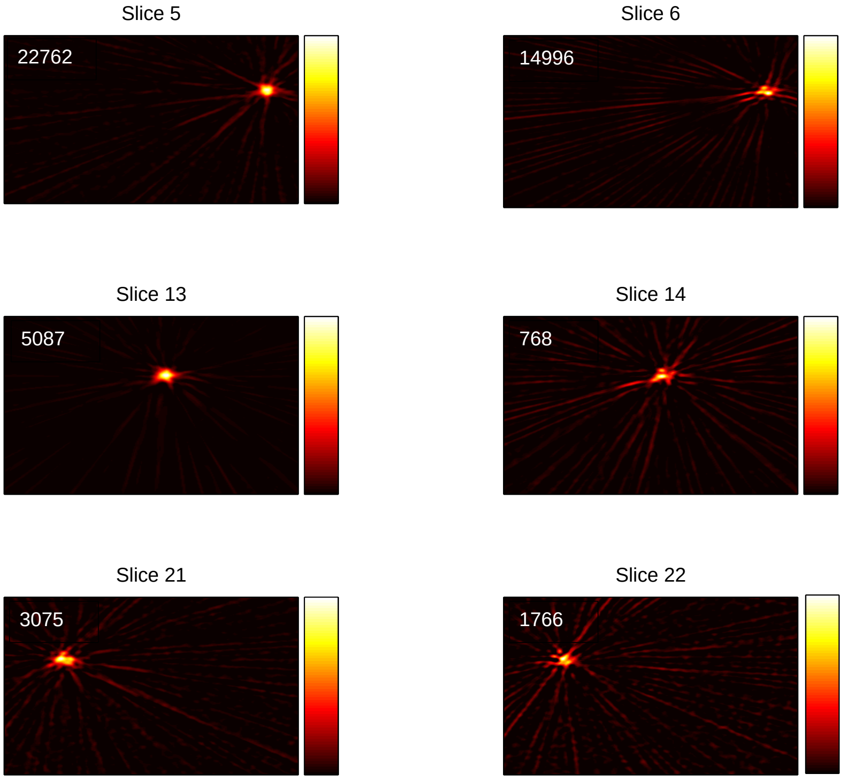

Figure 7.3: Images reconstructed from the six slices containing activity. The intermediate strength ^{22}Na source appears in slices 5 and 6, the strong source in slices 13 and 14 and the weakest source in slices 21 and 22. The number of counts in each reconstruction is displayed in the top left hand corner of each image. The star like artefacts associated with the use of FBP reconstruction appear more significant in the images on the right hand side. This results from the reduced signal to noise ratio of these images.

$$\Gamma = 1.25\sqrt{(d/2)^2 + (0.0022D)^2 + s^2} \tag{7.1}$$

where d is the crystal width, D is the detector-detector distance, s is the effective source size (taking into account positron range blurring effects) and the factor 1.25 is due to reconstruction.

For point source imaging with the SmartPET system, the detector separation was 130mm and the effective source size is ~1mm based on a positron range of 0.5mm [Der88]. Taking the crystal size, d, as 1mm (the effective size of a detector element when using PSA) a value of $\Gamma = 1.44$mm is calculated. The blurring factor associated with image reconstruction quoted above is defined empirically for iterative reconstruction. As the images presented in Figure 7.3 have been reconstructed using the FBP algorithm, the blurring factor is likely to be significantly larger. The values of PSF presented in Table 7.1 suggest that the blurring factor associated with FBP is around twice that quoted for iterative reconstruction. This is confirmed by the results of iterative reconstruction presented later in this study.

Anomalous Number of Counts

In the images presented in Figure 7.3 it is observed that a greater number of counts are included in the image of the intermediate strength source in slice 5 relative to the strong source in slice 13. As this may be indicative of non-uniformity in response, analysis was performed on data from a single ^{22}Na point source placed at the centre of the field of view. Figure 7.4(left) shows how the number of coincidences resulting from 511kev gamma rays recorded varies as a function of slice number (indexed by AC strip number). It can be seen how the sensitivity drops towards a minimum at slice 7 before rising again towards slice 11 which recorded the largest number of counts. This result was confirmed using the ^{22}Na line source spanning all slices. In clinical PET studies geometrical and efficiency correction factors (referred to as normalisation coefficients) are routinely applied in order to allow quantitatively accurate studies to be performed [Kin96]. Figure 7.4(right) shows the correction factor required to normalise the number of counts in each slice to that recorded in slice 11. This non-uniformity of response is unexpected in the SmartPET system and may be due to too high a threshold being set in the CFD of one or more channels. Further investigation into the variation of response throughout the entire FOV is required as part of the continued development of the SmartPET project. Several methods which are employed in clinical scintillator PET systems are discussed in [Bad98].

Normalisation coefficients generated for clinical PET systems are calculated and applied on a LoR by LoR basis during data processing. As this is not possible here the correction factors displayed in Figure 7.4(right) are not applied in any subsequent analysis. In the future, an evaluation of the uniformity of response of the SmartPET system across the entire field of view should be carried out. If correction factors must subsequently be applied the response of all LoRs relative to one another must be quantified and any discrepancies accounted for.

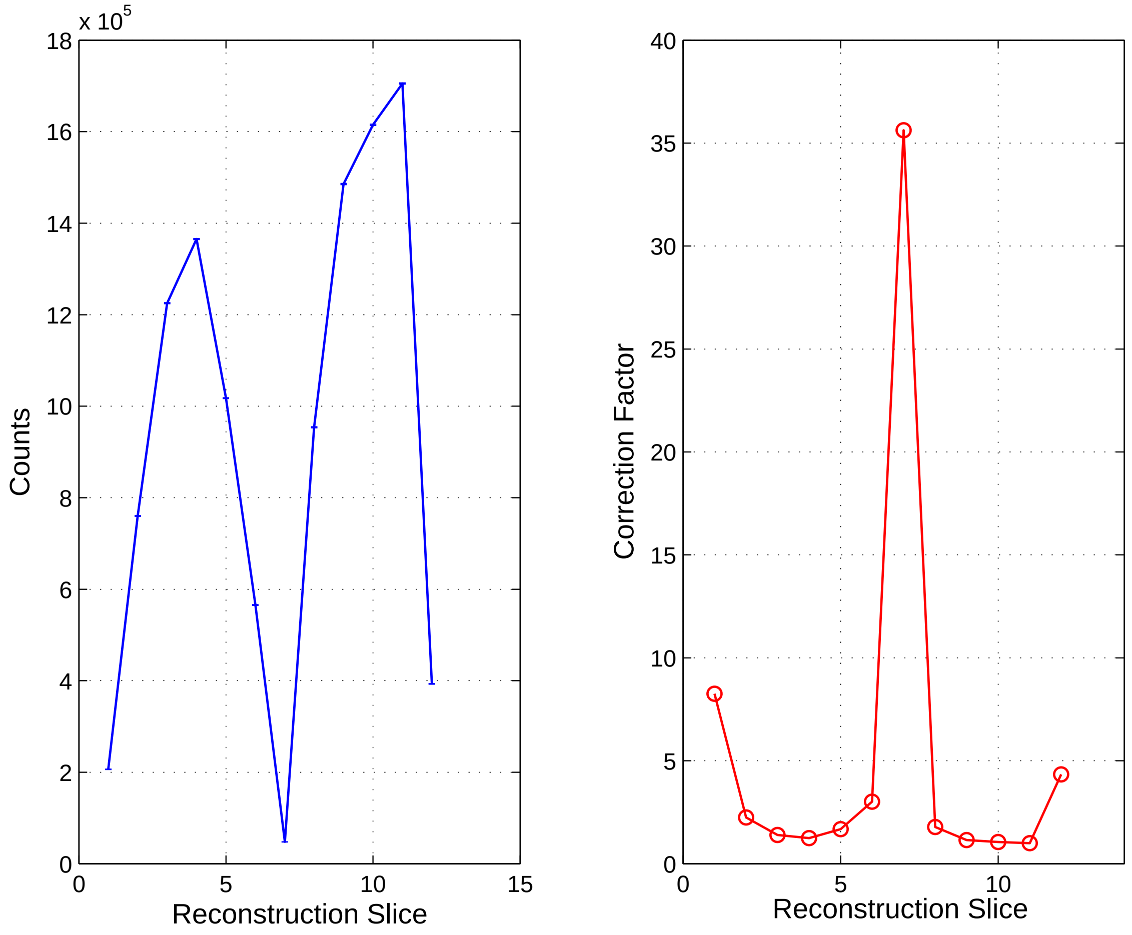

Figure 7.4: Left: Plot showing the variation in number of coincidences from a centrally located ^{22}Na point source recorded as a function of twelve reconstruction slices. Right: The correction coefficients required to normalise the response of each slice to that of slice 11.

Influence of Statistics on Image Quality

The effect of statistics on image quality has been investigated by performing reconstructions of the strong point source in slice 13 while varying the number of counts included in the images. Images were reconstructed from Type 1 events with 5, 10, 20, 50, 80, 100 and 120 counts included per angle (four representative results are shown in Figure 7.5). The PSNR and PSF values were calculated for each image and the variation of each metric as a function of the number of events is displayed in Figure 7.5. This figure also shows one-dimensional

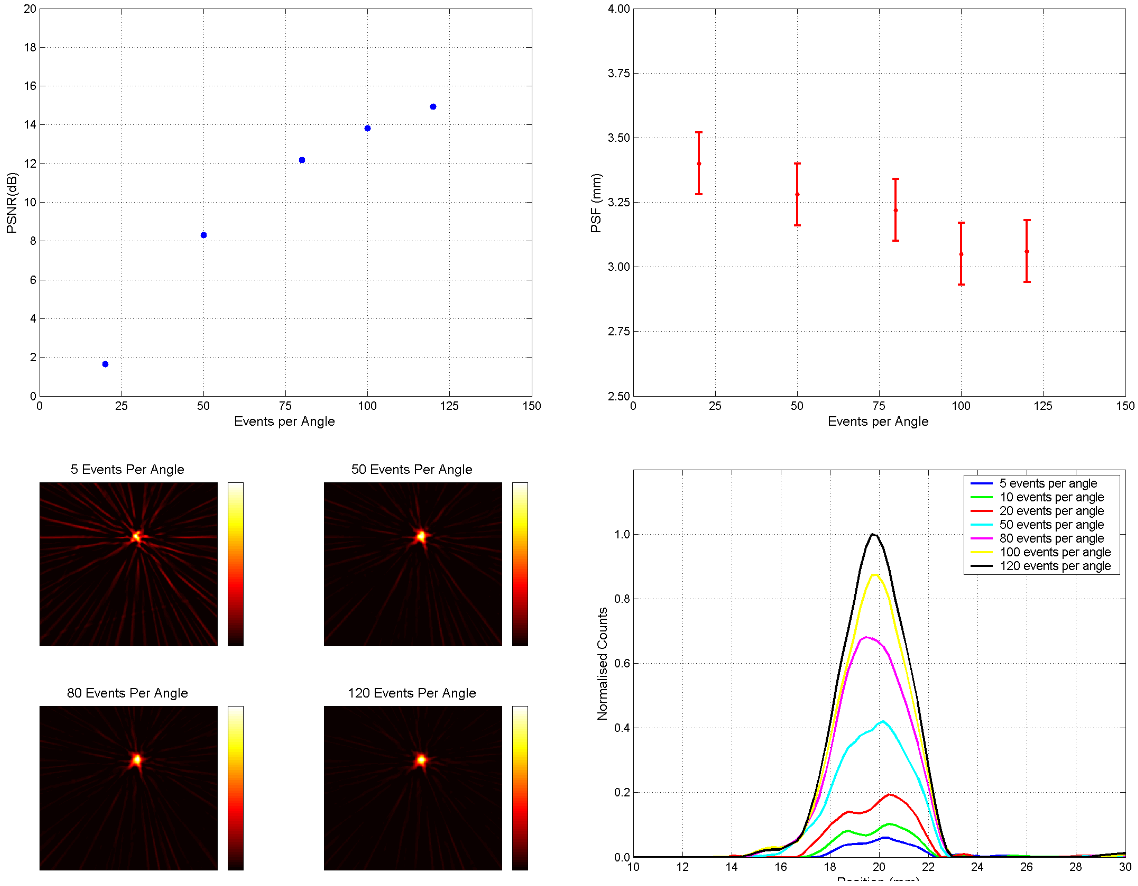

Figure 7.5: Left: The variation of PSNR as a function of the number of events included per angle (top) and FBP images reconstructed using 5, 50, 80 and 120 events per angle (bottom). Right: The variation in the PSF as a function of the number of events included per angle (top) and slices through the x-axis of the point source profile associated with each reconstructed image (bottom). It can be seen how as the number of events included in the reconstruction data set increases the quality of the resulting image improves.

slices through the point source profile of each image. Below 20 events per angle the images become severely limited by the lack of statistics and the PSF is poorly defined thus PSNR and PSF values are only plotted for images where between 20 and 120 counts are included at each angle.

From these results one can observe how the quality of the images increases steadily as larger numbers of counts are included at each angle. The PSF improves linearly as the number of counts included per angle increases. Above around 100 counts per angle the PSF

Slice	PSNR(dB)	FWHM$_x$ (mm)	FWHM$_y$ (mm)	FWHM$_{mean}$ (mm)
5	6.84	2.11(0.17)	2.34(0.17)	2.32(0.12)
6	10.26	1.88(0.17)	3.75(0.17)	2.82(0.12)
	-	3.05(0.17)	2.34(0.17)	2.70(0.12)
13	13.52	2.46(0.17)	3.16(0.17)	2.81(0.12)
14	10.41	3.28(0.17)	3.05(0.17)	3.16(0.12)
21	3.40	3.28(0.17)	3.05(0.17)	3.16(0.12)
22	0.57	3.52(0.17)	2.78(0.17)	3.15(0.12)

Table 7.2: Summary of results for the quality assessment of the six images presented in Figure 7.6. It should be noted that when imaging from Type 2 data, two sources are observed in slice 6 and a value of PSF FWHM is calculated for each source.

value may begin to plateau as the point source profile is accurately defined and the impact of including more events becomes less significant. This is illustrated by the variation in the x-axis point source profile displayed. Like the PSF, the PSNR value also improves with increasing counts asymptotically approaching a maximum value. These results illustrate the highly statistical nature of PET imaging (and gamma-ray imaging in general) and highlights the importance of maximising sensitivity and statistics wherever possible.

7.1.2 Type Two Events

Using only Type 2 events, the FBP images reconstructed for the six slices measuring point sources are presented in Figure 7.6 with the accompanying assessment of image quality in Table 7.2. These images once again show the presence of well localised point sources with values of PSF consistent with Equation 7.1. However, increased levels of artefacts are also present which may be explained by an increased uncertainty in the calculation of interaction position. The image from slice 6 now shows the presence of a second point source (the strong source which consistently appears in slices 13 and 14). This is a result of the phenomenon presented in Figure **??** although the reason for its occurrence here, and not when imaging with Type 1 ([1,1,1,1]) events, is unclear. An investigation of this may form part of the ongoing work towards the development of SmartPET image reconstruction.

In a conventional PET system events which scatter between individual scintillator crystals, an effect often referred to as Compton crosstalk [Val03], are commonly rejected [Par04].

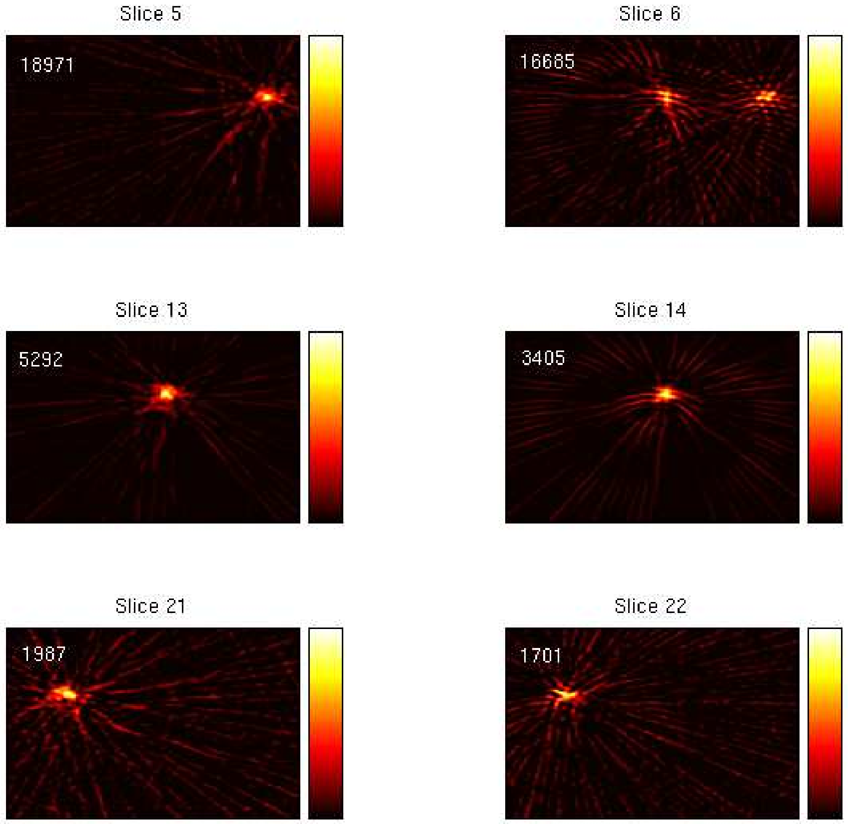

Figure 7.6: Images reconstructed from Type 2 events only. Two sources may now be observed in slice 6. The images show well localised point sources and display good spatial resolution. A somewhat increased presence of artefacts may be observed relative to the images presented in Figure 7.3.

The results presented here show how, while more prevalent in a HPGe PET system such as SmartPET due to the increased Compton scattering cross section at this energy (relative to scintillators), these events need not be vetoed and may in fact be used for image reconstruction, so long as the first interaction is identified correctly.

7.1.3 Type Three Events

The images reconstructed from processing Type 3 events are shown in Figure 7.7 while the associated image quality results are displayed in Table 7.3. These event types constitute the largest of the three data fractions investigated here and also pose the greatest challenge to the data processing algorithms. In these respects Type 3 events represent an important

Slice	PSNR(dB)	FWHM$_x$ (mm)	FWHM$_y$ (mm)	FWHM$_{mean}$ (mm)
5	7.28	4.45(0.17)	3.52(0.17)	3.98(0.12)
6	10.85	2.58(0.17)	3.00(0.17)	2.79(0.12)
	-	-	-	-
13	17.47	5.16(0.17)	4.22(0.17)	4.69(0.12)
14	15.39	2.93(0.17)	2.81(0.17)	2.87(0.12)
21	3.65	1.88(0.17)	2.11(0.17)	1.99(0.12)
22	1.70	-	-	-

Table 7.3: Table summarising the results of the quality assessment performed on the images presented in Figure 7.7. No values of PSF could be calculated for the source in slice 22 and the second source in slice 6 as the point source profile was too poorly defined. Due to the effect of limited statistics in the peak, an artificially low value of PSF is recorded for the point source in slice 21.

data subset and the ability to use them for imaging represents a major step forward for the SmartPET project.

The images presented in Figure 7.7 demonstrate that these events may be used to successfully localise the three point sources. The images show increased presence of artefacts and slightly broadened PSF profiles due to the increased uncertainty in the calculation of interaction position. Despite this however, the images remain good quality with generally impressive values of PSNR. For slices 21 and 22, the point source profile is poorly formed resulting in an artificially narrow FWHM for the source in slice 21 and an unmeasurable PSF for that in slice 22. This result is once again due to statistical limitations, an effect demonstrated by the correspondingly low values of PSNR for these images. While the number of counts included in the images may be larger than that from other data subsets, the increased uncertainty in defining an accurate interaction position and/or LoR reduces the number of counts falling into the peak.

7.1.4 Identification of First Hit

In Chapter 6 the method for first hit identification was discussed. Clearly, if image quality is to be maintained, it is essential that this technique correctly identifies the hit from which to define the LoR. It is not possible to directly ascertain how often the first and second hit are correctly distinguished, the validity of the assumptions made when performing the first hit

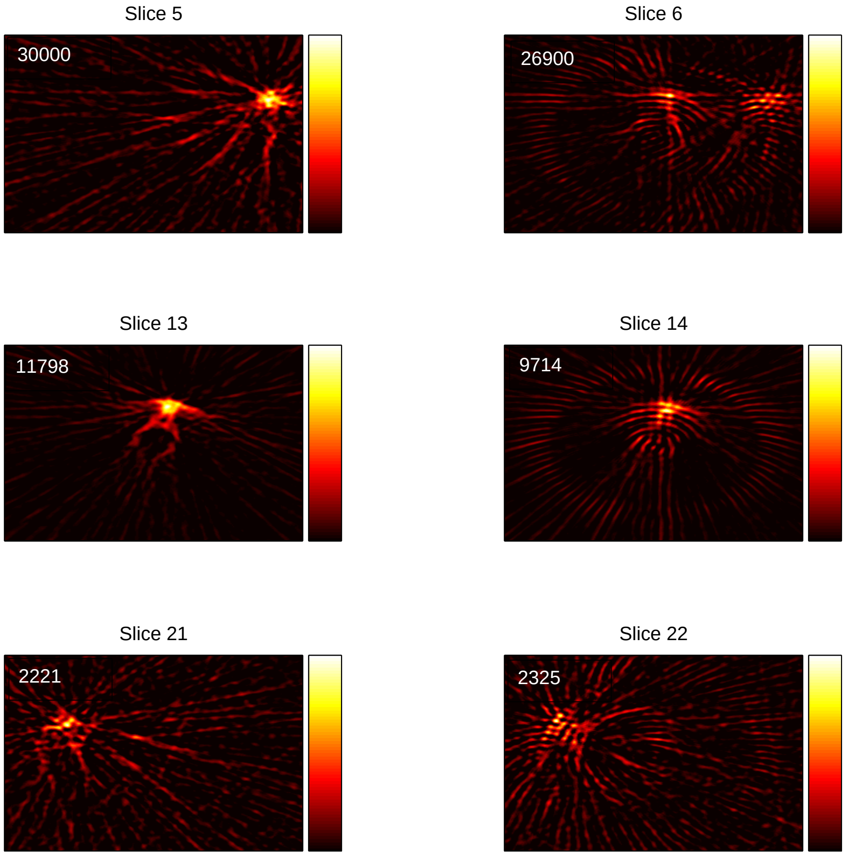

Figure 7.7: Images reconstructed from Type 3 events only. The presence of artefacts resulting from inaccurate identification of the correct LoR are apparent although the point sources are still generally well defined in the major slices.

identification have however been investigated. By processing Type 3 events using reversed criteria for determining the first interaction, the impact on the quality of the reconstruction has been assessed. The first hit is therefore now identified as being the deepest interaction (assumes backscattering is more probable at 511keV). Using this basis for event processing the resulting FBP images are displayed in Figure 7.8. These images show reduced quality in comparison to those presented in Figure 7.7 with the increased impact of artefacts resulting in consistently lower values of PSNR. The point source profiles are poorly defined and a PSF value can only be accurately calculated for slice 5 with the mean value found to be 4.80(0.12)mm.

	Slice 5		Slice 13	
	PSNR (dB)	FWHM$_{mean}$ (mm)	PSNR (dB)	FWHM$_{mean}$ (mm)
Event Type 1	12.15	2.87(0.12)	16.37	2.98(0.12)
Event Type 2	6.84	2.32(0.12)	13.52	2.81(0.12)
Event Type 3	7.28	3.98(0.12)	17.47	4.69(0.12)

Table 7.4: Summary of the quantitative image quality assessment of the images from slices 5 and 13 reconstructed from each of the three event types.

The drop in counts observed when using the modified criteria provides confidence in the assumption that the most probable interaction sequence is a shallow interaction depositing greater than 50% of the initial energy follwed by a deeper interaction depositing the remaining energy. The degradation in image quality resulting from appying these modified criteria also provides confidence in the standard approach to identifying the first hit. In the future, it may be possible to accurately reconstruct the interaction sequence on an avent by event basis using advanced Gamma Ray Tracking (GRT) algorithms [Lee99], [Wie03]. These techniques, two of which are reviewed and compared in [Lop04], aim to identify the path of a scattered gamma ray based on the kinematics of Compton scattering [Sch99] and probabilistic approaches [Piq04] to determine interaction sequences. Applying such methods to PET data would in principle allow the first interaction of a 511kev gamma ray to be identified without the need to reject events. The use of GRT algorithms is likely to become increasingly important if events of fold three or above are to be used for imaging. It should be noted that the use of GRT techniques would be likely to require more advanced PSA approaches and due to the computationally expensive nature of both algorithms, neither would lend themselves to fully online data processing.

7.1.5 Influence of Event Type on Image Quality

From the results presented in the previous sections one can observe how the event type directly influences the quality of the reconstructed images. As the quality of the event decreases and the accuracy with which the LoR is defined is diminished, the image quality can be seen to degrade. Table 7.4 summarises the PSNR and mean PSF values for the most well defined point sources (those in slices 5 and 13) for each event type.

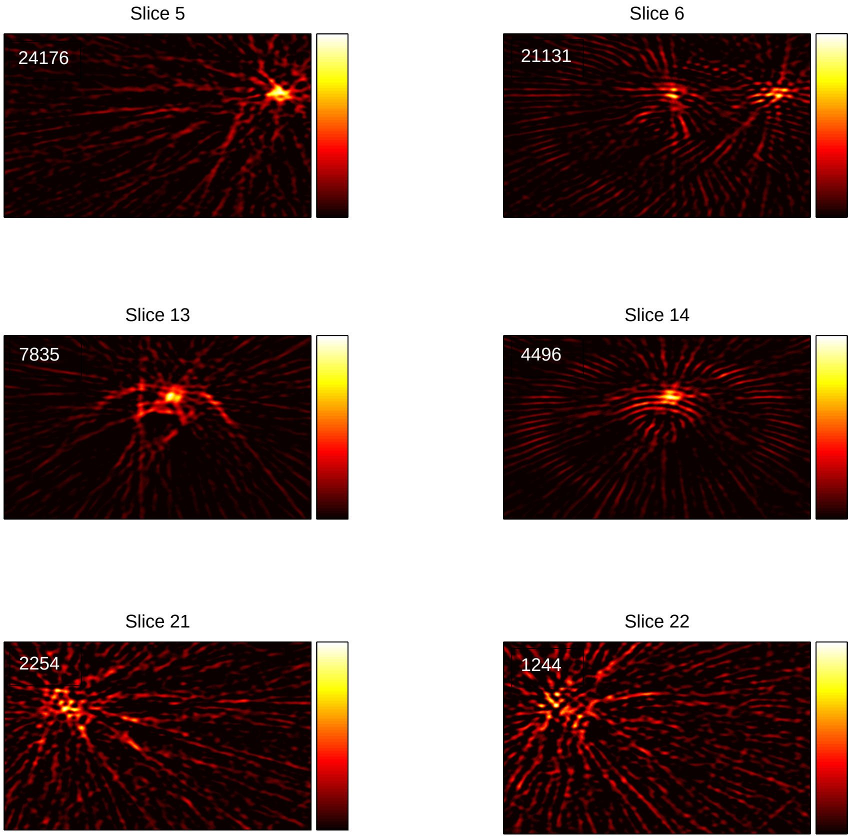

Figure 7.8: FBP images reconstructed from Type 3 events where reversed criteria for determining the first hit were applied. These images exhibit reduced quality relative to those in Figure 7.7 which use the standard criteria as discussed in Chapter 6.

Influence on Spatial Resolution

For the most well defined point sources (slice 5 and slice 13 respectively) the value of the PSF increases by 1.1mm and 1.7mm FWHM between imaging with Type 1 and Type 3 events. This corresponds to a reduction in spatial resolution of 39% and 57% for the point sources in slices 5 and 13 respectively. It is observed that the values of PSF when imaging with Type 1 and Type 2 events remain generally consistent, significant degradation only taking place when imaging with Type 3.

Influence on PSNR

From initially including only Type 1 events, the PSNR values can be seen to fall when imaging with only Type 2 events and then rise again when using only Type 3. The initial drop in PSNR is likely to be due to the uncertainty in identifying the gamma-ray interaction position (and thus LoR definition) introduced by using Type 2 events. This has the effect of reducing the number of counts falling into the point source profile relative to the background and thus reduces the PSNR. When using Type 3 events this uncertainty still exists (and is likely to become more severe) but is balanced somewhat by the inclusion of larger numbers of events in the image matrix.

By allowing larger fractions of the PET data set to be included in the reconstruction a trade off is established between imaging sensitivity and image quality. The ability to distinguish between these event types and treat them individually is a luxury afforded by a HPGe PET system such as SmartPET and future developments may lead to events being individually weighted depending upon their usefulness for imaging. In this way it may be possible for both sensitivity and image quality to be maintained.

7.1.6 Imaging All Events

In reality, the data subsets presented in the previous sections would be unlikely to be used individually and ideally the SmartPET system should aim to process all coincident events resulting from 511keV gamma rays. Images have therefore been reconstructed using events up to and including [2,2,2,2] interactions, just over 60% of the entire PET data set. The resulting images and quality assessment thereof are displayed in Figure 7.9 and Table 7.5 respectively. The inclusion of large numbers of events, all of which can be potentially used for imaging in their own right ensures that these images exhibit high values of PSNR with spatial resolution approaching that determined by the limitations previously discussed.

In comparison with Type 1 events, the only event type to have been used for imaging prior to this work, a factor of 3 increase in sensitivity is achieved, and PSNR values improve by a factor of ∼1.5. In general, a slight degradation in spatial resolution is observed (∼2% increase in PSF for the point source in slice 5) but in terms of image quality and system performance may be offset against the increase in PSNR and sensitivity.

Based on the pixel-by-pixel sum of the six slices a total projection along the rotation

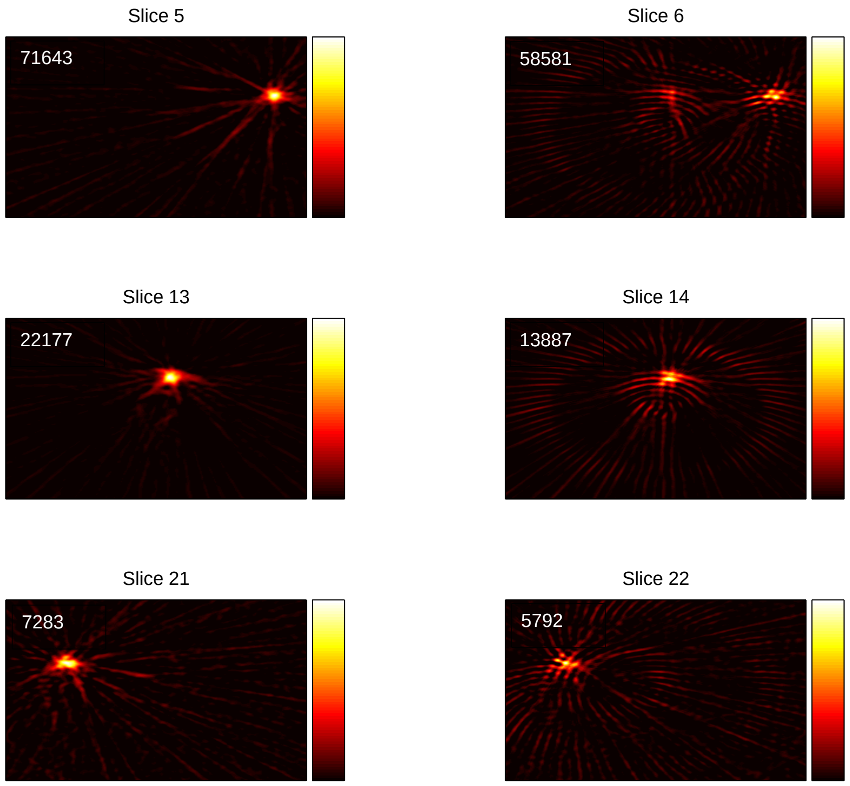

Figure 7.9: FBP images reconstructed using all data up to and including [2,2,2,2] events.

Slice	PSNR(dB)	FWHM$_x$ (mm)	FWHM$_y$ (mm)	FWHM$_{mean}$ (mm)
5	17.54	2.58(0.17)	3.28(0.17)	2.93(0.12)
6	18.69	3.05(0.17)	2.11(0.17)	2.58(0.12)
	-	-	-	-
13	24.61	3.05(0.17)	3.52(0.17)	3.28(0.12)
14	19.38	3.52(0.17)	2.93(0.17)	3.22(0.12)
21	13.03	3.75(0.17)	3.63(0.17)	3.69(0.12)
22	9.06	-	-	-

Table 7.5: Table summarising the image quality assessment performed on the images in Figure 7.9 where the images were reconstructed using all events up to and including [2,2,2,2] events.

axis has been created. This image is displayed in Figure 7.10 along with a three-dimensional projection of the reconstructed matrix with the three point sources located at pixel numbers (52,166), (141,169) and (230,171)[1].

Using the centroid of each point source profile the ratio of intensities relative to the strongest point source (from left to right in the image) is found to be 0.239(0.001):1.000(0.004):0.555(0.003) while the ratio of source activities is 0.046:1.000:0.121. While no exact correction for the non-uniformity in response discussed in Section 7.1.1 can be performed, an approximate correction based on the coefficients from Figure 7.4 results in an intensity ratio of 0.013(0.007):1.000(0.072):0.151(0.008). The corrected ratio is in closer agreement to that expected from the source activities.

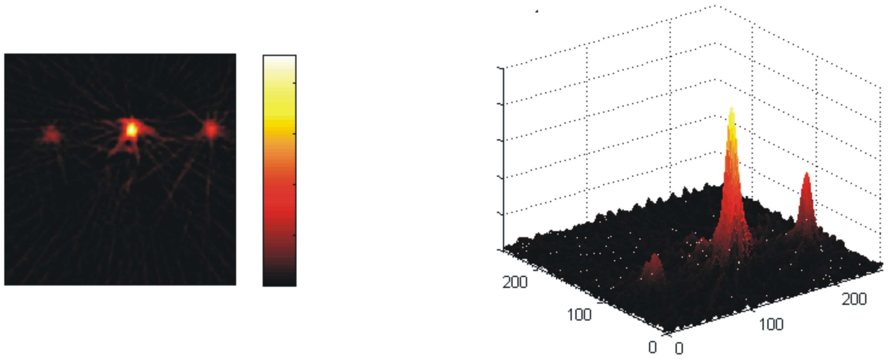

Figure 7.10: Total projection along the rotation axis based on the pixel-by-pixel sum of the six images in Figure 7.9 (left) along with a three dimensional projection of the same image (right).

In the case of all images presented, the presence of artefacts reduces the perceived image quality, and in a clinical imaging scenario may degrade their performance as a diagnostic tool. These artefacts may be reduced or even eliminated through the use of the MLEM algorithm for image reconstruction. This technique has therefore been applied to the sinograms from the six major slices (Figure 7.11) and a second sum image created based on these slices (Figure 7.12). These images, resulting from ten iterations of the MLEM algorithm, are reconstructed onto a 128x128pixel grid from sinograms containing parallel LoRs only. The system matrix implemented for use in this work contains only geometric considerations. This sparse matrix is based upon a forward projection calculation where a point at the

---

[1] The coordinate system of the image refers to a cartesian grid where the origin, (0,0), is at the bottom left corner of the reconstructed image.

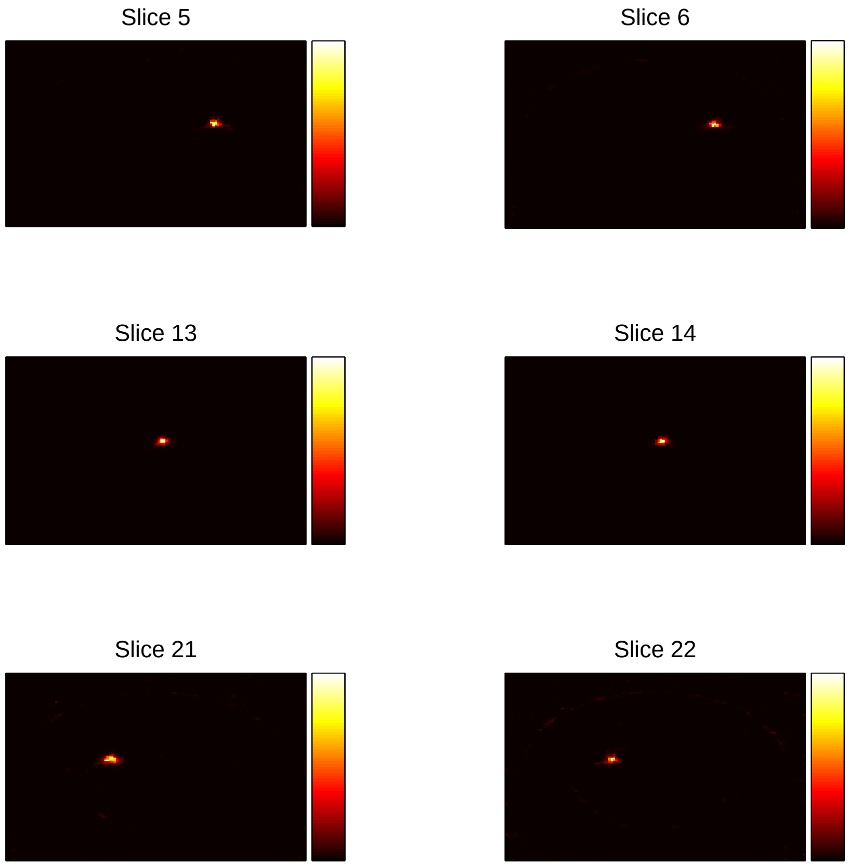

Slice 5

Slice 6

Slice 13

Slice 14

Slice 21

Slice 22

Figure 7.11: Images of the three ^{22}Na point sources after 10 iterations of the MLEM algorithm. These images were constructed from all data up to and including [2,2,2,2] events. The images, each reconstructed onto 128x128 pixel grid from sinograms containing parallel LoRs only, show little or no presence of artefacts and exhibit PSF values of between 1.4 and 1.5mm.

centre of each pixel is forward projected at each measured projection angle. The detector element covering the projected position is given a probability of one to measure a decay from that pixel while all other parallel LoRs at this projection angle are given a probability of zero. The MLEM reconstructed images in Figure 7.11 all show the three point sources well localised with no obvious presence of reconstruction artefacts. The MLEM algorithm provides fine spatial resolution and excellent PSNR values. With the exception of the image from slice 22 which is limited by poor statistics, each point source is reconstructed with a

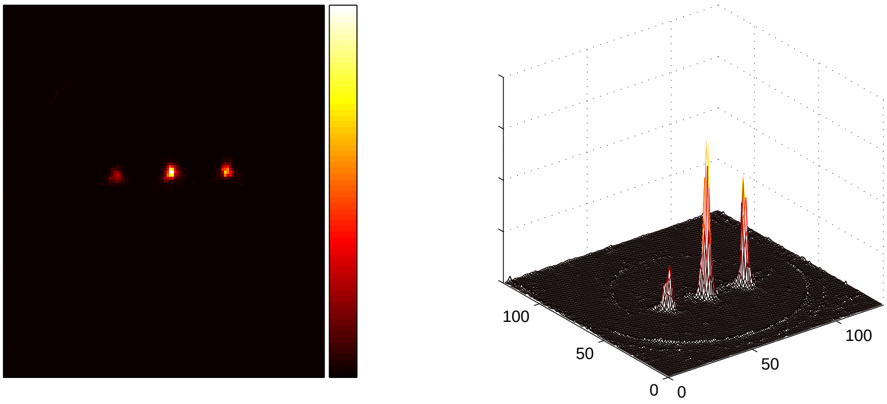

Figure 7.12: Left: Total projection along the rotation axis based on the pixel-by-pixel sum of the six images in Figure 7.11. Right: A three-dimensional projection of the same image. Using the MLEM algorithm for image reconstruction the spatial resolution and PSNR values are much improved relative to those reconstructed with FBP.

Slice	PSNR(dB)	FWHM$_x$ (mm)	FWHM$_y$ (mm)	FWHM$_{mean}$ (mm)
5	54.14	1.45(0.17)	1.40(0.17)	1.43(0.12)
6	54.12	1.55(0.17)	1.55(0.17)	1.55(0.12)
13	54.16	1.40(0.17)	1.42(0.17)	1.41(0.12)
14	54.15	1.38(0.17)	1.40(0.17)	1.39(0.12)
21	53.82	1.79(0.17)	1.41(0.17)	1.60(0.12)
22	53.24	1.31(0.17)	1.13(0.17)	1.22(0.12)

Table 7.6: Table summarising the image quality assessment performed on the images in Figure 7.11.

mean PSF value between 1.4 and 1.6mm while the PSNR value of each image is around 54dB to two decimal places (The results of the image quality assessment of each slice are presented in Table 7.6). The sum image presented in Figure 7.12 exhibits reconstructed PSF profiles of, from left to right, 1.50mm, 1.41mm and 1.42mm FWHM. These values are consistent with the limiting spatial resolution imposed by Equation 7.1 as discussed in Section 7.1.1 of this work. In the case of these images no ratio of point source intensities has been calculated as MLEM reconstruction, unlike FBP, is not reliably quantitative by nature. A more accurate implementation of the system matrix is likely to be required for quantitative PET imaging.

7.2 Line Source Imaging

The ability of the the SmartPET system to image extended source distributions was assessed by reconstructing images of the ^{22}Na line source. For each data set the highest quality ([1,1,1,1]) events were used for reconstruction. With each line source reconstructed in terms of the discrete slices through the SmartPET rotation axis, each slice was then projected into a three-dimensional volume, effectively stacking the slices in order to produce a '2.5D' PET image. Using the MATLAB programming environment [MAT] an isosurface has then been applied at the half-maximum value rendering the line source as a 3D volume. Figures 7.13 and 7.14 show the reconstructed images of the line source in the orientations discussed in Chapter 6.

7.2.1 Orientation One

Figure 7.13 shows reconstructed images of the line source parallel to the rotation axis using both the FBP (left) and MLEM (right) algorithms. This reconstruction was performed in terms of twelve slices as the source has uniform distribution and covers the entire length of the detectors. The increased granularity provided by imaging from twentythree slices was therefore not required. The images show how when the line source was placed into the SmartPET system for data collection it was slightly off-axis resulting in the skew observed in the images. Taking slices through the line sources reveals that the reconstructed LSF has a value of 5.70(0.17)mm FWHM in x and y when using FBP where the true diameter of the source is 2.5mm. The MLEM image shows much better spatial resolution, with a LSF of 2.69(0.17)mm. These values appear to be consistent with the limiting spatial resolution incurred by positron range blurring, gamma-ray non-colinearity and reconstruction blurring.

7.2.2 Orientation Two

Reconstructed images of the line source parallel to axis of rotation with an elevation of around 45° are presented in Figure 7.14. The image on the left shows the volumetric image resulting from FBP reconstruction of twelve slices along the rotation axis while the image on the right was constructed by applying ten iterations of the MLEM algorithm to each of twentythree two-dimensional slices. As the line source is off axis and reconstructed from discrete slices, the application of the isosurface, and the need to interpolate between slices,

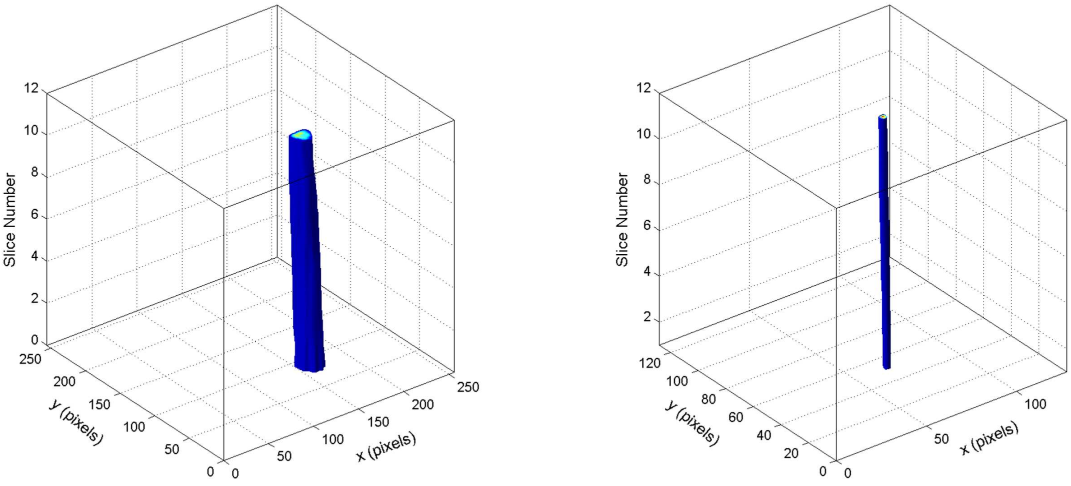

Figure 7.13: Volumetric images of the ^{22}Na line source parallel to the rotation axis of the SmartPET system. Using coincident single pixel hits the images was reconstructed in terms of twelve discrete two-dimensional slices. These slices have then been projected into a three-dimensional volume and an isosurface applied at the mean FWHM value. The image on the left is the result of FBP reconstruction while the image on the right shows the reconstruction from ten iterations of the MLEM algorithm.

results in the non-uniformity which may be observed in the structure of the lines along their lengths. The would be alleviated by the use of fully three-dimensional image reconstruction reconstruction.

7.3 Pseudo-Phantom Imaging

The pseudo-phantom was reconstructed with the FBP algorithm into twelve two dimensional slices from [1,1,1,1] events. Figure 7.15(top left) shows the twelve slices projected into a three dimensional volume and individual isosurfaces applied at half maximum values of the line and point source profiles. Figure 7.15(top right) shows a slice in which the line source and one of the point sources are seen. Only one point source is observed due to the failure of an electronics channel during data acquisition. In Figure 7.15(top left) the point source is falsely elongated as a consequence of its appearance in three reconstruction slices (as discussed earlier in this chapter). Quantitative analysis of the point and line source

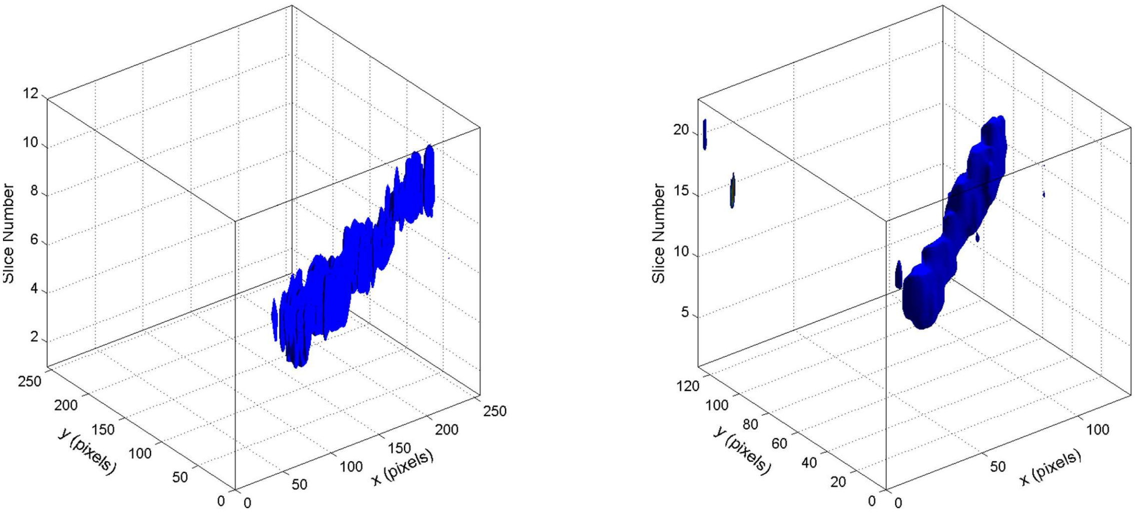

Figure 7.14: Volumetric images of the ^{22}Na line source parallel to the rotation axis of the SmartPET system with an elevation of around 45°. The image on the left is a result of FBP reconstruction while the image of the right was produced by applying ten iterations of the MLEM algorithm to each of the twenty three slices through the rotation axis.

profiles reveals that the pseudo-phantom exhibits an average PSF value of 3.04(0.12)mm and LSF value of 5.30(0.12)mm. The pseudo-phantom data was also reconstructed using the MLEM algorithm and Figure 7.15(bottom left) and (bottom right) shows the resultant volumetric and planar images respectively. It can be observed how the use of the iterative algorithm once again provides improved spatial resolution and a reduction in the presence of reconstruction artefacts. From these images the mean PSF is calculated to be 1.78(0.12)mm while the LSF is 2.72(0.12)mm. These images demonstrate for the first time the ability of the SmartPET system to distinguish multiple features in a distributed source arrangement with fine spatial resolution.

7.4 Phantom Imaging

As with the point and line sources, images of the phantoms were reconstructed using the FBP and MLEM algorithms. Images of a reconstructed two-dimensional slice from the hot-phantom data are presented in Figure 7.16. The images on the top row show FBP

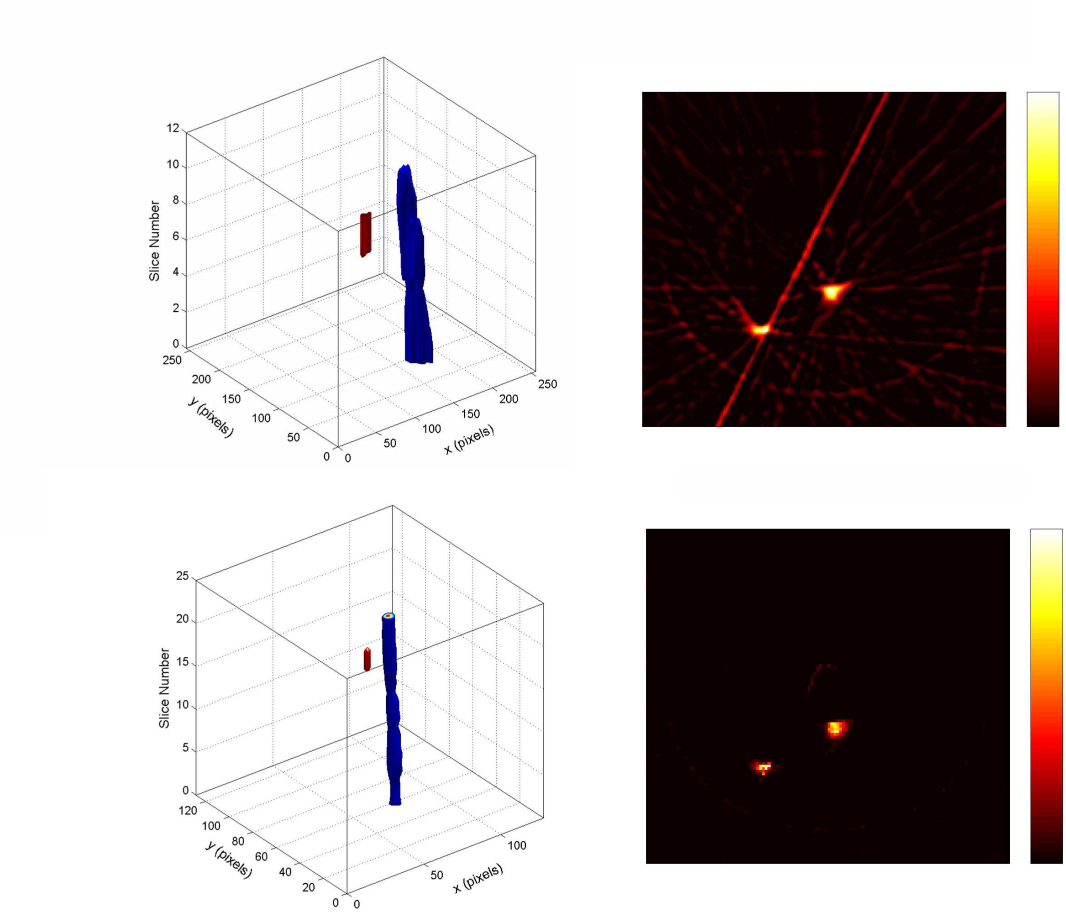

Figure 7.15: Left: Volumetric reconstructions of the pseudo-phantom using FBP (top) and ten iterations of the MLEM algorithm (bottom). The point source appears artificially elongated due to its appearance in multiple reconstruction slices. Right: Two-dimensional slices showing the presence of the line source and a single ^{22}Na point source from FBP reconstruction (top) and MLEM reconstruction (bottom). Only one point source may be observed in these images as the failure of an electronics channel during data acquisition resulted in no counts being recorded from the strip 'containing' the second source.

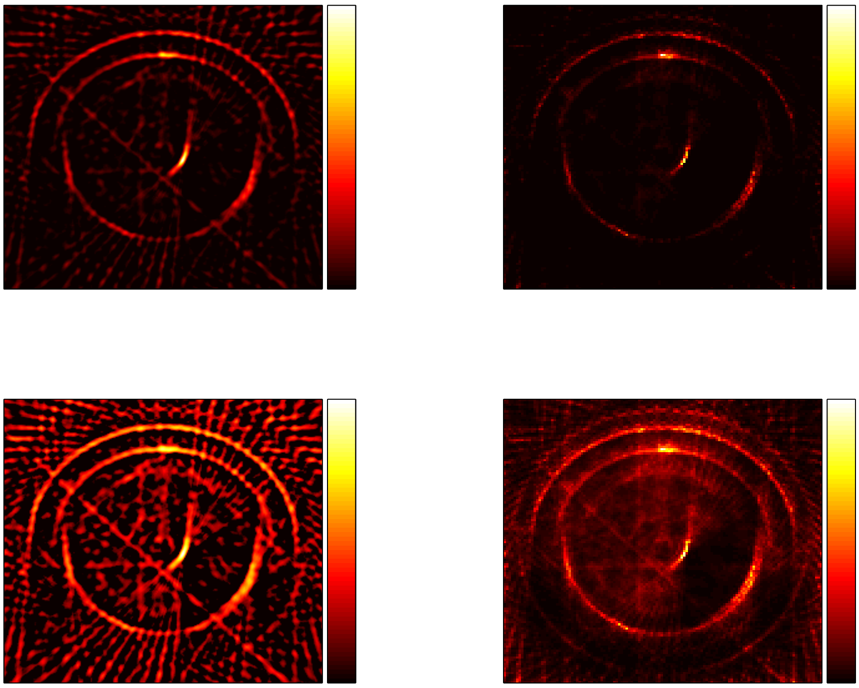

Figure 7.16: Reconstructed images of the hot phantom. The top row shows images reconstructed with the FBP algorithm (left) and ten iterations of the MLEM algorithm (right). The bottom row shows the same images where the square root of the image matrices has been taken in order to emphasise any fine detail. These images show the general structure of the phantoms but the rods remain unresolved, largely due to a combination of insufficient statistics and limited angular sampling.

(left) and MLEM (right) images while those on the bottom row show the square root of the image matrices in order to emphasise any small details in the images. The images in Figure 7.16 represent the limit of performance of the SmartPET system at this time. While the general structure and shape of the phantoms may be observed the location of the rods is largely undefined. It is believed that significant improvement may be obtained in future tests through increased statistics, increased angular sampling and the development of a more advanced MLEM algorithm. Imaging of the phantoms may be considered to be a major focus of future experimental work for the SmartPET project.

Chapter 8

Conclusions and Discussion

The experimental results presented in this study demonstrate the performance of a prototype Positron Emission Tomography system utilising planar HPGe detector technology. The experimental measurements undertaken provide evidence of the feasibility of such a system for small animal imaging. It has been shown how the use of digital Pulse Shape Analysis techniques may be employed in order to improve the achievable image quality.

By performing high precision scans of one the SmartPET HPGe detectors with finely collimated gamma-ray beams at a range of energies the performance and response of the detector as a function of gamma-ray interaction position has been quantified. This analysis has facilitated the development of parametric Pulse Shape Analysis techniques and algorithms for the correction of imperfections in detector response. These algorithms have then been applied to data from PET imaging measurements using both SmartPET detectors in conjunction with the specially designed rotating gantry.

A number of point sources have been imaged and it has been shown how, when using simple PSA approaches, the nature of an event has direct implications for the quality of the resulting image. Over 60% of coincident events from 511keV gamma rays have been processed in imaging these point sources, increasing the imaging sensitivity by a factor of three in comparison to previous work [Mat06]. The absolute detection sensitivity of the SmartPET system has been found to be 0.99%.

The SmartPET system has been used to image distributed sources for the first time. A ^{22}Na line source was imaged in a number of different orientations and reconstructed with a spatial resolution approaching the fundamental limitations imposed by gamma-ray non-colinearity and positron range blurring. Increasingly complex source distributions have been imaged, demonstrating the ability of the system to resolve multiple features with fine spatial resolution. These measurements then allowed the current limitations of the system to be identified.

8.1 Sensitivity

The absolute detection sensitivity of the SmartPET system is 0.99% for a point source placed at the centre of the field of view (CFOV) and a detector separation of 130mm. A review and comparison of several commercially available small animal PET systems is presented in [Lar06] where the absolute sensitivity (CFOV point source) is seen to vary from 1.3% to 6.5% for the five systems reviewed. Each of these systems has either a four-head or ring geometry and as such each provides greater solid angle coverage than the SmartPET system. If the SmartPET system was to take the form of a four-head geometry the sensitivity would double to 1.98%, rising to around 3% for a ring geometry.

Where the SmartPET system holds an advantage over those commercial systems with higher absolute sensitivity is in the fraction of events which may be used for imaging. In PET detectors using BGO scintillator elements, only approximately 44% of 511keV gamma rays undergo photoelectric absorption in a single interaction, with the remaining 56% undergoing at least a single Compton scatter [Hoo03], [Zav06]. The fraction of (total incident) gamma rays scattering between two detector elements may be as great as 30% for 2x2x10mm^3 crystals [Lev97]. As these events are typically rejected the imaging sensitivity is decreased. The results presented in this work show how similar events in the SmartPET system may be successfully used for imaging. Future developments in data processing for SmartPET should allow ever larger event fractions to be included through the use of more complex PSA and the potential application of Gamma Ray Tracking (GRT) algorithms. This coupled with development of the image reconstruction algorithms in order to allow more LoRs to be utilised should result in the effective imaging sensitivity of the SmartPET system rivalling, and in some cases surpassing that offered by current commercially available small animal PET imagers.

8.2 Spatial Resolution

Through point and line source imaging it has been shown that the SmartPET system is capable of achieving reconstructed image spatial resolution limited only by the fundamental constraints of positron range blurring, gamma-ray non-colinearity and reconstruction induced blurring. In imaging ^{22}Na point sources the reconstructed point source profiles are found to have typical FWHM values of 2.5-3mm while a ^{22}Na line source of 2.5mm inner diameter has been reconstructed with FWHM of 5.70(0.12)mm when reconstructing with a FBP algorithm. When reconstructing the point source data using an MLEM algorithm the FWHM of the point source at the centre of the field of view is found to be 1.41(0.12)mm. Processing the line source data with the MLEM algorithms yields an image with a LSF of 2.69(0.12)mm.

8.3 Performance

At the present time, no standard protocol exists for the evaluation of small animal PET scanners thus comparisons based on measurements of physical characteristics are typically employed. Commonly, performance is described in terms of absolute detection sensitivity and image spatial resolution although it is noted in [Web04] how the lack of standardised procedures makes the results significant but not strictly comparable. Using the metrics of sensitivity and spatial resolution, five commercially available dedicated small animal PET systems are reviewed and compared in [Lar06]. These systems are:

- YAP-PET: A dedicated PET/SPECT system consisting of a rotating four-head detection system based on 20x20 individual 2x2x30mm^3 YAP (Yttrium Aluminium Perovskite) crystals.
- MICROPET Focus 120: An LSO based system consisting of four rings of (13824) 1.5x1.5x10mm^3 crystals.
- MOSAIC: A scanner consisting of a ring of 16680 discrete GSO (Gadolinium Oxyorthosilicate) crystals of 2x2x10mm^3 arranged in 57 rows.
- EXPLORE VISTA 32: A system comprising two rings of 6084 LGSO/GSO detectors. Detectors are arranged in 18 modules per ring where each module consists of a 13x13

array of 1.5x1.5x15mm^3 elements.

- QUAD-HIDAC 32: A large area gas filled detector in four-head configuration. Each head consists of a stack of eight HIDAC detectors.

Figure 8.1 shows the performance of these systems in terms of the absolute detection sensitivity and reconstructed spatial resolution (FWHM) for imaging a point source (^{22}Na or ^{18}F) at the centre of the field of view (CFOV). This plot shows how the spatial resolution achievable with commercial systems varies between 1 and 2.2mm with sensitivity values ranging from 1.3% to 6.5% as discussed. The performance of the SmartPET system has also been plotted showing spatial resolution of 1.41mm and absolute sensitivity of 0.99%. For comparison purposes a second data point has been plotted for SmartPET, indicating the theoretical sensitivity if the system was to take the form of a ring geometry. With its current performance the SmartPET system compares favourably with the commercial systems reviewed. Only the MicroPET Focus 120 system exhibits better performance in terms of both spatial resolution and sensitivity. It is perhaps worth noting that the impressive spatial resolution offered by the Quad-Hidac system is likely to be due to the use of system specific iterative reconstruction algorithms designed to optimise the imaging performance.

8.4 Future Developments

This study demonstrates the current performance of the SmartPET system and provides a point from which further development work may continue. This is likely to focus on three main areas of the system; implementation of the electronics, evolution of data processing and PSA techniques and the advancement of the reconstruction algorithms.

8.4.1 Implementation of the Electronics

As has been previously discussed, the full SmartPET system will use a compact PCI based digital electronics solution in place of the GRT4 cards employed in this work. This two tier system (an overview is provided in [Bos05]) will provide ‘level one’ processing of the signals from each detector face with algorithms for digitisation and calculation of energy. A digital CFD will allow accurate time stamping to be provided through a 100MHz global clock and drive geometric zero suppression. Level two cards will then merge the data from all

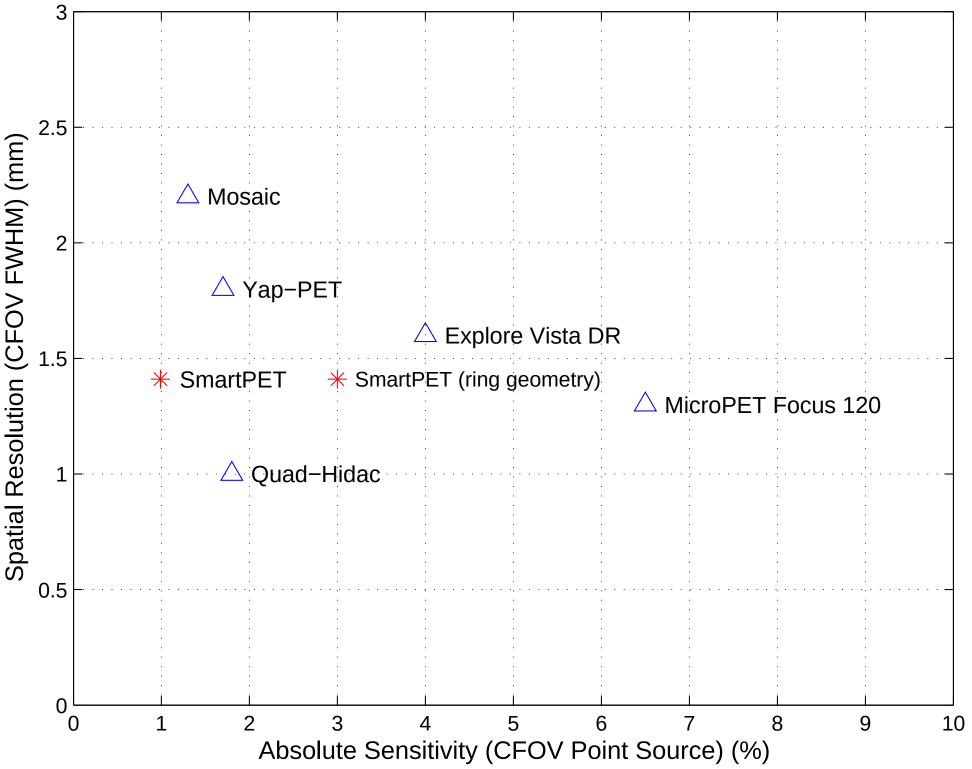

Figure 8.1: Plot comparing performance of current commercial PET systems for small animal imaging in terms of their sensitivity and image spatial resolution. The current performance of the SmartPET system is also plotted along with the sensitivity value which could be achieved if the system was to take the form of a ring geometry.

channels, performing PSA and event building within their FPGA and DSP components. As discussed in Chapter 6 the increased data rate allowed by this system will result in shorter scan times while the free running nature of the DAQ will allow events to be built based on a variable coincidence window controlled by the user. Investigating the influence of this coincidence window on the performance of the system will allow optimisation of the timing resolution. A necessary first step is therefore optimisation of the digital CFD algorithm in order to provide the best achievable timing resolution.

8.4.2 Evolution of Pulse Shape Analysis

The application of PSA algorithms to PET data is crucial in order to provide good spatial resolution and allow 'complex' gamma-ray interactions to be used for imaging. The approaches developed in this work are based on relatively simple parametric approaches ideally suited to online implementation. Future developments are likely to focus upon both improving these existing techniques and developing more advanced approaches.

Development of Parametric Pulse Shape Analysis

The parametric PSA techniques developed and applied in this work may be improved by providing more accurate depth of interaction information. This is especially important if one is to correct for parallax error when imaging from non-parallel Lines of Response. Ongoing work has suggested that the risetime correlation approach may be extended to provide depth of interaction resolution of the order of 1mm. This should be pursued along with an investigation into the ideal parameter with which to characterise the charge pulse risetime as discussed in Section 5.3. In order to maximise the sensitivity of the method it is suggested that the risetime should be described in terms of parameters which include as much of the trace as is practicable (i.e. correlation of T10-T95 values). For a comprehensive validation of these parametric techniques it may be useful to analyse high precision scan data comparing the derived interaction position against the collimator position on an event by event basis, quantifying the absolute position resolution achievable with these methods.

Further Pulse Shape Analysis

The PSA algorithms proposed for the AGATA and GRETA projects along with prototype gamma-ray imagers such as the SPEIR (SPEctroscopic Imager for γ-Rays) system [Mih04] use approaches which compare the pulse shape response of the detector to a database of simulated pulse shapes (referred to as a basis data set) from known interaction positions on an event-by-event basis. These algorithms have been shown to reliably provide spatial resolution of ~1mm from multiple hit events with the ability to distinguish multiple interactions occurring within a single pixel [Mih04]. The output of these algorithms are passed to the input of GRT routines in order to accurately reconstruct the gamma-ray interaction sequence. The use of similar analysis techniques should, in principle, provide the SmartPET system with the capability to achieve optimal image spatial resolution irrespective of event type while using all detected events for reconstruction. This will require a full electric field simulation of the SmartPET detectors to be performed in order to create the basis data set, while high precision experimental pulse shapes must be available for the purposes of validation [Nel07].

Whether improvements in performance resulting from the use of advanced PSA techniques translate to improvements in image quality is yet to be seen, as is whether or not the increased CPU requirements of database matching approaches are justified by improved imaging performance. It is clear that advanced PSA and GRT algorithms must be implemented offline, with the AGATA collaboration designing a dedicated ‘PSA farm’ [Des05c] for event processing. Such large scale processing requirements do not exist for the SmartPET system. The primary PSA algorithm being tested for the GRETA spectrometer currently requires around 3ms to process each interaction (up to and including two interactions in a given segment) using a standard PC (2GHz processor) [Dox07], a rate likely to be acceptable for offline processing of small animal PET data.

8.4.3 Advancement of the Image Reconstruction Algorithms

The image reconstruction algorithms developed prior to this work and applied to imaging data here have been adequate for the reconstruction of relatively simple source distributions during the development of the SmartPET system. Significant scope remains for expanding and improving both the FBP and iterative reconstruction algorithms. At this time, the major limitation on imaging sensitivity is in the fraction of LoRs which may be used. A feasible next step is therefore the inclusion of oblique LoRs in addition to parallel and ‘almost parallel’ LoRs and the potential implementation of fully three dimensional image reconstruction. While the use of FBP reconstruction is useful for the purpose of system development, if the SmartPET system is to compete with more mature PET imagers and meaningful comparisons are to be drawn between their relative performance, the advancement of the iterative reconstruction algorithms is essential. This continues to be a very active research topic around the world and the use of HPGe detectors may allow new avenues to be explored. In imaging complex source distributions such as phantoms (and ultimately small animals) a reliable system matrix must be developed. In the short term this will involve expanding the current algorithm beyond imaging relatively simple source distributions with only parallel LoRs. Longer term work may focus upon including more sophisticated modelling to incorporate scatter and random correction and weighting factors for various event types.

8.4.4 Imaging Measurements

The SmartPET system should aim to perform imaging measurements using the new digital electronics, demonstrating the ability to operate at high count rates. Initially, scanning of the phantoms should be repeated, with imaging of a small rodent being the ultimate goal. It may also be interesting to quantify the system performance across the entire FOV as scintillator based PET systems routinely exhibit non-uniform response. Some non-uniformity of response has been observed in this work, the nature of which is worthy of further investigation. This analysis may take the form of experimental measurements of a distributed source imaged at different locations within the FOV coupled with complimentary Monte Carlo simulations.

The ability to collect data at high rates will allow measurements to be taken which employ increased angular sampling. Scanning over the full 180° range in smaller angular increments will improve the quality of images reconstructed with FBP by removing the star artefacts. As the data presented in this work was collected by rotating the SmartPET detectors in 5° steps it is suggested that, in future, measurements should be taken every 2°.

8.5 HPGe in Medical Imaging

In concluding this study the current position and potential future role of HPGe systems for medical imaging is discussed. For over twenty years the use of HPGe detectors in medical imaging applications has shown great promise [Has91], [Kau78], [Rus80]. Later, with the advent of segmented HPGe detectors and the increasing availability/performance of fast digital electronics, the combination of unrivalled energy resolution, fine position resolution without loss of sensitivity and the use of large event fractions implied that a HPGe device may be capable of providing diagnostic images of high spatial resolution while potentially reducing patient dose and/or scan times. The performance of the SmartPET system continues to suggest that this may be a reality and as proof of principle for an integrated PET system provides evidence in support of this. The low photofraction of HPGe in relation to scintillators suggests that HPGe detectors are best suited to application in small animal imaging systems. While the fine energy resolution facilitates the highly effective scatter rejection which would improve the quality of clinical images, the resulting loss of sensitivity (when using detectors of relatively low volume at least) is likely to render a human HPGe PET system impractical at this time. Short term developments in HPGe systems for small animal imaging should focus on the development and refinement of digital pulse processing techniques. Improvements in PSA algorithms will facilitate improved spatial resolution and in principle allow all detected coincident events to be used for imaging. The ability to accurately identify the depth of a gamma ray interaction (DOI), and ultimately reconstruct the interaction sequence for multiple hits, may prove to be crucial. As the blurring induced by parallax error in a scintillator may degrade image spatial resolution by a factor of three [Mos97], considerable research effort is being dedicated to investigating methods for measuring the DOI in scintillators. The effect of parallax error becomes particularly significant for small ring diameters [Zie05] such as those used in small animal systems and thus the potential for HPGe detectors to provide 1mm DOI sensitivity presents interesting opportunities as the quest for optimum spatial resolution continues.

The introduction of HPGe to clinical (human) PET is limited mainly by the low stopping power of the material. Assuming gamma rays scattering within the material can be used for imaging, this problem may be overcome by simply using more HPGe to absorb the annihilation gamma rays. As it is not currently possible to produce planar HPGe crystals with depth profiles greater than around 20mm this may require the integration of two or more individual crystals into a single cryostat. Factors which may limit the use of HPGe in PET extend to both clinical and pre-clinical (small animal) imaging scenarios. The relatively poor timing resolution provided by HPGe detectors relative to fast scintillators is an issue which must be taken into account as are more practical considerations such as system cost and the requirement for cooling.

It appears that with continued development, HPGe detectors may be capable of making a significant contribution to small animal PET imaging while their role in clinical PET remains less clear. With increasing interest in the development of instrumentation for medical imaging, both in terms of PET and Compton imaging for SPECT, the next five to ten years looks set to provide answers to many as yet unresolved issues.

Appendix A

SmartPET Energy Resolutions

A.1 Energy Resolution at 511keV

The energy resolution (FWHM) of all 48 channels of the two SmartPET detectors at 511keV as recorded through the GRT4 digital electronics is presented in Table A.1.

The values show good uniformity with the exception of strip AC06 of SmartPET2 which exhibits an inconsistently large value of FWHM. The FET input stage of the preamplifier coupled to this strip was replaced after being damaged during powering of the detector following thermal cycling. This procedure appears to have resulted in a degradation of energy resolution, likely due to poor grounding.

An energy resolution of 3.98keV FWHM is quoted for strip DC11 of SmartPET1. Prior to the application of the charge sharing correction algorithm discussed in Chapter 5, the energy resolution is 7.34 keV.

A.2 Energy Resolution at 122keV

The energy resolution (FWHM) of all 48 channels of the two SmartPET (SP1 and SP2) detectors at 122keV is presented in Table A.2. The energy resolution quoted by ORTEC are also tabulated. All values presented were recorded through analogue electronics using an ORTEC 671 Spectroscopy Amplifier. The values of SmartPET1 are quoted for an amplifier shaping time of 6μs while the SmartPET2 energy resolutions were recorded using a shaping time of 3μs. It is observed that the values of energy resolution are consistently worse for the

Channel	**SmartPET1 Energy Resolution (keV)**	**SmartPET2 Energy Resolution (keV)**
AC01	3.33	3.21
AC02	3.16	3.20
AC03	3.22	3.48
AC04	3.24	3.14
AC05	3.22	3.02
AC06	3.20	4.97^{+}
AC07	3.14	3.16
AC08	3.08	3.05
AC09	3.11	3.11
AC10	3.01	3.01
AC11	3.42	3.13
AC12	3.50	3.32
DC01	3.21	3.72
DC02	3.48	3.16
DC03	3.12	3.24
DC04	3.09	3.81
DC05	3.21	3.37
DC06	3.34	3.22
DC07	3.12	3.62
DC08	3.36	3.29
DC09	3.18	3.54
DC10	3.40	3.18
DC11	3.98*	3.41
DC12	3.25	3.50

Table A.1: The energy resolution (FWHM) of all 48 channels of the SmartPET detectors at 511keV. The uncertainty in all values of FWHM are $\leq$5%. *Prior to the application of the charge sharing correction algorithm discussed in Chapter 5, the energy resolution of DC11 is 7.34 keV. $^{+}$ The FET at the input stage of the preamplifier coupled to strip AC06 on SmartPET2 was replaced after being damaged during powering of the detector following thermal cycling. This procedure has resulted in a degradation of energy resolution, likely due to poor grounding.

SmartPET2 detector relative to SmartPET1. This is likely to be due to the SmartPET2 detector suffering from a highly unstable baseline (baseline shifts ∼200mV are observed), possibly the result of a faulty high voltage filter.

Channel	**SP1 Resolution (ORTEC)**	**SP1 Resolution (Liverpool)**	**SP2 Resolution (ORTEC)**	**SP2 Resolution (Liverpool)**
	(keV)	**(keV)**	**(keV)**	**(keV)**
AC01	1.51	1.45	1.57	1.73
AC02	1.41	1.36	1.61	1.66
AC03	1.46	1.42	1.52	1.60
AC04	1.47	1.39	1.46	1.49
AC05	1.45	1.39	1.39	1.48
AC06	1.62	1.48	1.41	1.51
AC07	1.45	1.40	1.48	1.56
AC08	1.43	1.40	1.49	1.55
AC09	1.44	1.42	1.49	1.54
AC10	1.40	1.38	1.50	1.53
AC11	1.49	1.38	1.48	1.54
AC12	1.49	1.46	1.45	1.66
DC01	1.73	1.71	1.42	1.38
DC02	1.30	1.20	1.45	1.40
DC03	1.48	1.34	1.61	1.46
DC04	1.29	1.35	1.57	1.50
DC05	1.30	1.41	1.58	1.40
DC06	1.25	1.32	1.64	1.45
DC07	1.30	1.38	1.74	1.48
DC08	1.29	1.31	1.60	1.56
DC09	1.29	1.27	1.75	1.54
DC10	1.43	1.41	1.56	1.44
DC11	2.53	3.79	1.44	1.55
DC12	1.61	1.76	1.45	1.61

Table A.2: The energy resolution (FWHM) of all 48 channels of the SmartPET detectors at 122keV along with values quoted by the manufacturer (ORTEC). The uncertainty in all values of FWHM measured at Liverpool are $\leq$5%.

Appendix B

Cross-talk Correction and Add-Back

The advent of composite HPGe detectors with increased granularity such as the Clover detector [Duc99], [Gro05] gave rise to the concept of operating in either direct mode, where each crystal is operated as a single detector, or Add-Back mode, where the sum of energies deposited in multiple crystals during Compton scattering events is calculated. The treatment of data in Add-Back or 'total' detection mode serves to maximise the photopeak efficiency and peak-to-total ratio.

In Chapter 4 the absolute efficiency, intrinsic efficiency and peak-to-total ratio of the SmartPET1 detector were presented. These values were calculated with the detector operating in total detection mode. However, when 'adding-back' the energy deposited in multiple interactions, the procedure is complicated by the presence of electronic cross-talk between detector segments.

B.1 Cross-talk

Proportional cross-talk[1] is an undesired coupling between electronics channels resulting in a shift of the baseline of channels neighbouring a hit strip. When performing calculations of

---

[1] A second type of cross-talk, not observed in the SmartPET detectors also exists. This is known as derivative cross-talk as the effect is proportional to the derivative of the induced signal. Further information on derivative cross-talk may be found in [Vet00] and [Bru06]

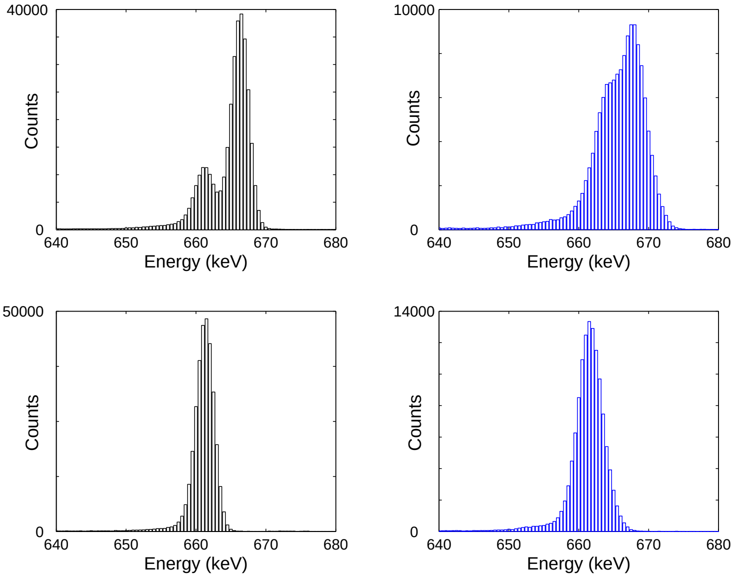

Figure B.1: Spectra showing the 662keV photopeaks from the ^{137}Cs Add-Back of AC strips on SmartPET1. The top row shows uncorrected spectra from fold two (left) and fold three (right) Add-Back while the bottom row shows the same photopeaks with the application of cross-talk correction.

Add-Back energy, these baseline shifts cause shifts in energy resulting in peak broadening and/or double peaking. This can be observed in the top row of Figure B.1 which shows the photopeak from ^{137}Cs Add-Back spectra constructed individually from fold two and fold three interactions where no cross-talk correction has been applied.

The magnitude of the cross-talk was calculated by measuring the baseline shift (in keV) as a function of gamma-ray energy. This result is displayed in Figure B.2 where the directly proportional nature of the cross-talk is clear. From the gradient of the trend line the magnitude of the cross-talk between AC coupled strips on SmartPET1 is found to be $\sim$0.7% of the deposited energy.

Performing a similar analysis for the DC coupled face reveals the presence of proportional cross-talk of $\sim$0.2% of the induced signal. The reduced level of cross-talk observed between DC coupled strips is believed to be due to the lower interstrip capacitance resulting from the larger interstrip gap. This is consistent with the findings of Kroeger *et al.* in [Kro95]. It is also found that the crosstalk values are consistent between both SmartPET detectors.

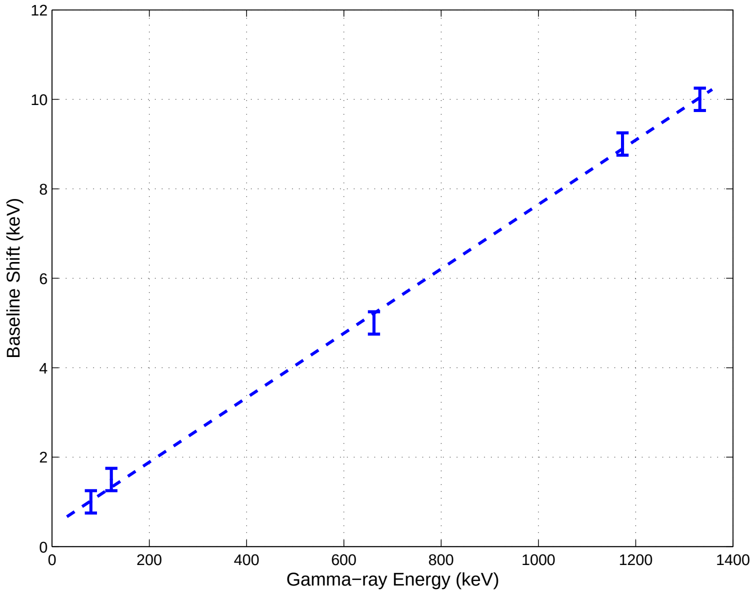

Figure B.2: Plot showing the baseline shift resulting from cross-talk as a function of energy deposited. The linear trend shows how the magnitude of this cross-talk is directly proportional to the induced signal. From the gradient of the trend line the cross-talk between AC coupled strips on SmartPET1 is found to be ∼0.7% of the energy deposited.

B.2 Fold Two Add-Back

To confirm the assumption that cross-talk occurs between neighbouring strips only, an analysis of fold two events from an uncollimated ^{137}Cs point source was performed. Individual Add-Back spectra were created for events scattering between adjacent strips and those scattering between non-adjacent strips. Figure B.3 shows the Add-Back photopeak from each category of event along with the Add-Back photopeak from all fold two events recorded on the AC face of the SmartPET1 detector. These spectra show how the Add-Back energy calculated from events scattering between non-adjacent strips is unaffected by cross-talk, with the photopeak centroid lying at 662keV. For events scattering between neighbouring strips the photopeak is shifted by around 4keV (∼0.7% of 662keV) to 666keV.

This shift was corrected for by applying an event-by-event correction coefficient to the sum energy calculated for all fold two events occurring between adjacent strips. The resultant photopeak is shown in the bottom left of Figure B.1 where the correction is shown to allow the reconstruction of the full energy peak.

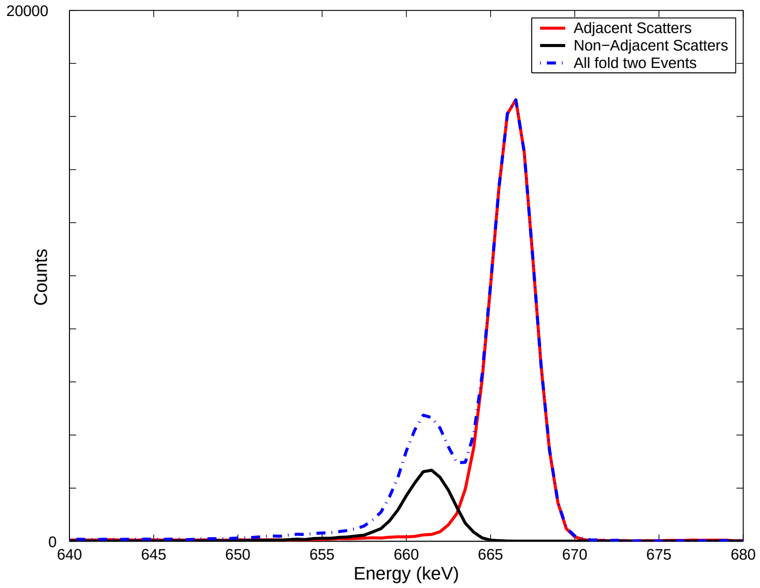

Figure B.3: Add-Back (^{137}Cs) photopeaks from fold two events. The photopeaks resulting from Add-Back of adjacent and non-adjacent scattered events are shown along with that arising from all fold two events. The x-axis shows the energy in keV while the y-axis contains the number of counts on a linear scale.

B.3 Fold Three Events

The same correction methodology was developed for fold three interactions where an additional level of complexity exists due to the number of scatter scenarios which may occur. The analysis was performed using five major scattering scenarios, displayed diagramatically in Figure B.4. It is as a result of these different cross-talk contributions that the photopeak appears broadened in Figure B.1(top right). By analysing the energy spectra produced from the Add-Back of each event type a series of correction coefficients were generated. By applying these on an event-by-event basis, in the same way as for fold two events, the effect of the proportional cross-talk is removed and the full energy peak recovered (see bottom right image of Figure B.1).

For events which interact in more than three strips on a single face, no cross-talk correction is applied due to the large number of scatter combinations which are possible. Such events account for less than 1% of all events at 511keV.

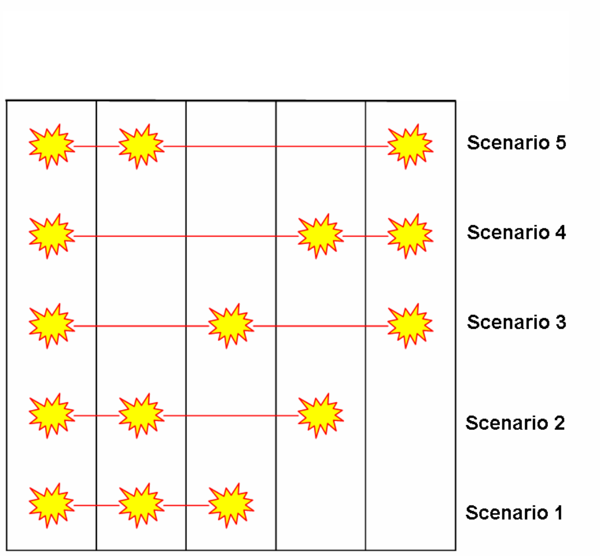

Figure B.4: The five scattering scenarios considered for fold three events when developing the cross-talk correction.

B.4 Add-Back Efficiency

With the cross-talk correction now in place, the absolute Add-Back efficiency of the Smart-PET1 detector as a function of energy was calculated for double hit (fold two) and triple hit (fold three) events. Data were then analysed using all events, performing an energy Add-Back for events with fold greater than one. Figure B.5 shows how the absolute efficiency varies as a function of energy for a range of fold scenarios and the total Add-Back efficiency. This plot demonstrates how the Add-Back procedure may be employed to greatly improve the efficiency of the detector.

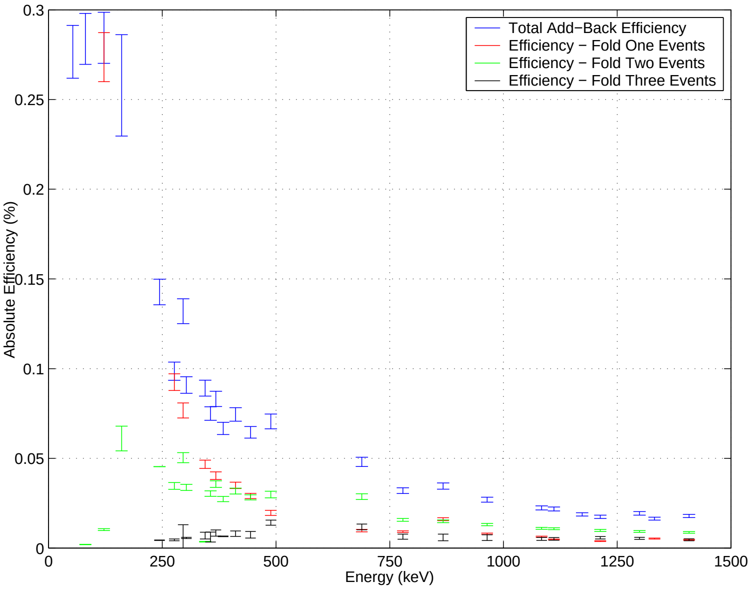

Figure B.5: Plot showing the variation of absolute efficiency as a function of energy.

Bibliography

[Amm00] *Three-dimensional position sensing and field shaping in orthogonal-strip germanium gamma-ray detectors*, M. Amman and P.N. Luke, NIM A452 (2000) 155-166.

[Bad98] *Algorithms for calculating detector efficiency normalization coefficients for true coincidences in 3D PET*, R.D. Badawi *et al.*, Phys. Med. Biol. 43 (1998) 189-205.

[Baz04] *The Advanced Gamma Ray Tracking Array AGATA*, D. Bazzacco, Nucl. Phys. A 746 (2004) 248c-254c.

[Bos05] *The SmartPET DAQ*, A.J. Boston, Oral contribution, SmartPET collaboration meeting, Melbourne (2005).

[Bos07] *Characterisation of the SmartPET planar germanium detectors*, H.C. Boston *et al.* NIM A (2007) 104-107.

[Bos07b] *Characterisation of the first SmartPET planar germanium detector*, H.C. Boston-Scraggs *et al.*, In preparation, NIM A.

[Bru06] *Characterisation of large volume HPGe detectors. Part II: Experimental results*, B. Bruyneel *et al.*, NIM A569 (2006) 774-789.

[But73] *Construction and use of a three Ge(Li) Compton polarimeter*, P.A. Butler *et al.*, NIM 108 (1973) 497-502

[But87] *The application of semiconductor detectors in nuclear structure physics*, P.A. Butler, NIM A255 (1987) 194-198.

[CEL] *http://www.celoxica.com.*

[Cob03] *3-D positioning germanium detectors for gamma-ray astronomy*, W. Coburn *et al.*, X-Ray and Gamma-Ray Detectors and Applications IV, Proceedings of SPIE 4748 (2003).

[Coo07a] *Position sensitivity of the first SmartPET HPGe detector*, R.J. Cooper *et al.* NIM A573 (2007) 72-75

[Coo07b] *SmartPET: Applying HPGE and pulse shape analysis to small-animal PET*, R.J. Cooper *et al.* NIM A (2007) 313-317.

[Cha00] *Positron Physics, Cambridge University Press*, M. Charlton and J.W. Humberston (2000).

[Che97] *MicroPET: A high resolution PET scanner for imaging small animals*, S.R. Cherry *et al.*, IEEE Transactions on Nuclear Science 44 (1997) 1161-1166.

[Che01] *Use of Positron Emission Tomography in animal research*, S.R. Cherry and S.S. Gambhir, ILAR Journal V42(3) 2001.

[Che03] *Physics in Nuclear Medicine, Third Edition*, S.R. Cherry, J.A. Sorenson and M.E. Phelps (2003).

[Che04] *In vivo molecular and genomic imaging: new challenges for imaging physics*, S.R. Cherry, Phys. Med. Biol. 49 (2004) 13-48.

[Cob02] *Results of charge sharing tests in a Ge strip detector*, W. Coburn, S.E. Boggs, S. Amrose, R.P. Lin *et al.* IEEE (2002).

[Col05] Verification of the GREAT Total Data Readout system using pseudo random patterm generator, P.J. Coleman-Smith, IEEE NSS Conference Record (2005).

[Cor63] *Representation of a function by its line integrals with some radiological applications*, A.M. Cormack, J. Applied Physics, vol. 31 no. 9, pp. 2722-2727 (1963).

[Del99] *GRETA: utilizing new concepts in γ-ray detection*, M.A. Deleplanque *et al.*, NIM A430 (1999) 292-310.

[Der88] *A Positron Tomograph with 600 BGO crystals and 2.6mm resolution*, S.E. Derenzo *et al.*, IEEE Transactions on Nuclear Science, 35 (1988) 1

[Des02] *Improving the position resolution of highly segmented HPGe detectors using pulse shape analysis methods*, M. Descovich, Ph.D Thesis, The University of Liverpool (2002).

[Des05a] *The position response of a large-volume segmented germanium detector*, M. Descovich *et al.*, NIM A553 (2005) 512-521.

[Des05b] *In-beam measurement of the position resolution of a highly segmented coaxial germanium detector*, M. Descovich *et al.*, NIM A553 (2005) 535-542.

[Des05c] *Real time pulse shape analysis for the γ-interactions in AGATA*, P. Desesquelles *et al.*, IEEE NPSS Real Time Conference (2005) 100-102.

[Dob05] *The characterisation and position resolution of a planar germanium strip detector*, J.L. Dobson, Ph.D Thesis, The University of Liverpool (2005).

[Dox07] *An approximate method for linear signal decomposition in γ-ray tracking detectors*, I. Doxas *et al.*, NIM A (2007).

[Duc99] *The Clover: a new generation of composite Ge detector*, G. Duchene *et al.*, NIM A432 (1999) 90-110

[Ebe01] *MINIBALL A Ge detector array for radiaoctive ion beam facilities*, J. Eberth *et al.*, Prog. Part. Nucl. Phys. 46 (2001) 389-398.

[Fir96] *Table of Isotopes, Eighth Edition, Volume I*, R.B. Firestone (1996).

[Gas00] *Digital signal processing and algorithms for gamma-ray tracking*, W. Gast *et al.*, IEEE NSS Conference Record (2000) 2 182-185.

[GEA] *http://geant4.web.cern.ch/geant4*

[Geo94] *An analog-to-digital conversion based on a moving window deconvolution*, A. Georgiev, W. Gast and R.M Lieder, IEEE Transactions on Nuclear Science, Volume 41, Issue 4 (1994).

[Ger05] *Gamma-ray imaging exploiting the Compton effect*, J. Gerl, Nucl. Phys. A 752 (2005) 688c-695c.

[Gil07] *Effect of position resolution on LoR discrimination for a dual-head Compton camera*, J. Gillam *et al.*, NIM A573 (2007) 76-79.

[Gri07] *Private Communication, A.N. Grint.*

[Gro05] *Characterisation of an Exogam clover germanium detector*, S.A.A. Gros, Ph.D Thesis, The University of Liverpool (2005).

[Hal06] *Germanium: From its discovery to SiGe devices*, E.E. Haller, Materials Science in Semiconductor Processing 9 (2006) 408-422.

[Har04] *Positronium: Review of symmetry, conserved quantities and decay for the radiological physicist*, M.D. Harpen, Medical Physics, 31(1) 57-61 (2004).

[Has91] *A prototype high-purity germanium detector system with fast photon-counting circuitry for medical imaging*, B.H. Hasegawa *et al.*, Med. Phys. 18 5 (1991) 900-909.

[Hem95] *Practical gamma-ray spectrometry*, G. Gilmore and J.D. Hemingway (1995).

[He00] *Review of the Shockley-Ramo theorem and its application in semiconductor gamma-ray detectors*, Z. He, NIM A463 (2000) 250-267.

[Hoo03] *Development of a new silicon based detector module for PET*, P.R. Hooper, MSc Thesis, The University of Wollongong (2003).

[Hub99] *Conceptual design of a high-sensitivity small animal PET camera with 4π coverage*, J.S. Huber and W.W. Moses, IEEE Transactions on Nuclear Science, vol. 46, no. 3 (1999).

[Ide03] *Position sensitivity of a segmented planar Ge detector*, E. Ideguchi *et al.*, NIM A496 (2003) 373-384.

[JAS] *http://www.spect.com/pub/Flanged*$_{j}$*aszczak*$_{p}$*hantoms.pdf*

[Jon07] *Meeting the Future Challenges of PET Based Molecular Imaging*, T. Jones, Oral contribution, Mayneord-Phillips Summer School on Molecular Imaging with Positron Emission Tomography (2007).

[Kac04] *Three-gamma annihilation imaging in positron emission tomography*, K. Kacperski *et al.*, IEEE Transactions on Medical Imaging, 23 4 (2004) 525-529.

[Kac05] *Performance of three-photon PET imaging: Monte Carlo simulations*, K. Kacperski and N.M. Spyrou, Phys. Med. Biol. 50 (2005) 5679-5695.

[Kak89] *Principles of Computerized Tomographic Imaging*, A.C. Kak and M. Slaney, IEEE Press (1989).

[Kar06] *Comparative evaluation of two commercial PET scanners, ECAT EXACT HR+ and Biograph 2, using GATE*, N. Karakatsanis *et al.*, NIM A569 (2006) 368-372.

[Kau78] *Imaging characteristics of a small germanium camera*, L. Kaufman *et al.*, Invest. Radiol. 13 (1978) 223-232.

[Kin96] *Efficiency normalization techniques for 3D PET data*, P.E. Kinahan *et al.*, IEEE NSS MIC Conference Record 2 (1996) 1021-1025.

[Kit76] *Introduction to Solid State Physics, Fifth Edition*, C. Kittel (1976).

[Kle29] *Über die Streuung von Strahlung durch freie Elektronen nach der neuen relativistisschen Quantendynamik von Dirac*, O. Klein and Y. Nishina, Z. Phys. 52 (1929) 853-868.

[Kli07] *Qualitative aspects of image applications in multimedia technology*, M. Klima, Radioelektronika (2007) 17th International Conference.

[Kno99] *Radiation Detection and Measurement, Third Edition*, G.F. Knoll (1999).

[Kro95] *Spatial resolution and imaging of gamma-rays with germanium strip detectors*, R.A. Kroeger *et al.*, SPIE (1995) Vol. 2518.

[Kro96] *Analysis of simulated and measured pulse shapes of closed-ended HPGe detectors*, Th. Kroll *et al.*, NIM A371 (1996) 489-496.

[Kro99] *Charge spreading and position sensitivity in a segmented planar germanium detector*, R.A. Kroeger *et al.*, NIM A422 (1999) 206-210.

[Lar06] *Small Animal PET: A review of commercially available imaging systems*, M. Larobina, A.Brunetti and M. Salvatore, Current Medical Imaging Reviews, (2006) 2, 187-192.

[Laz03] *The GRT4 VME pulse processing card for segmented germanium detectors*, I.H. Lazarus *et al.*, IEEE Nuclear Science Symposium, (2003) N29-36.

[Laz06] *Private Communication*, I. Lazarus.

[Lee99] *Gamma-ray tracking detectors*, I.Y. Lee *et al.*, NIM A422 (1999) 195-200.

[Lev97] *Compton scatter and x-ray crosstalk and the use of very thin inter-crystal septa in high resolution pet detectors*, C.S Levin *et al.*, IEEE Trans. Nucl. Sci. 44 2 (1997) 218-224.

[Lev99] *Calculation of positron range and its effect on the fundamental limit of positron emission tomography system spatial resolution*, C.S. Levin and E.J. Hoffman, Phys. Med. Biol. 44 (1999) 781-799.

[Lie01] *The TMR network project: Development of γ-ray tracking detectors*, R.M. Lieder *et al.*, Nuc. Phys. A 682 (2001) 279c-285c.

[Lil02] *Nuclear Physics Principles and Applications*, J. Lilley (2002).

[Lop04] *γ-ray tracking algorithms: a comparison*, A. Lopez-Martens *et al.*, NIM A533 (2004) 454-466.

[Luk00] *Coplanar-grid CdZnTe detector with three-dimensional position sensitivity*, P.N. Luke *et al.*, NIM A439 (2000) 611-618.

[MAE] *http://www.ortec-online.com/software/softwaremca.htm*

[Man02] *Positron Emission Tomography in Cancer research and treatment*, M. Mandelkern and J. Raines, Technology in Cancer Research & Treatment, 1 (1002) 423-439.

[Mar00] *Physics for Radiation Protection*, J.E. Martin (2000).

[MAT] *http://www.mathworks.com/products/matlab/*

[Mat04] *Small animal PET demonstrator Monte Carlo simulations*, A.R. Mather, Poster contribution, The University of Liverpool Research in Progress Poster Day (2004).

[Mat06] *Evaluation of the planar germanium SmartPET system for use in Positron Emission Tomography*, A.R. Mather, Ph.D Thesis, The University of Liverpool (2006).

[MCN] *http://mcnp-green.lanl.gov/index.html.*

[Med04] *A simple method for the characterization of HPGe detectors*, P. Medina *et al.*, Instrumentation and Measurement Technology Conference, Italy (2004).

[Mih00] *The influence of anisotropic electron drift velocity on the signal shapes of closed-end HPGe detectors*, L. Mihailescu *et al.*, NIM A447 (2000) 350-360.

[Mih04] *SPEIR: a Ge Compton camera*, L. Mihailescu *et al.*, NIM A570 (2007) 89-100.

[Mih05] *Methods for increasing the efficiency of Compton imagers*, L. Mihailescu *et al.*, IEEE NSS (2006) Conference Record.

[Mih07] *Data acquisition with a fast digitizer for large volume HPGe detectors*, L.C. Mihailescu et al., NIM A578 (2007) 298-305.

[Mil05] *3D position sensitivity of a highly segmented Ge detector*, L. Milechina and B. Cederwall, NIM A550 (2005) 278-291.

[Mis04] *Performance evaluation of the 16-module quad-HIDAC small animal PET camera*, J. Missimer *et al.*, Phys. Med. Biol. 49 (2004) 2069-2081.

[Mos93] *Empirical observation of resolution degradation in positron Emission Tomographs utilizing block detectors*, W.W. Moses *et al.*, J. Nucl. Med., vol. 34, (1993) pp. 101P.

[Mos97] *Design of a high-resolution, high-sensitivity PET camera for human brains and small animals*, W.W. Moses *et al.*, IEEE Trans. Nucl. Sci. NS-44 (1997) 1487-1491.

[Mos03] W.W. Moses, Oral contribution IEEE Medical Imaging Conference, Portland, Oregon (2003).

[Nel07] *Characterisation of an AGATA symmetric prototype detector*, L. Nelson *et al.*, NIM A573 (2007) 153-156.

[Nic01] *A positron floodlight for PET attenuation measurements*, R.J. Nickles, IEEE Transactions on Nuclear Science, Vol. 48, No. 1 (2001).

[Nol85] *The performance of a bismuth germanate escape suppressed spectrometer*, P.J. Nolan *et al.*, NIM A236 (1985) 95-99.

[Ola06] *Pulse Shape Analysis for the location of the γ-interactions in AGATA*, A. Olariu *et al.*, IEEE Trans. Nucl. Sci. (2006) 53 3.

[Owe85] *Spectral degradation effects in an 86cm^3 Ge(HP) detector*, A. Owens, NIM A238 (1985) 473-478.

[Pag03] *The GREAT spectrometer*, R.D. Page *et al.*, NIM B204 (2003) 634-637.

[Par03] *Effect of inter-crystal Compton scatter on efficiency and image noise in a small animal PET module*, S-J. Park *et al.*, IEEE NSS Conference Record Vol. 4 (2003) 2272-2277.

[Par04] *PET reconstruction with system matrix dervived from point source measurements*, V.Y. Para *et al.*, IEEE NSS Conference Record, Vol. 4 (2004) 2483-2487.

[Phi02] *Small animal PET imaging with germanium strip detectors*, B.F. Phillips *et al.*, IEEE Medical Imaging Conference Record (2002).

[Piq04] *A probabilistic γ-ray tracking method for germanium detectors*, I. Piqueras *et al.*, NIM A516 (2004) 122-133.

[Poe97] *Experimental Techniques in Nuclear Physics*, D.N. Poenaru and W. Greiner (1997).

[Rad17] *Uber die Bestimmug von Funkitionen durch ihre integralwerte langs gewisser Manningfaltigkeiten*, J. Radon, Math. Phys. K1. 69, (1917), 262.

[Rad88] *Low noise techinques in detectors*, V. Radeka, Annual Review of Nuclear and Particle Science, 38 (1988).

[Rad04] *Decomposition Algorithm Development*, D. Radford, Oral contribution to the GRETINA software meeting (2004).

[Ram39] *Currents induced by electron motion*, S. Ramo, Proceedings of the Institute of Radio Engineers, 27 (1939).

[Rea02] *One-pass list-mode EM algorithm for high-resolution 3-D PET image reconstruction Into large arrays*, A.J. Reader *et al.*, IEEE Trans. Nucl. Sci. 49 (2002) 693-698.

[Rei02] *The MINIBALL array*, P. Reiter *et al.*, Nucl. Phys. A 701 (2002) 209-212.

[Rus80] *An ultrapure germanium detector array for quantitating three-dimensional distribution of a radionuclide: a study of phantoms*, H. Rusinek *et al.* J. Nucl. Med. 21 (1980) 777-782.

[San04] *Private Communication*, P. Sangsingkeow, ORTEC, Oak Ridge.

[San05] *Private Communication*, P. Sangsingkeow, ORTEC, Oak Ridge.

[Sch99] *A γ-ray tracking algorithm for the GRETA spectrometer*, G.J. Schmid *et al.*, NIM A430 (1999) 69-83.

[Sen07] *Proceedings of the 2007 International Workshop on Semiconductor PET*, http://www.qse.tohoku.ac.jp/pet/workshop

[Sha90] *Quantifying image quality*, P.F. Sharp, Clin. Phys. Physiol. Meas. 11 (1990) A 21-26

[She82] *Maximum likelihood reconstruction for emission tomography*, L.A Shepp and Y. Vardi, IEEE Trans. Med. Imag. vol. MI-1, pp. (1982) 113-122.

[Sho38] *Currents to conductors induced by a moving point charge*, W. Shockley, Journal of Applied Physics, 10 (1938) 635.

[SIE] *http://www.medical.siemens.com*

[Sim83] *Application of a sectored Ge(Li) detector as a Compton polarimeter*, J. Simpson *et al.*, NIM 204 (1983) 463-469.

[Sim05] *The AGATA Project*, J. Simpson, J. Phys. G: Nucl. Part. Phys. 31 (2005) 1801-1806.

[Sze02] *Semiconductor Devices Physics and Technology, 2nd Edition*, S.M. Sze (2002).

[Tar03] *PET instrumentation and reconstruction algorithms in whole-body applications*, G. Tarantola *et al.*, Journal of Nuclear Medicine 45 (2003) 756-769.

[Tom03] *Analytical image reconstruction of cone-beam projections from limited-Angle Compton camera data*, T. Tomitani and M. Hirasawa, IEEE Transactions on Nuclear Science, Vol.50, No. 5, (2003).

[Tow04] *Principles and Technology of PET*, D.W. Towndend, Ann. Acad. Med. Singapore 33 (2004) 133-145.

[Tur06] *The characterisation of the first SmartPET HPGe planar detector*, G.H.B. Turk, Ph.D Thesis, The University of Liverpool (2006).

[Val03] *Positron Emission Tomography: Basic Science and Clinical Practice*, P.E. Valk *et al.*, (2003).

[Vas02] *Effects of inter-crystal cross-talk on multi-element LSO/APD PET detectors*, P. Vaska *et al.*, IEEE NSS Conference Record, Vol. 3 (2002) 1643-1647.

[Vet00] *Performance of the GRETA prototype detectors*, K. Vetter *et al.*, NIM A452(2000) 105-114.

[Vet04] *Gamma-ray imaging with position-sensitive HPGE detectors*, K. Vetter *et al.*, NIM A525 (2004) 322-327.

[Wal01] *Quad-HIDAC PET: Comparison of list-mode and projection-data driven image reconstruction for high resolution imaging*, R.J. Walledge *et al.*, IEEE NSS and MIC Conference Record (2001).

[Wan02] *Why is image quality assessment so difficult?*, Z. Wang *et al.*, IEEE International Conference on Acoustics, Speech and Signal Processing (2002).

[Web00] *Three photon annihilations of positrons and positronium in solids with two detectors in coincidence*, M.H. Weber and K.G. Lynn, Radiation Physics and Chemistry 58 (2000) 749-753.

[Web04] *Small animal PET: aspects of performance assessment*, S. Weber and A. Bauer, European Journal of Nuclear Medicine and Molecular Imaging 31 11 (2004).

[Wie03] *Gamma-ray tracking with segmented HPGe detectors*, O. Wieland *et al.*, Brazillian Journal of Physics 33 2 (2003) 206-210.

[Zav06] *SiliPET: An ultra high resolution design of a small animal PET scanner based on double sided silicon strip detector stacks*, G.Zavattini *et al.*, NIM A568 (2006) 393-397.

[Zhe02] *High speed real-time data acquisition and transfer system based on FPDP*, Z. Huachun *et al.*, Proceedings of the (2002) International Conference on Control and Automation.

[Zie05] *Positron Emission Tomography: Principles, technology and recent developments*, S.I. Ziegler, Nucl. Phys. A 752 (2005) 679c-687c.